UNIVERSITÉ DE LORRAINE | BIBLIOTHÈQUES UNIVERSITAIRES

AVERTISSEMENT
DROIT D'AUTEUR

Ce document est le fruit d'un long travail approuvé par le jury de soutenance et mis à disposition de l'ensemble de la communauté universitaire élargie.

Il est soumis à la propriété intellectuelle de l'auteur. Ceci implique une obligation de citation et de référencement lors de l'utilisation de ce document. Toute contrefaçon, plagiat ou reproduction illicite encourt une poursuite pénale.

Contact bibliothèque : ddoc-theses-contact@univ-lorraine.fr
(Cette adresse ne permet pas de contacter les auteurs)

Code de la Propriété Intellectuelle. articles L 122. 4
Code de la Propriété Intellectuelle. articles L 335.2- L 335.10

UNIVERSITÉ DE LORRAINE
34 COURS LÉOPOLD — CS 25233
54052 NANCY CEDEX
TÉL : 03 54 50 54 00
CONTACT@UNIV-LORRAINE.FR
WWW.UNIV-LORRAINE.FR

École doctorale C2MP

Thèse

présentée en vue de l'obtention du titre de

Docteur de l'Université de Lorraine
en Chimie théorique et informatique

par

Rohith Ravi

Apolipoprotein A-I Mimetic Peptide-Lipid Assemblies: A Molecular Dynamics Study

Assemblages peptide-lipide mimétiques de l'apolipoprotéine A-I : une étude par dynamique moléculaire

soutenue publiquement le 10/12/2025
à l'université de Lorraine, Nancy, France.

Rapporteurs

Prof. Ana-Nicoleta Bondar, University of Bucharest, Romania

Prof. Christophe Ramseyer, Chrono-environnement - UMR 6249 CNRS/ UFC Campus de la Bouloie, Besançon, France

Examinateurs

Prof. Elmira Arab Tehrany, University of Lorraine, Nancy, France
(Présidente du jury)

Dr. Luca Monticelli, Molecular Microbiology and Structural Biochemistry (MMSB), UMR 5086 CNRS, Lyon, France

Directeur de thèse

Dr. Mounir Tarek, UMR CNRS 7019, University of Lorraine, France

Acknowledgements

I would like to thank my thesis reviewers, **Prof. Christophe Ramseyer** and **Prof. Ana Nicoleta Bondar**, for taking the time to carefully review my work and for their valuable insights. I'm also grateful to my monitoring committee members and thesis examiners, **Dr. Luca Monticelli** and **Prof. Elmira Arab Tehrany**, for their time and support throughout my PhD journey.

A very special thank-you goes to my advisor, **Dr. Mounir Tarek**, for his guidance, patience, and trust. I learned a lot from him over these three years.

I would also like to thank my collaborators, **Prof. Burkhard Bechinger**, **Dr. Evgeniy S. Salnikov**, **Prof. Gunther Marsche**, **Mrs. Alankrita Rani**, **Prof. Ruth Prassl**, and **Dr. Karin Kornmüller**, for the wonderful scientific discussions.

I am thankful to **Dr. Fabien Pascal** and **Dr. Abdallah Ammar** for their help with the technical set-up, and to **Mrs. Séverine Bonenberger** and **Mrs. Véronique Baur** for making the administrative side of things much smoother.

To my groupmates **Daniel** and **Yulia**: thank you for everything, from funny conversations to exciting scientific discussions.

Life in Nancy, inside and outside the lab, was much better thanks to my dear friend **Marta**. Thank you for reminding me that there's a world outside PhD deadlines.

And to **Giuseppe**, **Chengyu**, **Radu**, **Sergio**, **Atilla**, **Filippo**, **Mayank**, **Yuya**, **Jeremy**, **Leila**, **Andy**, and **Yash**: thank you for making these three years in Nancy such a great time.

A heartfelt thank-you to **Michele**, who treated me like her own son and helped me deal with homesickness. A special thanks to **Suganthan**, **Souloke**, and **Ashith** for their support and for the travels that truly kept me sane during this journey.

Finally, I would like to thank my Liebling, **Princy**, for her indispensable support and for giving me the strength to keep going. And to my family: thank you for your endless love, support, and belief in me always.

Abstract

Apolipoprotein A-I (apoA-I) is the principal protein of high-density lipoproteins (HDL) and a key driver of reverse cholesterol transport (RCT), promoting cholesterol efflux via ABCA1 and the formation of nascent HDL. Its tandem amphipathic helices stabilize lipid bilayers, and apoA-I also exhibits antioxidant, anti-inflammatory, and anti-atherogenic activities, underscoring its relevance to cardiovascular health. However, trials aimed at raising HDL have not yielded the anticipated clinical benefit, and native apoA-I poses manufacturing and delivery challenges. apoA-I mimetic (AAM) peptides, short, synthetic amphipathic helices, were developed to emulate apoA-I's structural and functional features. They self-assemble with lipids to form peptide–lipid nanodiscs used in cardiovascular therapies and biomedical applications, and as versatile scaffolds for the characterization of membrane proteins in structural biology.

Despite extensive work on nanodiscs, their structure, dynamics, and physicochemical properties remain largely unexplored. This thesis combines all-atom molecular dynamics (MD) simulations with experimental data from our collaborators to deliver atomistic insight into amphipathic α-helical apoA-I mimetic peptide–lipid assemblies. **The primary goal of this PhD thesis is to provide detailed atomistic insights into their structure, dynamics, and to decipher the key interactions that stabilize these peptide-lipid assemblies**.

In this study, we focused on the clinically relevant derivatives of 18A peptides, namely **14A, 4F, and 4F-P-4F peptides**, which have attracted considerable biomedical interest. Our Investigation begins with 14A lipid nanodiscs, quantifying peptides' orientation around the lipid bilayers, and identifying interactions that stabilize nanodisc structure and dynamics. Back-calculated ^{15}N chemical shifts and ^{2}H quadrupolar splitting agree with prior solid-state Nuclear Magnetic Resonance (ssNMR), supporting a dimeric, antiparallel belt of 14A around the discoidal bilayer. Nanodisc stability arises from aromatic π–π stacking between peptides, as well as electrostatic and hydrophobic peptide–lipid interactions, producing stable discs with heterogeneous lipid order and thickness from center to rim and providing atomistic evidence for the previously hypothesized interactions that stabilize the nanodisc.

We next examined 4F and its tandem dimer 4F-P-4F lipid nanodiscs. Lacking comprehensive local orientational restraints, we built models guided by our 14A-based nanodisc study and by previously reported NMR studies on related AAM peptide-lipid assemblies. To assess global size and shape, we computed small-angle X-ray

scattering (SAXS) profiles from MD snapshots and compared them with experimental data, constraining plausible disc sizes/morphologies and identifying sources of mismatch. Further, in collaboration with biophysical and biomedical groups studying 4F-P-4F lipid nanodiscs, we found that 4F-P-4F remains α-helical in free and lipidated form, forms stable peptide–lipid assemblies in aqueous solution, and shows calculated circular dichroism (CD) spectra consistent with measurements; MD identified key peptide–lipid contacts that confer stability. Functionally, these stable nanodiscs increased cholesterol efflux compared with free peptide and suppressed eosinophil chemotaxis and airway inflammation in vivo, underscoring their therapeutic potential.

In summary, we establish a protocol for the construction, simulation, and analysis of peptide–lipid nanodiscs. Our findings reveal the overall structural organization and the critical peptide–peptide and peptide–lipid interactions that govern nanodisc stability. These insights both deepen fundamental understanding and provide a framework for rationally designing next-generation apoA-I mimetics with therapeutic potential and for optimizing nanodiscs as versatile platforms for membrane-protein research.

Résumé

L'apolipoprotéine A-I (apoA-I) est la protéine principale des lipoprotéines de haute densité (HDL). Elle est un moteur du transport inverse du cholestérol (RCT) favorisant l'efflux via ABCA1 et la formation de HDL naissantes. Ses hélices amphipathiques en tandem stabilisent les bicouches lipidiques, et présente des activités antioxydantes, anti-inflammatoires et anti-athérogènes, soulignant sa pertinence cardiovasculaire. Toutefois, les essais visant à augmenter a quantité de HDL n'ont pas donné les bénéfices cliniques attendus, et l'apoA-I native pose des défis de fabrication et d'administration. Des peptides mimétiques (AAM), courtes hélices amphipathiques synthétiques, ont été développés pour reproduire les caractéristiques d'apoA-I. Ils s'auto-assemblent avec les lipides pour former des nanodisques utilisés en thérapies cardiovasculaires, en applications biomédicales et comme échafaudages pour la caractérisation de protéines membranaires.

Malgré de nombreux travaux, la structure, la dynamique et les propriétés physicochimiques des nanodisques restent partiellement connues. Cette thèse combine des simulations de dynamique moléculaire (MD) tout atome et des données expérimentales de nos collaborateurs pour fournir une vision atomistique de l'assemblages peptide-lipide mimétiques d'apoA-I à hélice α amphipathique. **L'objectif principal de cette thèse de doctorat est de fournir des informations atomistiques détaillées sur leur structure et leur dynamique, et d'élucider les interactions clés qui stabilisent ces assemblages peptide-lipide.**

Nous nous concentrons sur des dérivés cliniquement pertinents des peptides **18A: 14A, 4F et 4F-P-4F.** Les investigations débutent avec des nanodisques 14A : nous quantifions l'orientation du peptide autour des bicouches et identifions les interactions qui stabilisent la structure et sa dynamique. Les décalages chimiques ^{15}N et les éclatements quadrupolaires ^{2}H rétro-calculés concordent avec la RMN du solide antérieure, étayant une ceinture dimérique antiparallèle de 14A autour de la bicouche discoïdale. La stabilité découle d'un empilement aromatique π–π entre peptides et d'interactions électrostatiques et hydrophobes peptide-lipide, produisant des disques stables avec une hétérogénéité de l'ordre lipidique et de l'épaisseur de la bicouche du centre vers le bord, et apportant une preuve atomistique d'interactions stabilisantes précédemment hypothétisées.

Nous examinons ensuite 4F et son dimère en tandem 4F-P-4F. En l'absence de contraintes locales d'orientation exhaustives, nous construisons des modèles guidés par l'étude 14A et par des travaux de RMN publiés sur des AAM apparentés. Pour

évaluer la taille et la forme globales, nous calculons des profils de diffusion des rayons X aux petits angles (SAXS) à partir de conformations issues de la dynamique et les comparons à l'expérience, ce qui borne des tailles/morphologies plausibles et explique les écarts avec les spectres expérimentaux. En collaboration avec des équipes biophysiques et biomédicales, nous montrons que 4F-P-4F conserve son hélicité α en solution libre comme lipidée, forme des assemblages peptide-lipide stables dans l'eau et présente des spectres de dichroïsme circulaire (CD) calculés cohérents avec les mesures experience ; la MD identifie des contacts peptide-lipide clés stabilisant le nanodisque. Ces nanodisques augmentent l'efflux de cholestérol par rapport au peptide libre et réduisent la chimiotaxie des éosinophiles ainsi que l'inflammation des voies aériennes in vivo, soulignant leur potentiel thérapeutique.

Enfin, nous établissons un protocole pour construire, simuler et analyser des nanodisques peptide-lipide. Nos résultats révèlent l'organisation d'ensemble et les interactions essentielles peptide-peptide et peptide-lipide qui gouvernent la stabilité. Ces éclairages approfondissent la compréhension fondamentale et fournissent un cadre pour concevoir des mimétiques d'apoA-I de nouvelle génération à potentiel thérapeutique et optimiser les nanodisques comme plateformes polyvalentes pour l'étude des protéines membranaires.

List of Publications

1. Alankrita Rani, Denys Balandin, **Rohith Ravi**, Julia Teppan, Ivan Vidakovic, Melanie Kienzl, Thomas Bärnthaler et al. "Peptide-based lipid nanodiscs suppress eosinophil recruitment and chemotaxis." Journal of Controlled Release (2025): 114060.

2. **Rohith Ravi**, Evgeniy S. Salnikov, Burkhard Bechinger, Mounir Tarek. "Structural and dynamics of apoA-1 mimetic peptide lipid nanodisc assemblies: A molecular dynamics study" BBA-Biomembranes (2025): 184495.

List of Abbreviations

AAM	ApoA-I Mimetic
AAMLA	Apolipoprotein A-I Mimetic Peptide-Lipid Assemblies
ABCA1	ATP-Binding Cassette Subfamily A Member 1
ABCG1	ATP-Binding Cassette Subfamily G Member 1
apoA-I	Apolipoprotein A-I
ATP	Adenosine Triphosphate
CAD	Coronary Artery Disease
CD	Circular Dichroism
CETP	Cholesteryl Ester Transfer Protein
CG	Coarse-Grained
CVD	Cardiovascular Disease
DLS	Dynamic Light Scattering
DMPC	1,2-dimyristoyl-sn-glycero-3-phosphocholine
dHDL	Discoidal High-Density Lipoproteins
ELIC	*Erwinia* Ligand-Gated Ion Channel
HDL	High-Density Lipoproteins
HDL-C	High-Density Lipoprotein Cholesterol
HMR	Hydrogen Mass Repartitioning
IDL	Intermediate-Density Lipoproteins
IFT	Indirect Fourier Transform
LCAT	Lecithin-Cholesterol Acyltransferase
LDL	Low-Density Lipoproteins
LXR	Liver X Receptors
MD	Molecular Dynamics
MP	Membrane Protein
MSP	Membrane Scaffold Protein
nHDL	Nascent High-Density Lipoproteins
NMR	Nuclear Magnetic Resonance
PAGE	Polyacrylamide Gel Electrophoresis
PBC	Periodic Boundary Conditions
PLTP	Phospholipid Transfer Protein
PME	Particle-Mesh Ewald
pLGIC	Pentameric Ligand-Gated Ion Channel
RCT	Reverse Cholesterol Transport

RDF	Radial Distribution Function
Rg	Radius of Gyration
SANS	Small-Angle Neutron Scattering
SAXS	Small-Angle X-ray Scattering
SEC	Size-Exclusion Chromatography
sHDL	Synthetic High-Density Lipoproteins
SR-BI	Scavenger Receptor Class B Type I
ssNMR	Solid-State Nuclear Magnetic Resonance
TEM	Transmission Electron Microscopy
VLDL	Very-Low-Density Lipoproteins
WHO	World Health Organization

Contents

Abstract iii

Résumé v

List of Publications vii

List of Abbreviations ix

List of Figures xx

General Introduction 1

Research Objectives 2

Thesis Outline 3

Introduction générale 5

Objectifs de recherche 6

Plan de la thèse 7

1 Introduction 9
- 1.1 Lipoproteins . . . 10
- 1.2 HDL Metabolism and Cardiovascular Health . . . 12
  - 1.2.1 Reverse Cholestrol Transport . . . 12
- 1.3 Challenges in HDL Raising Therapies for CVDs . . . 14
- 1.4 Apolipoprotein A-I Mimetic Peptides (AAM) and synthetic-High Density Lipoproteins (sHDL): Therapeutic to CVD . . . 16
  - 1.4.1 AAM Nanodiscs: A tool for membrane protein characterization 18
- 1.5 Studying Nanodisc Assembly and Structure . . . 21

References . . . 23

2 Methods 35
- 2.1 Molecular Dynamics Simulations . . . 35
  - 2.1.1 Newtonian Framework in Molecular Dynamics . . . 36
  - 2.1.2 Ensembles of statistical thermodynamics . . . 37
  - 2.1.3 Ergodicity and Its Role in MD Sampling . . . 38

2.1.4 Numerical Integrators for MD Trajectories . . . 39
2.1.5 Force Fields and Potential Energy Functions . . . 40
2.1.6 Periodic Boundary Conditions and Long-range interactions . . 41
2.1.7 Thermostats . . . 43
2.1.7.1 Velocity randomizing algorithms (Andersen and SD thermostats): . . . 43
2.1.7.2 Velocity scaling algorithms (Berendsen, V-rescale and Nosé-Hoover thermostats): . . . 44
2.1.8 Barostats . . . 45
2.2 Building Peptide-based Nanodiscs . . . 46
2.2.1 Peptides of Interest . . . 47
2.2.2 Construction of Peptide-based Nanodiscs: *diskus.py* . . . 47
2.2.2.1 Peptide Orientation: . . . 47
2.2.2.2 Arranging the peptides and optimizing the belt . . . 48
2.2.2.3 Equilibrated lipid bilayer-slab to Lipid-disc . . . 50
2.2.2.4 Assembly and solvation . . . 50
2.2.3 Simulation Protocol . . . 51
2.3 Analysing Simulation . . . 52
2.3.1 Radius of Gyration (Rg) . . . 52
2.3.2 Radial Distribution Function (RDF) . . . 53
2.3.3 Atomic Mass Density Distribution . . . 53
2.3.4 DSSP algorithm and Helicity Calculation . . . 54
2.3.4.1 Calculation of Helicity (%) . . . 55
2.3.5 To Calculate the Interactions: Radial Density Distribution . . 55
2.3.6 Membrane Thickness and Lipid Order Parameter Calculations 56
2.3.6.1 Membrane Thickness: `thickness.py` . . . 56
2.3.6.2 Lipid Chain Order Parameter: `order.py` . . . 57
2.3.7 Calculation of ssNMR Parameters: ^{15}N-Chemical shift.py and ^{2}H Splitting.py . . . 58
2.3.8 Small Angle X-ray Scattering (SAXS) . . . 60
2.3.8.1 Model free analysis . . . 61
2.3.8.2 Guinier analysis . . . 61
2.3.8.3 Indirect Fourier Transform Method . . . 62
2.3.9 Small Angle X-ray Scattering from All-Atomic MD simulation: 64
2.3.9.1 GROMACS-SWAXS software details . . . 64
2.3.9.2 Atomic form factors . . . 65
2.3.9.3 Fitting procedure . . . 65
References . . . 66

3 Results **73**
3.1 Molecular Dynamics Simulations of 14A Peptide–Lipid Complexes: Comparison to NMR . . . 74
3.1.1 Computational Details . . . 74
3.1.2 Priliminary Analysis . . . 75
3.1.3 Validation of 14 Peptide Orientation with ssNMR Observation 76

3.1.4 Uncover the Interactions that Stabilize 14A Peptide-Lipid Assemblies . . . 80
3.1.4.1 Peptide-peptide interactions . . . 80
3.1.4.2 Lipid-peptide interactions . . . 83
3.1.4.3 Lipid properties of 14A peptide nanodiscs at different temperature . . . 86
3.1.5 Discussion . . . 90
3.2 ApoA-I Mimetic Peptides Nanodisc MD Simulation: Comparing with SAXS Data . . . 92
3.2.1 Computational Details . . . 92
3.2.2 Comparing Theoretical SAXS Curves Across Different Peptide Scaffold Nanodiscs of Similar Size . . . 95
3.2.3 Preliminary Data Analysis on Experimental SAXS Curves . . . 98
3.2.4 Analysis of Polydispersity and Size Effects on SAXS Profiles . . . 101
3.2.4.1 Assuming Gaussian distribution of sizes to address polydispersity . . . 105
3.2.5 Cross-system Comparison of the SAXS Profiles . . . 106
3.2.6 Discussion . . . 110
3.3 4F-P-4F Synthetic HDL Nanodiscs and Biological Assay . . . 112
3.3.1 Computational Details . . . 112
3.3.2 Characteriszation of 4F-P-4F Nanodiscs . . . 113
3.3.2.1 Rationale and nanodisc construction . . . 113
3.3.2.2 Comparison of MD simulation and experiment CD spectra . . . 114
3.3.2.3 Lipid-peptide Interactions . . . 114
3.3.3 sHDL Structural Relation to Cholesterol Efflux . . . 117
3.3.4 Discussion . . . 117
References . . . 119

4 Conclusion and Perspectives **127**
4.1 Conclusion . . . 127
4.2 Perspectives . . . 130
References . . . 131

5 Appendix **135**
5.1 Optimization of 14A Dimeric Antiparallel Arrangement . . . 135
5.2 Orientation of the Side Chain . . . 137
5.3 Gaussian Distribution of Sizes of Nanodiscs to Introduce the Polydispersity . . . 139
References . . . 142

List of Figures

1.1 Lipoprotein particles comprise a hydrophobic core enriched in triacylglycerols and cholesteryl esters, surrounded by phospholipids and unesterified cholesterol that is stabilized by apolipoproteins. Variations in particle size and composition give rise to the classical categories: chylomicrons (CM), very-low-density (VLDL), intermediate-density (IDL), low-density (LDL), and high-density (HDL) lipoproteins. Representative apolipoproteins include apoA1, apoB, and apoE. Reported percentages refer to weight fractions. Figure adapted from [4]. 11
1.2 Pictorial representation of truncated human apolipoprotein A-I (apoA-I), the major protein component of high-density lipoprotein (HDL). apoA-I is composed almost entirely of a pseudo-continuous amphipathic α-helix, punctuated by kinks at regularly spaced proline residues. The structure comprises residues 44–243 (exon 4) of apoA-I and is taken from the Protein Data Bank (PDB ID: 1AV1). 13
1.3 Schematic representation of Reverse Cholesterol Transport (RCT) and lipid metabolism. This figure is adapted from [28]. 15
1.4 Schematic representation of the ApoA–I mimetic peptides studied in this thesis: (A) 14A, (B) 4F, and (C) 4F-P-4F. 19

2.1 Illustration of periodic boundary conditions (PBC) in a molecular simulation. A finite number of atoms is modeled within a central simulation cell, which is replicated in all three spatial directions to approximate bulk behavior and minimize finite-size effects. For clarity, only the two in-plane periodic images (x–y plane) surrounding the primary cell are shown. 42
2.2 Measured length of an input peptide, which consists of two α-helical monomers. 48
2.3 Left: Diagram explaining the rotation and translation of each dimer in the initial configuration. Right: Initial configuration of a belt with 10 proteins. Several collisions are visible (highlighted in red). 49
2.4 Optimized configuration of a belt with 10 proteins. The collisions from Figure 2.3 have been resolved (highlighted in red) by increasing the radius of the belt. 50

2.5 The picture illustrates a two-part continuous process. In Part 1, the assembly of nanodiscs is depicted, showing their sequential formation. Part 2 demonstrates the use of Packmol for the organized packing of water and ions around the assembled nanodiscs. 51
2.6 Pictorial representation of the method used to compute ^{2}H quadrupolar splitting and ^{15}N chemical-shift anisotropy (CSA). **(A)** The ^{2}H splitting is obtained from the angle θ between the $C_\alpha - C_\beta$ bond vector and the magnetic-field direction $\mathbf{B}_0$. **(B)** The ^{15}N CSA tensor is shown in its principal-axis system placed next to the molecular frame of the peptide-bond. ^{15}N chemical shift is obtained by determining the polar (Θ) and azimuthal (Φ) angles of $\mathbf{B}_0$ within the molecular frame relative to the principal axes of the CSA tensor. Axes $\vec{\sigma}_{11}$ and $\vec{\sigma}_{33}$ lie in the peptide plane within the plane of the paper, while $\vec{\sigma}_{22}$ is perpendicular to it. Θ is measured between $\vec{\sigma}_{33}$ and $\mathbf{B}_0$, and Φ is measured between the $\vec{\sigma}_{11}$ and the projection of $\mathbf{B}_0$. 59

3.1 (A) Radius of gyration (Rg) for System A and its replicas at 30°C and 37°C, individually plotted over 1µs. System A comprises 24 (14A) peptides and 186 DMPC lipids. (B) Radius of gyration for System B at 30°C and 37°C, plotted over 400ns. 76
3.2 Pictorial representation of 14A/DMPC nanodiscs. (A) System A: final snapshot from a 1 μs MD trajectory at 37 ° C (Replica 1). (B) System B: final snapshot from a 400 ns MD trajectory at 37 ° C. . . . 77
3.3 ^{2}H quadrupole splittings vs angle (ϑ) plot where X-axis represent the angle between 0 to 180 degree and the Y-axis represents the corresponding splitting values in kHz.The dotted blue line marks the magic angle and the corresponding splitting value. 79
3.4 (A) Schematic depiction of peptide interactions illustrating both the formation of dimeric units and the lateral contacts established between adjacent dimers. (B) Free energy profile of tyrosine residues (Y7) located at the dimer interfaces for system A, while (D) shows the corresponding profile for system B. (C) Free energy profile of phenylalanine residues (F14), which mediate lateral interactions between neighboring dimer blocks in system A, while (E) shows the corresponding profile for system B. 82
3.5 Cutoff distances for counting salt bridges were determined from radial distribution functions: (A) 4.7 Å between the nitrogen of the amino group in lysine (9K) side chains and the phosphorus of DMPC molecules; (B) 5.7 Å between the carbon of the carboxyl group in glutamic acid (12E) side chains and the nitrogen of DMPC molecules; (C) 5.7 Å between the hydroxyl group at the para position of tyrosine (2Y) and the nitrogen of DMPC molecules. 84

3.6 Representation of system A configuration sampled during molecular dynamics (MD) simulation, highlighting key interactions and orientations. (A) Salt bridge interactions between peptides and lipid head groups: a lysine (K9) – phosphate salt bridge formed by interactions between the amino group (NH_3^+) of the lysine (blue) and the phosphate group of DMPC (orange), and a glutamic acid (E12) – choline salt bridge formed by interactions between the glutamate carboxyl group (red) and choline group of DMPC (yellow). (B) Orientation of aromatic residues along the bilayer normal, with tyrosine (green) and phenylalanine (red) rings aligned nearly parallel to the membrane normal. Additionally, a salt bridge interaction is observed between the hydroxyl group (red ball) in the para position of the tyrosine aromatic ring and the choline group of the DMPC (yellow). (C) Probability distribution of the aromatic ring normal orientations for tyrosine and phenylalanine within the 0°–180° range of system A. 85
3.7 Probability density distribution of the aromatic ring normal orientations for tyrosine and phenylalanine within the 0°–180° range. These plots were obtained from the system B simulation. 86
3.8 Mass density profiles of nanodiscs with varying peptide and lipid compositions. (A–F): System A; panels (A–C) correspond to simulations at 30°C, and (D–F) at 37°C. (G, H): System B; (G) at 30°C and (H) at 37°C. The plots show lipid and peptide mass density distributions along the x and y axes. "Lipid x" and "Lipid y" denote lipid densities along the respective axes, while "Peptide x" and "Peptide y" show peptide mass densities. These profiles were used to calculate the average nanodisc diameter for each system (see section:2.3.3). . . 88
3.9 2D maps of bilayer thickness (left panels), average lipid order parameters calculated over all C–H bonds in the two aliphatic tails of DMPC lipids (center panels), and order parameters as a function of carbon position along the lipid tails (right panels). The rim zone is defined as all lipids within 10 Å of the 14A peptides, while the core zone includes all lipids located beyond this distance. Panels (A) and (B) correspond to System A, simulated at 30°C and 37°C, respectively. Panels (C) and (D) correspond to System B, simulated at 30°C and 37°C, respectively. 89
3.10 Pictorial representation of 4F/DMPC and 4F–P–4F/DMPC nanodiscs. (A) System B2 (4F/DMPC). (B) System C1 (4F–P–4F/DMPC). . . . 96
3.11 Mass density distribution profiles of 14A, 4F and 4F-P-4F nanodiscs.(A): System A1, and (B): System B2, (C): System C1. The plots show lipid and peptide mass density distributions along the x and y axes. "Lipid x" and "Lipid y" denote lipid densities along the respective axes, while "Peptide x" and "Peptide y" show peptide mass densities (see section: 2.3.3). These profiles were used to calculate the average nanodisc diameter for each system. 97
3.12 Calculated Small-angle scattering curves of system A1, B2, C1. The curves are vertically separated for clarity. 97

3.13 Pair-distance distribution functions, P(r), obtained by indirect Fourier transform (IFT) of the corresponding SAXS curves for systems A1 (14/DMPC), B2 (4F/DMPC), and C1 (4F-P-4F/DMPC). The inferred D_{max} for each system are derived from the respective P(r) profiles 98
3.14 Experimental SAXS profiles for 4F/DMPC and 4F-P-4F/DMPC. (A) Intensity plotted as $\log I$ vs. q. (B) Intensity plotted as $\log I$ vs. $\log q$, the gray box highlights the deviation in the SAXS profiles. (C) Guinier analysis for the 4F–P4F/DMPC sample ($\ln I$ vs. q^2). (D) Guinier analysis for the 4F/DMPC sample. (E) Pair-distance distribution functions $P(r)$ obtained by indirect Fourier transform (IFT) of the respective SAXS profiles, used to estimate the maximum particle dimension $D_{\max}$. 100
3.15 Calculated SAXS profiles from MD simulations using GROMACS-SWAXS, plotted as $\log I(q)$ vs. $\log q$. (A) Normalized SAXS curves of the 4F/DMPC systems. (B) Normalized SAXS curves of the 4F-P-4F/DMPC systems. A gradient color scheme is used to highlight differences among the curves. 103
3.16 Comparison of calculated SAXS curves with experimental data. (A) Calculated SAXS curves for B11 and B12 overlaid with the experimental 4F/DMPC profile. (B) Calculated SAXS curves for C4 and C5 overlaid with the experimental 4F-P-4F/DMPC profile. (C) Pair-distance distribution $P(r)$ for B11, B12, and the experimental 4F/DMPC data. (D) Pair-distance distribution $P(r)$ for C4, C5, and the experimental 4F-P-4F/DMPC data. *Note:* For panels (A) and (B), intensities were normalized as I/I_0; for panels (C) and (D), $P(r)$ curves were area-normalized to enable fair comparison. 104
3.17 **Polydisperse theoretical SAXS profile at B12 (25.4 nm).** The theoretical SAXS profile corresponds to a Gaussian size distribution with mean 25.4 nm (B12) and standard deviation $\sigma = 3$ (size bins). Fitted to the 4F/DMPC* experimental data using a single global scale factor C (Section: 2.3.9.3.) and plotted as a log–log scale as $\log I(q)$ versus $\log q$, with q in nm^{-1}. 106
3.18 Each SAXS curve computed from the 4F/DMPC MD simulations was fitted to the experimental SAXS data of the 18A/DMPC nanodisc and plotted as $\log I(q)$ vs. $\log q$. Experimental SAXS data taken form Midtgaard et al [26]. The fitting procedure is described in Section: 2.3.9.3. 108
3.19 Calculated SAXS profile of B1 (4F/DMPC) fitted with the 18A/DMPC* model, plotted as $\log I(q)$ vs. $\log q$ (with q in $\mathrm{Å}^{-1}$). Experimental SAXS data are from Midtgaard et al.[26]. The fitting procedure is described in Section 2.3.9.3. 109

3.20 Far UV CD spectra comparing the structural characteristics of the sHDL formulation and the non-lipidated 4F-P-4F peptide. Both experimental spectra and MD-derived spectra are shown. The mean-residue molar ellipticity at 222 nm, $[\theta]_{222}$, was obtained by converting the molar circular dichroism spectra $\Delta\varepsilon(\lambda)$ using $[\theta] = 3298\,\Delta\varepsilon$, and the percent α-helicity was computed using Eq. 3.5. 4F-P-4F* and 4F-P-4F/DMPC* are experimental curves, and the remaining systems are from MD-derived spectra. 114
3.21 Mass density distribution profiles of 4F-P-4F nanodiscs.(A): System A, and (B): System B, (C): System C. The plots show lipid and peptide mass density distributions along the x and y axes. "Lipid x" and "Lipid y" denote lipid densities along the respective axes, while "Peptide x" and "Peptide y" show peptide mass densities (see section: 2.3.3). These profiles were used to calculate the average nanodisc diameter for each system. 115
3.22 Molecular dynamics simulation of sHDL nanodiscs. A. Snapshot of system A (4F-P-4F/DMPC) from the MD trajectory illustrating peptide–lipid salt bridges: (i) a lysine–phosphate interaction between the lysine amine nitrogen (blue) and the lipid phosphate phosphorus (orange); (ii) a glutamate–choline interaction between the glutamate carboxylate (white) and the choline nitrogen of the lipid headgroup (yellow). B–C. Alternative orientations highlighting hydrophobic (white) and hydrophilic (pink) residues of the 4F-P-4F dimers, emphasizing the amphipathic side-chain patterning and their positioning relative to the lipid core and surrounding solvent. 116
3.23 ^{3}H-cholesterol efflux from isolated human eosinophils, expressed as the percentage of total ^{3}H-cholesterol released following treatment with sHDL (25 µg/mL) or 4F-P-4F (25 µg/mL). Data are presented as mean ± SEM from three independent experiments; statistical significance was assessed using Student's t-test. Data adapted from our collaborative study [37]. 118

5.1 **(A)** Schematic of the collaborator-proposed 14A dimer configuration. **(B)** Representative snapshot showing collapse of the dimer at the nanodisc rim after restraint release. **(C)** Time series of the distance between the centers of mass of the Tyr7 aromatic rings over 500 ns. **(D)** Antiparallel, head-to-tail dimer configuration that satisfies our structural criteria. **(E)** Pictorial representation of a stable 14A-peptide nanodisc after a 1 μs simulation at 37 °C. 136
5.2 Pictorial representation of the method used to calculate the orientation of 14A peptide sidechain aromatic rings relative to the membrane axes. The aromatic ring plane is aligned parallel to the z-axis, with its normal oriented perpendicular to the membrane plane. The calculation was performed by measuring the angle between the aromatic ring normal and the membrane normal. 138

5.3 **Polydisperse theoretical SAXS profiles for 4F/DPMC.** Each panel (B1–B15) corresponds to a Gaussian size distribution with the mean centered on the indicated system and standard deviation $\sigma = 3$. The resulting polydisperse profiles are fit to the experimental data using a single global scale factor C and plotted on a log–log scale as $\log I(q)$ versus $\log q$, with q in nm^{-1}. 141

General Introduction

This PhD thesis forms part of the France–Austria research project AAMLA *(Apolipoprotein A-I Mimetic Peptide–Lipid Assemblies)*, funded by Agence Nationale de la Recherche (ANR) and Austrian Science Fund (German: Fonds zur Forderung der wissenschaftlichen Forschung, FWF). Within this interdisciplinary program, we aim to establish a rigorous physicochemical understanding of high-density lipoproteins (HDL) mimetic peptide–lipid nanoparticles, linking their structure and dynamics to biological function and ultimately informing the design of improved candidates for future cardiovascular therapies. Our contribution centers on computation: we have built and validated molecular models of peptide–lipid assemblies using large-scale all-atom molecular dynamics (MD) simulations in close dialogue with experimental collaborators, leveraging small-angle X-ray scattering (SAXS) and nuclear magnetic resonance (NMR) to corroborate and test our models.

Biological motivation Apolipoprotein A-I (apoA-I) is the principal protein component of plasma HDL and a key effector in reverse cholesterol transport (RCT), which removes excess cholesterol from peripheral tissues to the liver for excretion. ApoA-I promotes cholesterol efflux via interactions with membrane transporters such as ABCA1, becomes lipidated, and forms nascent HDL particles. Its tandem amphipathic α-helical domains stabilize phospholipid bilayers and enable HDL to solubilize and transport lipids. Beyond RCT, apoA-I exhibits antioxidant, anti-inflammatory, and anti-atherogenic activities, making it central to cardiovascular health.

Why mimetics?

Clinical strategies that simply elevate HDL-cholesterol have not delivered the expected reductions in cardiovascular risk, and native apoA-I ($\approx$28 kDa), which presents significant manufacturing challenges. Its production is complex, often relying on plasma-derived sources, and requires intravenous delivery, which raises concerns regarding cost, safety, and patient compliance. To overcome these limitations, apoA-1 mimetic (AAM) peptides have been developed over the decades. These are short, synthetic peptides designed to replicate the structure and biological properties of full-length apoA-1. They have shown beneficial effects in various animal disease models, including atherosclerosis. Moreover, these peptides can self-assemble with lipids to form peptide–lipid nanodisc assemblies, precursors of HDL particles. Due

to their relative ease of synthesis and their ability to provide a native-like, detergent-free bilayer environment, these peptide-lipid assemblies serve as excellent platforms for the biophysical characterization of membrane proteins.

Knowledge gap: Despite intense interest, the supramolecular architecture, molecular organization, and dynamic behavior of AAM peptide–lipid nanodiscs remain largely unexplored. Open questions include: How are helices oriented and packed? Which peptide–lipid and peptide–peptide interactions stabilize the assemblies? How do these structural features relate to functional readouts relevant to HDL biology?

Our approach: We address these questions using all-atom MD simulations tightly integrated with experiment. We focus on clinically relevant derivatives of the canonical class-A amphipathic helix 18A—specifically 14A, 4F, and 4F-P-4F—and construct their complexes with 1,2-dimyristoyl-sn-glycero-3-phosphocholine (DMPC). We generate long MD trajectories to probe equilibrium structure and dynamics, compute SAXS profiles and NMR-relevant observables for direct comparison with experimental data, and dissect interaction networks to identify sequence features that stabilize the assemblies.

Scope and Contributions:

Within AAMLA, we contribute (i) atomistic models of AAM peptide–DMPC nanodiscs, (ii) quantitative validation against SAXS and NMR, and (iii) mechanistic insight linking sequence, interfacial chemistry, and supramolecular stability. By combining simulations with experiment, we aim to bridge length- and time-scales that are difficult to access by either approach alone and to deliver design principles for next-generation mimetic peptides.

Research Objectives

We organize our work around the following questions:

1. What is the supramolecular architecture (size, shape, stoichiometry) of AAM-DMPC nanodiscs?
2. How are peptides arranged relative to the bilayer, what are the key dynamics, and do MD-derived SAXS/NMR observables agree with experiment?
3. Which peptide–lipid and peptide–peptide interactions most strongly stabilize the assemblies?

Thesis Outline

The manuscript is structured into several chapters, each addressing a critical component of the research.

Chapter 1: Introduction We introduce plasma lipoproteins with an emphasis on high-density lipoproteins (HDL). We summarise HDL structure, metabolism, and its roles in reverse cholesterol transport (RCT), as well as its antioxidant, anti-inflammatory, and antithrombotic activities. This context clarifies how remodeling processes shape HDL functional heterogeneity and why strategies that merely raise HDL-cholesterol have not consistently improved clinical outcomes—motivating a shift toward HDL *functionality*. We focus on apolipoprotein A-I (apoA-I) mimetic peptides and synthetic HDL (sHDL), highlighting their ability to form tunable peptide–lipid nanodiscs that mimic native bilayers, with both therapeutic relevance and utility as biophysical platforms. A brief survey of NMR, SAXS, and molecular dynamics literature identifies open questions on peptide registry at the rim, peptide–peptide and peptide–lipid interactions, and local lipid environments. This state-of-the-art, centered on clinically relevant 18A-derived sequences (14A, 4F, and 4F–P–4F), sets the stage for the following chapters.

Chapter 2: Methods We detail the methodology used to investigate nanodisc structure, dynamics, and morphology. We outline the classical MD framework (equations of motion, statistical ensembles, ergodicity, integrators) and practical choices for force fields, long-range electrostatics, and thermostat/barostat schemes. We then describe nanodisc construction using the custom `diskus.py` tool and simulation setup in `GROMACS` (CHARMM36m, hydrogen-mass repartitioning, NVT/NPT equilibration, production conditions). We summarise how observables are computed and, where applicable, compared with experiment: global size measures (radius of gyration and density-based diameters); peptide–lipid interactions (RDF-informed cutoffs and interaction counts); peptide secondary structure (DSSP helicity); membrane organisation (thickness and acyl-chain order maps); and ssNMR observables (^{2}H quadrupolar splittings and ^{15}N chemical shifts). Finally, we describe SAXS: calculation of SAXS profiles from explicit-solvent MD using `GROMACS-SWAXS`, and analysis of SAXS curves via Guinier plots and indirect Fourier transform (`GNOM`) to obtain R_g, $I(0)$, and $D_{\max}$.

Chapter 3: Results We used MD simulations, complemented by experiments from collaborators, to determine how apoA-I mimetic peptides organize and stabilize discoidal lipid bilayers and how this supramolecular architecture links to function. We study three scaffolds—14A, 4F, and tandem 4F–P–4F with DMPC, and benchmark simulations against experiment using ssNMR observables, SAXS profiles, pair-distance distribution functions $p(r)$, and CD spectra. The chapter comprises three sections:

- **Section 3.1:** Results for 14A/DMPC nanodisc structure, stability, and dynamics. We computed ^{15}N chemical shifts and ^{2}H quadrupolar splittings from trajectories and compared with prior ssNMR measurements to quantify peptide orientation around the lipid bilayer, and we characterized key peptide–peptide and peptide–lipid interactions underpinning stability.
- **Section 3.2:** Extension to 4F/DMPC and 4F–P–4F/DMPC nanodiscs. In the absence of comprehensive local orientational restraints, we build models guided by the 14A study and prior NMR on related mimetics. We computed SAXS from MD snapshots, compared to experiment to constrain nanodisc sizes/morphologies, and analyzed sources of mismatch.
- **Section 3.3:** we present collaborative work in which we characterized the 4F–P–4F/DMPC nanodiscs in structural detail and examined their potential biological relevance. We computed CD spectra from MD snapshots that agree with experiment and use MD simulations to reveal persistent peptide–lipid contacts that stabilize the nanodisc. We attempted to provide structural relevance to the biological function, especially regarding cholesterol efflux.

Chapter 4: Conclusions and Perspectives We provide a research summary, the main conclusions, and an outline of perspectives for future work.

Introduction générale

Cette thèse de doctorat s'inscrit dans le projet de recherche franco-autrichien AAMLA *(Assemblages peptide–lipide mimétiques de l'apolipoprotéine A-I)*, financé par l'Agence Nationale de la Recherche (ANR) et le Fonds autrichien pour la science (en allemand : *Fonds zur Förderung der wissenschaftlichen Forschung*, FWF). Au sein de ce programme interdisciplinaire, nous visons à établir une compréhension physico-chimique rigoureuse des nanoparticules peptide–lipide mimant les lipoprotéines plasmatiques de haute densité (HDL), en reliant leur structure et leur dynamique à leur fonction biologique, afin d'éclairer la conception de meilleurs candidats pour de futures thérapies cardiovasculaires. Notre contribution se centre sur la simulation de ces systèmes : nous avons construit des modèles moléculaires d'assemblages peptide–lipide à l'aide de simulations de dynamique moléculaire (MD) tout-atome à grande échelle. Nous les avons testé et validé en exploitant la diffusion des rayons X aux petits angles (SAXS) et la résonance magnétique nucléaire (RMN), en étroite interaction avec des collaborateurs expérimentateurs.

Motivation biologique L'apolipoprotéine A-I (apoA-I) est le principal constituant protéique des HDL et un acteur clé du transport inverse du cholestérol (RCT), qui élimine l'excès de cholestérol des tissus périphériques vers le foie pour excrétion. L'apoA-I favorise l'efflux de cholestérol via des interactions avec des transporteurs membranaires tels que ABCA1. Il devient lipidée et forme des particules de HDL naissantes. Ses domaines α-hélicoïdaux amphiphiles en tandem stabilisent les bicouches phospholipidiques et permettent aux HDL de solubiliser et transporter les lipides. Au-delà du RCT, l'apoA-I présente des activités antioxydantes, anti-inflammatoires et anti-athérogènes, la plaçant au cœur de la santé cardiovasculaire.

Pourquoi des mimétiques ?

Les stratégies cliniques qui se contentent d'augmenter le cholestérol HDL n'ont pas apporté les réductions de risque cardiovasculaire attendues, et l'apoA-I native (≈28 kDa) pose d'importants défis de fabrication. Sa production est complexe, reposant souvent sur des sources d'origine plasmatique, et nécessite une administration intraveineuse. Ceci soulève des questions de coût, de sécurité et d'adhésion des patients. Pour surmonter ces limitations, des peptides mimétiques d'apoA-1 (AAM) ont été développés au fil des décennies. Il s'agit de peptides courts et synthétiques conçus pour reproduire la structure et les propriétés biologiques de l'ApoA-1. Ils ont montré des effets bénéfiques dans divers modèles de pathologie animale, notamment

l'athérosclérose. De plus, ces peptides peuvent s'auto-assembler avec des lipides pour former des nanodisques peptide–lipide, précurseurs des particules de HDL. En raison de leur relative facilité de synthèse et de leur capacité à fournir un environnement de bicouche, sans tensioactif, proche de la protéine native, ces assemblages peptide–lipide constituent d'excellentes plateformes pour la caractérisation biophysique des protéines membranaires.

Lacunes de connaissances : Malgré un vif intérêt, l'architecture supramoléculaire, l'organisation moléculaire et le comportement dynamique des nanodisques peptide–lipide AAM restent en grande partie inexplorés. Les questions ouvertes incluent : Comment les hélices sont-elles orientées et empaquetées ? Quelles interactions peptide–lipide et peptide–peptide stabilisent ces assemblages ? Comment ces caractéristiques structurelles se relient-elles à des lectures fonctionnelles pertinentes pour la biologie des HDL ?

Notre approche : Nous abordons ces questions à l'aide de MD tout-atome étroitement mise en relation à l'expérience. Nous nous concentrons sur des dérivés cliniquement pertinents de l'hélice amphipathique de classe A canonique 18A spécifiquement 14A, 4F et 4F–P–4F—et construisons leurs complexes avec la 1,2-dimyristoyl-sn-glycéro-3-phosphocholine (DMPC). De longues trajectoires de MD sont générées pour sonder la structure et la dynamique d'équilibre des nanodisques. À partir d'elles, des profils SAXS et des observables pertinentes pour la RMN sont calculés en vue d'une comparaison directe avec les données expérimentales. Des réseaux d'interactions sont déterminés et disséqué afin d'identifier les caractéristiques de séquence qui stabilisent les assemblages.

Portée et contributions :

Dans le cadre d'AAMLA, nous apportons (i) des modèles atomistiques de nanodisques peptide AAM–DMPC, (ii) une validation quantitative par SAXS et RMN, et (iii) un éclairage mécanistique reliant leur séquence, leur chimie interfaciale et leur stabilité supramoléculaire. En combinant simulations et expériences, nous visons à combler les échelles de longueur et de temps difficiles d'accès par l'une ou l'autre approche seule, et à dégager des principes de conception pour des peptides mimétiques de nouvelle génération.

Objectifs de recherche

Nous structurons notre travail autour des questions suivantes :

1. Quelle est l'architecture supramoléculaire (taille, forme, stœchiométrie) des nanodisques AAM–DMPC ?
2. Comment les peptides sont-ils arrangés par rapport à la bicouche, quelles sont les dynamiques clés, et est-ce que les observables SAXS/RMN issues des MD

concordent-elles avec l'expérience ?

3. Quelles interactions peptide–lipide et peptide–peptide stabilisent le plus fortement les assemblages ?

Plan de la thèse

Le manuscrit est structuré en plusieurs chapitres, chacun abordant un volet essentiel de la recherche.

Chapitre 1 : Introduction Nous présentons les lipoprotéines plasmatiques en mettant l'accent sur les lipoprotéines de haute densité (HDL). Nous résumons la structure des HDL, leur métabolisme et leurs rôles dans le transport inverse du cholestérol (RCT), ainsi que leurs activités antioxydantes, anti-inflammatoires et antithrombotiques. Ce contexte clarifie comment les processus de remodelage façonnent l'hétérogénéité fonctionnelle des HDL et pourquoi les stratégies se limitant à augmenter le cholestérol HDL n'ont pas systématiquement amélioré les résultats cliniques. Ceci motive un recentrage vers la *fonctionnalité* des HDL. Nous nous concentrons sur les peptides mimétiques de l'apolipoprotéine A-I (apoA-I) et les HDL synthétiques (sHDL), en soulignant leur capacité à former des nanodisques peptide–lipide modulables qui miment des bicouches natives, avec une double pertinence thérapeutique et utilité comme plateformes biophysiques. Un bref état de l'art de la RMN, de la SAXS et de la dynamique moléculaire identifie des questions ouvertes concernant l'organisation des peptides sur le pourtour, les interactions peptide–peptide et peptide–lipide, ainsi que les environnements lipidiques locaux. Cet état de l'art, centré sur des séquences dérivées de 18A pertinentes cliniquement (14A, 4F et 4F–P–4F), prépare les chapitres suivants.

Chapitre 2 : Méthodes Nous détaillons la méthodologie employée pour étudier la structure, la dynamique et la morphologie des nanodisques. Nous exposons le cadre de la MD classique (équations du mouvement, ensembles statistiques, ergodicité, intégrateurs) et les choix pratiques concernant les champs de force, l'électrostatique à longue portée et les schémas de thermostat/barostat. Nous décrivons ensuite la construction des nanodisques à l'aide de l'outil sur mesure `diskus.py` et la mise en place des simulations dans `GROMACS` (CHARMM36m, répartition de la masse de l'hydrogène, équilibration NVT/NPT, conditions de production). Nous résumons la façon dont les observables sont calculées et, le cas échéant, comparées à l'expérience : mesures globales de taille (rayon de giration et diamètres fondés sur la densité) ; interactions peptide–lipide (seuils guidés par les fonctions de distribution radiale (RDF) et comptages des interactions) ; structure secondaire peptidique (hélicité DSSP) ; organisation membranaire (cartes d'épaisseur et d'ordre des chaînes acyles) ; et observables de RMN du solide (ssRMN) (éclatements quadrupolaires ^{2}H et déplacements chimiques ^{15}N). Enfin, nous décrivons la SAXS : calcul des

profils SAXS à partir de MD en solvant explicite avec `GROMACS-SWAXS`, et analyse des courbes SAXS via les tracés de Guinier et la transformée de Fourier indirecte (`GNOM`) pour obtenir R_g, $I(0)$ et $D_{\max}$.

Chapitre 3 : Résultats Nous avons utilisé des simulations de MD, complétées par des expériences réalisées par des collaborateurs, pour déterminer comment des peptides mimétiques d'apoA-I organisent et stabilisent des bicouches lipidiques discoïdales, et comment cette architecture supramoléculaire se relie leur fonction. Nous étudions trois échafaudages—14A, 4F et le tandem 4F–P–4F avec DMPC—et confrontons les simulations à l'expérience au moyen d'observables de RMN du solide, de profils SAXS, de fonctions de distribution des distances par paires $p(r)$ et de spectres de dichroïsme circulaire (CD). Le chapitre comprend trois sections :

- **Section 3.1 :** Résultats sur la structure, la stabilité et la dynamique des nanodisques 14A/DMPC. Nous avons calculé les déplacements chimiques ^{15}N et les éclatements quadrupolaires ^{2}H à partir des trajectoires et les avons comparés à des mesures antérieures de RMN du solide pour quantifier l'orientation des peptides autour de la bicouche lipidique, et nous avons caractérisé les interactions peptide–peptide et peptide–lipide clés qui sous-tendent la stabilité.
- **Section 3.2 :** Extension aux nanodisques 4F/DMPC et 4F–P–4F/DMPC. En l'absence de contraintes d'orientation locales exhaustives, nous avons construit des modèles guidés par l'étude 14A et par des travaux de RMN antérieurs sur des mimétiques apparentés. Nous avons calculé la SAXS à partir d'instantanés de DM, comparé aux expériences pour contraindre tailles/morphologies des nanodisques et analysé les sources de divergence.
- **Section 3.3 :** Nous présentons un travail collaboratif dans lequel nous avons caractérisé en détail les nanodisques 4F–P–4F/DMPC et examiné leur pertinence biologique potentielle. Nous avons calculé des spectres de CD à partir d'instantanés de MD qui concordent avec l'expérience et utilisé des simulations de MD pour révéler des contacts peptide–lipide persistants stabilisant le nanodisque. Nous avons cherché à relier la structure à la fonction biologique, en particulier en ce qui concerne l'efflux de cholestérol.

Chapitre 4 : Conclusions et perspectives Nous proposons une synthèse des travaux, les principales conclusions et des perspectives pour les recherches futures.

1 Introduction

This chapter provides a comprehensive overview of high-density lipoproteins (HDL) and their structural and functional significance, while introducing the apoA-I mimetic peptide nanodisc systems that form the basis of this thesis. It began with a broader introduction to plasma lipoproteins, outlining their supramolecular organization, classification, and roles in lipid transport. Particular emphasis was placed on HDL particles, which play a central role in reverse cholesterol transport (RCT) and exert multiple protective effects antioxidant, anti-inflammatory, and antithrombotic making them key determinants of cardiovascular health.

HDL metabolism is then examined in detail, describing the molecular mechanisms that govern cholesterol efflux, esterification, and hepatic clearance, and highlighting how HDL remodeling contributes to functional heterogeneity. The chapter reviews why clinical strategies designed to raise HDL-cholesterol (HDL-C) largely failed to improve cardiovascular outcomes. These findings shifted the field's focus from HDL quantity to HDL functionality, motivating alternative approaches. Among these were the development of apolipoprotein A-I mimetic peptides (AAMs) and synthetic HDL (sHDL) that replicate key structural and functional properties of native HDL, as well as strategies aimed at enhancing endogenous cholesterol-efflux pathways (e.g., ABCA1/ABCG1 upregulation). Beyond their therapeutic potential, peptide–lipid assemblies can form tunable nanodiscs that mimic native bilayers and provide versatile platforms for studying membrane proteins in near-physiological lipid environments.

Finally, the chapter surveys relevant experimental findings (e.g., NMR and SAXS) together with the existing molecular dynamics (MD) simulation literature on HDL-like and mimetic nanodiscs, delineating open questions regarding peptide registry at the rim, peptide–peptide and lipid–peptide interactions, and the local lipid environment within the discs. In this thesis, we focused on clinically relevant derivatives of 18A peptides — namely, 14A, 4F, and 4F-P-4F — which have attracted considerable biomedical interest. This focused review, together with state-of-the-art molecular modeling and MD simulations, provides a solid foundation for the subsequent chapters.

1.1 Lipoproteins

Lipoproteins are supramolecular nanostructures that serve as the primary transport vehicles for plasma lipids. Because plasma lipids such as cholesterol and triglycerides are insoluble in water, they must be carried in association with specific proteins known as apoproteins. Together, these components form complex macromolecular assemblies that enable lipid transport and metabolism [1–3].

Structurally, lipoproteins consist of a hydrophobic core composed mainly of triglycerides and cholesterol esters, surrounded by an amphipathic shell of phospholipids, free cholesterol, and apoproteins. Fatty acids derived from triglycerides can be used for energy production or stored for later use, while cholesterol plays essential roles in steroid hormone biosynthesis, membrane architecture, and bile acid formation. Apoproteins are central to lipoprotein function: they provide structural stability, regulate lipid metabolism, and act as ligands for receptor-mediated uptake. Based on their size, density, lipid composition, and apoprotein content, plasma lipoproteins are classified into five major classes: chylomicrons, very-low-density lipoproteins (VLDL), intermediate-density lipoproteins (IDL), low-density lipoproteins (LDL), and high-density lipoproteins (HDL) in Table 1.1 and Fig 1.1. HDL, colloquially known as "good cholesterol," participates in reverse cholesterol transport, while LDL, colloquially known as "bad cholesterol," promotes atherosclerosis.

Lipoprotein	**Density (g/ml)**	**Size (nm)**	**Major Lipids**	**Major Apoproteins**
Chylomicrons	< 0.930	75–1200	Triglycerides	Apo B-48, Apo C, Apo E, Apo A-I, A-II, A-IV
Chylomicron Remnants	0.930–1.006	30–80	Triglycerides, Cholesterol	Apo B-48, Apo E
VLDL	0.930–1.006	30–80	Triglycerides	Apo B-100, Apo E, Apo C
IDL	1.006–1.019	25–35	Triglycerides, Cholesterol	Apo B-100, Apo E, Apo C
LDL	1.019–1.063	18–25	Cholesterol	Apo B-100
HDL	1.063–1.210	5–12	Cholesterol, Phospholipids	Apo A-I, Apo A-II, Apo C, Apo E

Table 1.1: Major lipoprotein classes, density, size, major lipid composition, and associated apoproteins [2].

Disruptions in lipoprotein metabolism can have severe consequences for affected individuals. For instance, elevated LDL levels are a well-established risk factor for cardiovascular disease (CVD), as they promote premature atherosclerotic changes in blood vessels [5]. Lipoprotein disorders arise from a complex interplay of genetic predispositions and environmental influences. In Western populations, lifestyle factors in particular have been recognized as significant contributors to the development of these conditions.

Ongoing research, public health campaigns, and preventive strategies aim to mitigate the burden of lipoprotein-related disorders by promoting healthier lifestyle practices. Despite these efforts, the impact of CVD remains profound. According to the World Health Organization (WHO), cardiovascular diseases are the leading cause of death worldwide. In 2022 alone, an estimated 19.8 million people died from CVDs, representing approximately 32% of all global deaths. Of these, 85% were due to heart attacks and strokes[6, 7].

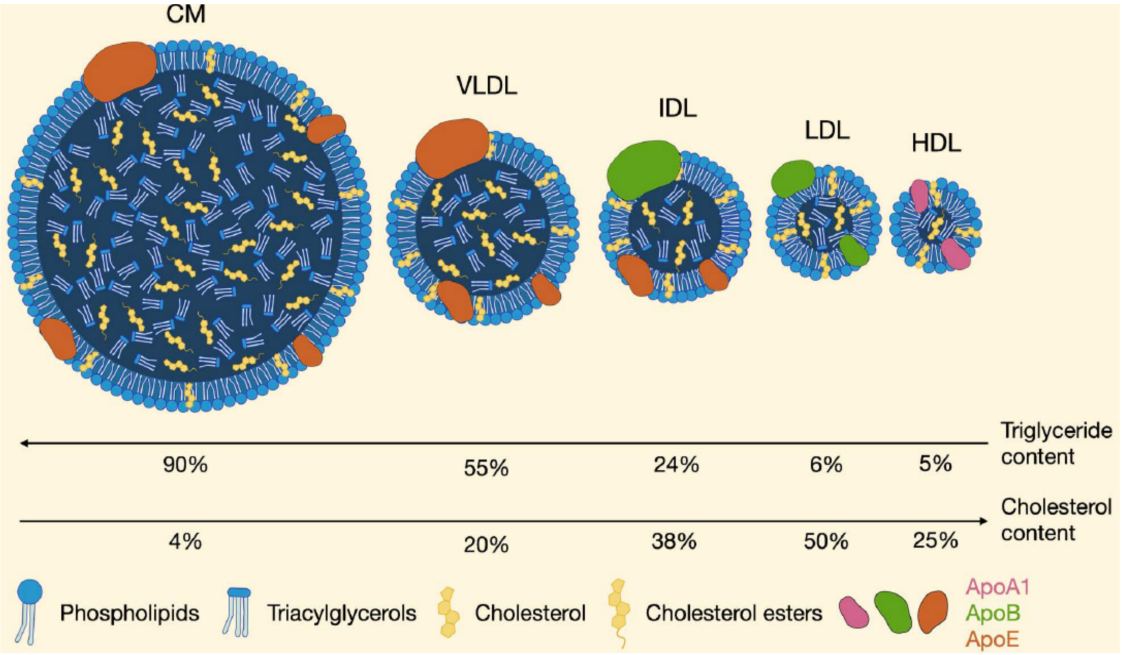

Figure 1.1: Lipoprotein particles comprise a hydrophobic core enriched in triacylglycerols and cholesteryl esters, surrounded by phospholipids and unesterified cholesterol that is stabilized by apolipoproteins. Variations in particle size and composition give rise to the classical categories: chylomicrons (CM), very-low-density (VLDL), intermediate-density (IDL), low-density (LDL), and high-density (HDL) lipoproteins. Representative apolipoproteins include apoA1, apoB, and apoE. Reported percentages refer to weight fractions. Figure adapted from [4].

1.2 HDL Metabolism and Cardiovascular Health

HDL are key players in plasma lipid metabolism and essential for cardiovascular health [8]. Their main job is reverse cholesterol transport (RCT) [9]: cholesterol and other cell lipids are moved out from peripheral tissues especially macrophages in the artery wall—back to the liver, where they can be dumped into bile and leave the body. This RCT pathway is a major reason why HDL shows anti-atherogenic effects. Beyond efflux, HDL particles also show antioxidant, anti-inflammatory, anti-thrombotic, and anti-apoptotic actions, which together help slow plaque formation and its progression [10]. Structurally, HDL are the smallest (≈10 nm diameter) and densest lipoproteins, built mostly from apolipoprotein A-I (apoA-I) about ≈70% of total HDL apoprotein plus phospholipids [11]. Other apolipoproteins also contribute to the composition of HDL particles [12]. ApoA-II is the second most abundant HDL apolipoprotein, accounting for approximately 15–20% of total HDL protein [13]. ApoC is the smallest apolipoprotein; it associates with both HDL and VLDL and readily exchanges between these lipoproteins. Although present at lower levels than apoA-I, ApoE is an important structural and functional glycoprotein component of HDL [14]. Because apoA-I is the principal protein that drives the formation of pre-β HDL (nascent HDL, nHDL) a key precursor in cholesterol metabolism and the central theme of this thesis, the discussion hereafter focuses specifically on Apolipoprotein A-I.

Mature human apoA-I has 243 amino acids and is encoded by exons 3 and 4 of its gene on chromosome 11. Exon 3 encodes residues 1–43, often called the "globular" N-terminal domain [15]; it starts with a short 10-residue segment termed G0, followed by three 11-mer repeats (G1, G2, G3). The classic lipid-binding motif in apoA-I is the amphipathic α-helix [16], largely encoded by exon 4 and frequently interrupted by proline residues. While most agree apoA-I is dominated by 11- and 22-mer helical segments, the exact 3D packing has been debated for years [17–22] because apoA-I occurs in several states including lipid-free, lipid-poor, and on discoidal or spheroidal HDL of different sizes and its conformation can shift between them [23]. Early concrete evidence for apoA-I's arrangement on discoidal HDL (dHDL) came from Borhani et al. [24], whose X-ray structure of residues 44–243 of lipid-free apoA-I suggested a "double-belt" organization. Axelsen et al [25]. Then, provided an experimental test of this belt concept using PATIR-FTIR, and theoretical work by Segrest et al [26] produced an atomic-resolution antiparallel double-belt amphipathic helical model for dHDL with an LL5/5 registry.

1.2.1 Reverse Cholestrol Transport

HDL occupies a central position in the RCT pathway [9], the process by which cholesterol is synthesized or deposited in peripheral tissues and returned to the liver for reuse or excretion in bile. Importantly, steady-state HDL concentrations reflect the balance between the rates of HDL particle production and catabolism;

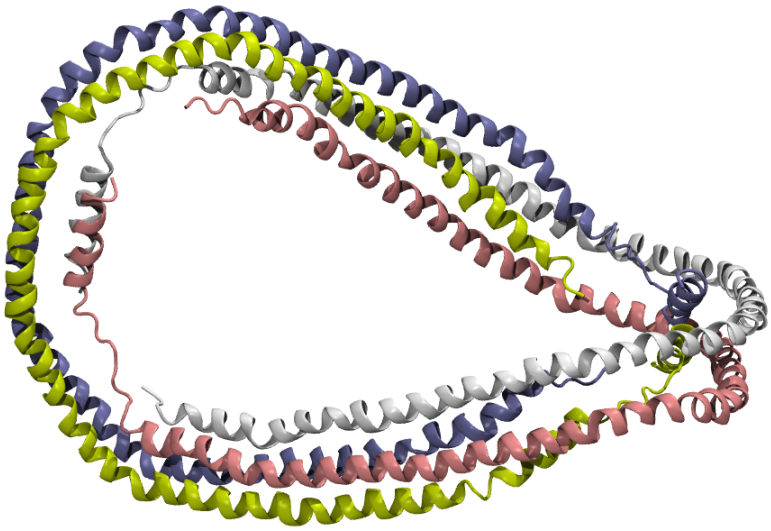

Figure 1.2: Pictorial representation of truncated human apolipoprotein A-I (apoA-I), the major protein component of high-density lipoprotein (HDL). apoA-I is composed almost entirely of a pseudo-continuous amphipathic α-helix, punctuated by kinks at regularly spaced proline residues. The structure comprises residues 44–243 (exon 4) of apoA-I and is taken from the Protein Data Bank (PDB ID: 1AV1).

consequently, while HDL levels are useful predictors of atherosclerotic risk, they function largely as biomarkers of the coordinated activity of multiple proteins that drive RCT rather than as isolated causal agents [8]. A minority of cells eliminate cholesterol directly through sebocytes and keratinocytes can secrete it onto the skin surface, and enterocytes can secrete it into the intestinal lumen, but most peripheral cells rely on RCT to prevent intracellular cholesterol accumulation.

The concept of RCT was first introduced in 1968 by Glomset [27]. RCT begins with the hepatic and intestinal synthesis of apoA-I, which acquires phospholipids and free cholesterol via interaction with the Adenosine triphosphate (ATP)-binding cassette transporter ABCA1 to form discoidal, lipid-poor "nascent" or pre-β-HDL. In parallel, tissue macrophages ingest excess cholesterol from their surroundings; when overloaded, these cholesterol-laden macrophages (foam cells) generate oxysterols that activate liver X receptors (LXR), thereby upregulating ABCA1 and ABCG1 to promote efflux of cholesterol to pre-β-HDL (via ABCA1) and to more mature HDL particles (via ABCG1). The free cholesterol transferred to nascent HDL is esterified by lecithin–cholesterol acyltransferase (LCAT), an apoA-I–activated enzyme, producing hydrophobic cholesteryl esters that migrate into the particle core and drive a morphological transition from discoidal pre-β-HDL to small, spherical HDL3; continued LCAT activity and lipid acquisition enlarge HDL3 to HDL2. These esterification and remodeling steps both expand HDL's cargo capacity and minimize back-diffusion of unesterified cholesterol. Ultimately, HDL delivers cholesteryl esters to the liver by two complementary routes: (i) direct selective uptake via the scavenger receptor class B type I (SR-BI) on hepatocytes, and (ii) indirect trans-

fer of cholesteryl esters to apoB-containing lipoproteins (VLDL/LDL) mediated by cholesteryl ester transfer protein (CETP), followed by hepatic uptake of those particles through LDL receptors. Within hepatocytes, cholesteryl esters are hydrolyzed to free cholesterol, which is either secreted into bile via ABCG5/ABCG8 transporters or converted to bile acids for excretion; hepatic lipase and phospholipid transfer protein (PLTP) remodel circulating HDL, interconverting HDL2 and HDL3, and regenerate smaller HDL particles that sustain efflux capacity. In addition to the uptake of cholesterol and cholesteryl esters by hepatocytes mediated by SR-B1 and LDLR, HDL can also be catabolized in the liver by being taken up as holoparticles via an unidentified HDL receptor (HDLR). Crucially, the liver continually releases new, lipid-poor apoA-I (often with phospholipids), which immediately re-engages ABCA1 on hepatic and peripheral cells to re-form pre-β-HDL—thereby restarting the RCT cycle and maintaining cholesterol homeostasis.

1.3 Challenges in HDL Raising Therapies for CVDs

Since the mid-20th century, high-density lipoprotein cholesterol (HDL-C) has been an attractive therapeutic target for atherosclerotic cardiovascular disease. The Framingham Heart Study first highlighted this relationship in 1977 [29], reporting that low HDL-C was a major risk factor for coronary artery disease (CAD). Subsequent re-analyses showed that low HDL-C was also associated with increased mortality [30]. Angiographic studies extended these observations: Jenkins and colleagues found that lower HDL-C correlated with greater atherosclerotic burden on coronary angiography [31]. Consistent with these data, Gordon et al. [32] estimated that each 1 mg/dL increase in HDL-C was associated with approximately a 2–3% reduction in CAD risk.

These findings spurred decades of epidemiological research and multiple clinical trials aimed at raising HDL-C to reduce CVD events. However, despite effectively elevating HDL-C, most pharmacologic interventions have not translated into meaningful reductions in cardiovascular outcomes. Recent systematic reviews [10, 28, 33, 34] and meta-analyses conclude that pharmacologically increasing HDL-C does not reliably lower cardiovascular event rates.

Before the widespread adoption of statins, niacin was one of the earliest agents used to raise HDL-C. In that era, niacin lowered total cholesterol, reduced non-fatal myocardial infarction, and was associated with a post-trial reduction in all-cause mortality. Yet two modern trials that added niacin to intensive statin therapy, AIM-HIGH and HPS2-THRIVE, failed to demonstrate a reduction in CVD events despite robust increases in HDL-C [35–37]. Fibrates induce the expression of apoA-I and apoA-II and thereby raise HDL-C. Meta-analyses suggest potential benefit in specific subgroups (e.g., patients with atherogenic dyslipidemia characterized by high triglycerides and low HDL-C). Nevertheless, the large PROMINENT trial (pemafibrate) provided strong evidence against routine fibrate use for CVD risk reduction,

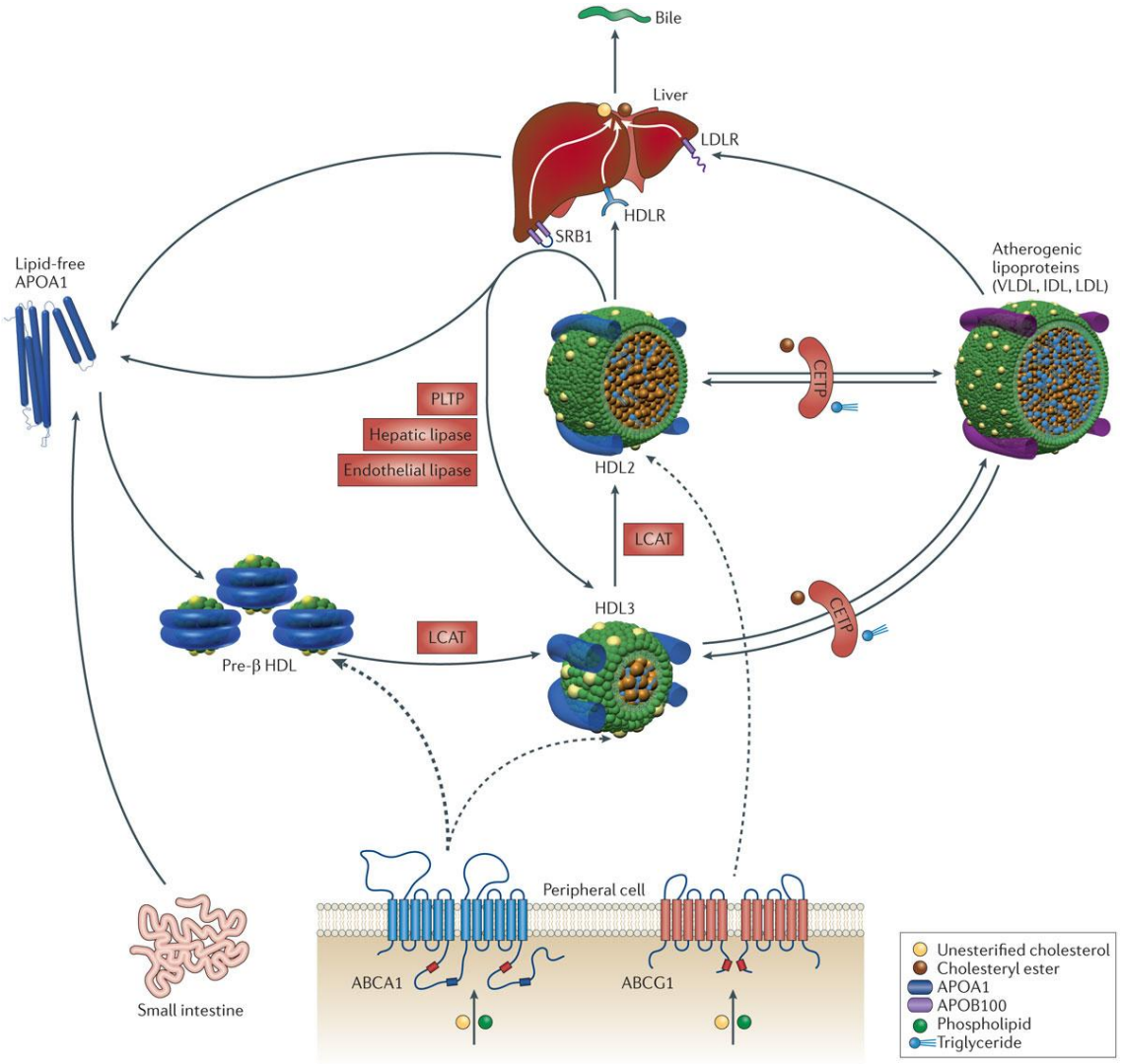

Figure 1.3: Schematic representation of Reverse Cholesterol Transport (RCT) and lipid metabolism. This figure is adapted from [28].

showing no benefit on cardiovascular outcomes despite favorable lipid changes [38].

CETP inhibitors inspired by genetic CETP deficiency are novel agents that have gained attention due to significant data demonstrating that CETP deficiency is linked to elevated HDL-C, and that regulation is favorable for lipoprotein levels in blood serum, associated with a reduction in CVD risk. However, clinical translation has been challenging. Torcetrapib is the first CETP inhibitor studied in humans. Trial ILLUMINATE was terminated early due to increased cardiovascular events in patients, resulting in mortality. Subsequent analysis revealed that Torcetrapib increased aldosterone and systolic blood pressure, which may have contributed to increased mortality [39, 40]. Dalcetrapib is another CETP inhibitor [41]; in the dal-OUTCOMES trial of patients with acute coronary syndrome, it increased HDL-C by up to 30% but did not reduce cardiovascular events. The ACCELERATE trial was terminated prematurely due to the futility of evacetrapib [42], which significantly increases the HDL-C by 125% and decreases LDL-C by 30%, but does not yield a reduction in CVD events. Similarly, there are many CETP-inhibiting agents that yield the same results, namely, anacetrapib [43].

Taken together, epidemiologic data and multiple clinical trials aiming at raising HDL-C with diverse drug strategies have yielded inconclusive results [10, 28, 34]. Even when HDL-C increased, cardio-protective effects were not consistently observed. As a result, the focus has shifted from HDL-C levels to HDL structure and its function.

1.4 Apolipoprotein A-I Mimetic Peptides (AAM) and synthetic-High Density Lipoproteins (sHDL): Therapeutic to CVD

Apolipoprotein A-I is central to HDL metabolism: it activates LCAT, promotes HDL particle maturation, and facilitates reverse cholesterol transport. However, because apoA-I is produced by the liver and intestine and has a relatively short half-life in plasma and other body fluids, its practicality as a therapeutic, considering cost, manufacturability, and route of administration, is limited. These constraints motivated the development of smaller peptides that mimic key apoA-I functions, giving rise to the field of apoA-I mimetics [44].

apoA-I mimetic peptides are small amphipathic α-helical peptides that recapitulate essential structural and functional features of apoA-I. In some contexts, these mimetics exhibit anti-inflammatory activity that is equal to or superior to that of the full-length protein. The first prototype, 18A (DWLKAFYDKVAEKLKEAF), was designed by Anantharamaiah in collaboration with Segrest [45]. It is a non-homologous class A amphipathic helix with clearly segregated hydrophobic and hydrophilic faces, inspired by apoA-I architecture. The original 18A contains two

phenylalanine residues on the hydrophobic face and is therefore sometimes called 2F. In vitro, 18A associates with non-oxidized lipids and supports LCAT activation and cholesterol efflux [44].

To increase helicity and stabilize the α-helical conformation hypothesized to enhance lipid binding end capping was introduced (N-terminal acetylation and C-terminal amidation; Ac-18A-NH_2) [46]. These modifications increased lipid affinity and stabilized secondary structure in vitro. Despite binding non-oxidized lipids, Ac-18A-NH_2 was not effective in mouse models of atherosclerosis. A bihelical variant was then created by linking two 18A units with a proline (18A-P-18A). This tandem peptide promoted cholesterol efflux from macrophages in culture and showed increased lipid association. In vitro, lipid association followed the trend: bihelical Ac-18A-NH_2 > Ac-18A-NH_2 > 18A [47].

Structure–activity insights guided the next step in tuning of hydrophobicity by adding phenylalanine residues [48]. The 4F peptide (Ac-DWFKAFYDKVAEKLKEAF-NH_2) exhibited greater lipid association and cholesterol efflux—including with oxidized lipids and showed improved in vivo performance relative to 18A. Additional apo-A1 mimetic peptide series (5F: Ac-DWLKAFYDKVFFKFKEFF-NH_2, 6F: Ac-DWLKAFYDKFFEKFKEFF-NH_2, 7F: Ac-DWFKAFYDKFFEKFKEFF-NH_2) were synthesized to probe the relation between the increase in hydrophobicity and lipid-association. Phenylalanine was favored because it is an acid-resistant hydrophobic residue common in membrane-active peptides and is synthetically more tractable than tryptophan. Increasing hydrophobicity from 4F to 5F enhanced phospholipid association; 6F and 7F were less effective, indicating an upper limit beyond which added hydrophobicity becomes detrimental. In vitro, 4F, 5F, and 6F were comparably potent at inhibiting LDL-induced monocyte chemotaxis. Collectively, these studies suggest that an appropriate balance between peptide–peptide and peptide–lipid interactions is required for optimal activity of amphipathic helices[48].

Over subsequent years, Navab et al. [49] conducted in vivo studies on a series of apoA-I mimetic peptides derived from the 18A motif. They showed that the ability to activate LCAT in vitro did not predict biological activity in vivo. However, analysis of the peptides' physicochemical properties suggested a plausible mechanism of action for those that were biologically active. In particular, the 4F and 5F peptides were active in arterial wall cell culture systems and mitigated lesion development. To increase stability and reduce proteolysis in vivo, 4F was often synthesized from D-amino acids (D-4F). Orally administered D-4F peptides increased paraoxonase activity and promoted the formation of pre-β HDL/nHDL-like particles in non-human primates [49, 50], and it was licensed by Novartis and advanced to phase I clinical trials in 2008. 4F peptides can assemble into nHDL-like particles and interact with SR-BI, highlighting their therapeutic potential in atherosclerosis. A bihelical "tandem" form 4F-P-4F (Ac-DWFKAFYDKVAEKLKEAF-P-DWFKAFYDKVAEKLKEAF-NH_2) more closely mimicked apoA-I in HDL remodeling and cholesterol efflux in vitro and showed stronger lipid association than monomeric 4F [51]. Beyond their cardioprotective effects, apoA-I mimetic peptides have been reported to alleviate

lung pathology in animal models of pulmonary inflammation [52–55].

Lipidation has been proposed as a strategy to address key limitations of apoA-I mimetic peptides, namely their tendency to aggregate and their susceptibility to proteolytic degradation, thereby improving pharmacokinetic behavior and therapeutic utility [55, 56]. When apoA-I mimetic peptides are formulated with phospholipids at defined stoichiometries, they self-assemble into uniform, discoidal synthetic HDL (sHDL) nanodiscs that display enhanced stability and extended circulating half-life relative to the free peptide [55, 57]. By constraining the amphipathic helices with lipids, as sHDL reduces nonspecific aggregation of peptides and yields more predictable behavior in biological environments [55].

With optimized structures and consistent composition [55, 58], sHDL mimetics tend to be more effective therapeutically than native HDL. Beyond therapeutics, the nanodisc architecture is well-suited for advanced biomedical applications: for example, 4F-based sHDL has been integrated with phospholipid cores and quantum dots to create optically traceable HDL mimetics for imaging applications [59].

Despite extensive in vitro and in vivo studies of s-HDL systems highlighting the broad potential of peptide-based nanodiscs [60, 61], their fundamental physicochemical attributes, such as molecular organization, size, structure, and dynamics, and the relationships between these attributes and biological effects, remain largely unexplored. To address this gap, we selected clinically relevant apoA-I mimetic peptides 4F, 4F-P-4F, and 14A (Fig. 1.4) for detailed evaluation.

1.4.1 AAM Nanodiscs: A tool for membrane protein characterization

Nanodiscs serve as powerful, detergent-free platforms for the biophysical characterization of membrane proteins (MPs) [62–65]. Because MPs play structural and functional roles central to life processes, they are of immense biomedical interest [8, 66, 67]: roughly one-third of all human proteins are membrane proteins, and approximately 50% of all approved drugs target them [68–70]. Handling MPs is notoriously challenging, as they often lose activity or display altered function outside a phospholipid environment. Consequently, determining MP structure is essential to understanding their molecular mechanisms, and the structural biology of MPs has remained a central topic in biophysics, biochemistry, and cell biology for decades.

Membrane proteins are often isolated and stabilized with detergents or other hydrophobic agents that shield their transmembrane domains. However, these environments do not guarantee proper function and can even denature MPs [71]. In biophysical studies, MPs are sometimes solubilized into proteoliposomes for expression in cell-free systems, but these preparations often yield turbid, viscous solutions. A more native-like and tractable alternative is to reconstitute MPs in nanodiscs for characterization. Together with electron microscopy [72, 73], numerous studies

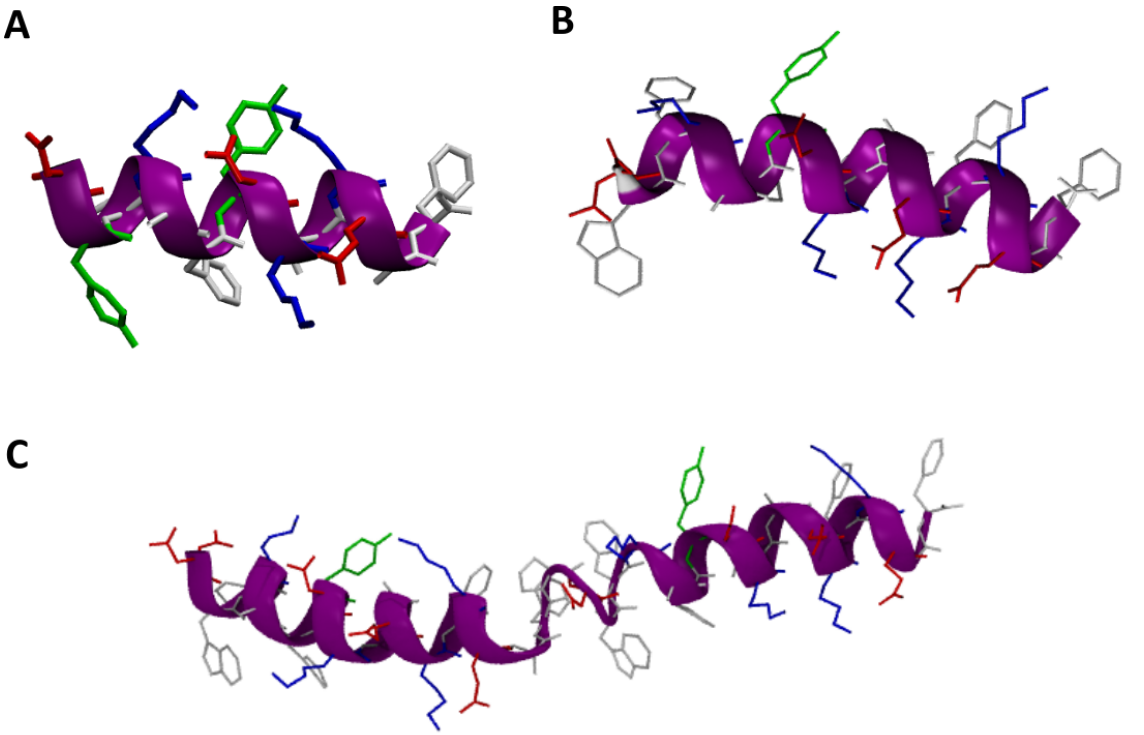

Figure 1.4: Schematic representation of the ApoA–I mimetic peptides studied in this thesis: (A) 14A, (B) 4F, and (C) 4F-P-4F.

now employ nanodiscs with varied scaffold architectures, reflecting growing interest in this technology. A notable example is the reconstruction of the full-length, active-state insulin receptor in nanodiscs [74].

Conventional nanodiscs use membrane scaffold proteins (MSPs)—often based on apolipoprotein A-I that are covalently linked via glycine or proline residues to form discs with fixed diameters, typically 10–17 nm. By contrast, engineered apoA-I-mimetic amphipathic peptides assemble nanodiscs through noncovalent interactions, enabling size tuning by adjusting the peptide-to-lipid ratio [75]. These peptides mimic MSP function and stabilize discoidal lipid patches. There are other scaffold architectures for nanodiscs, such as polymer nanodiscs [76], saposin nanodiscs [77], and DNA-scaffolded nanodiscs [78], but they are not of particular interest in this thesis.

Recent experimental studies [79], supported by molecular dynamics simulations, have demonstrated that the size of lipid nanodiscs significantly influences the structure of pentameric ligand-gated ion channels (pLGICs). Specifically, reconstitution of the Erwinia ligand-gated ion channel (ELIC) into MSP-based nanodiscs of differing diameters (10–17nm) leads to distinct structural conformations, as observed by single-particle cryo-electron microscopy (cryo-EM). Moreover, investigations using MSP2N2 nanodiscs (17nm), the largest among MSP constructs, revealed that scaffold–protein interactions can perturb channel function: $\alpha 1\beta 3$ $GABA_AR$ receptors maintained a closed activation gate despite exhibiting a peak open probability

of approximately≈0.6 in HEK293 cells [80, 81], lipid tail packing [82] and size of the nanodisc can modulate membrane protein activity. Similarly, a recent study reports that ABC transporter activity is affected by nanodisc size [83]. In that work, the smallest MSP1D1 nanodiscs (10 nm) altered the basal activity of human ABCB10 (an inner mitochondrial membrane transporter of biliverdin), AtAtm3 (a half-transporter of the ABCB family in plants), and the bacterial LmrA multidrug resistance transporter, and also changed their responses to substrates. By contrast, in larger MSP2N2 nanodiscs, these transporters showed strong substrate-induced stimulation, similar to that observed in liposomes. The authors speculate that these effects arise either from direct interactions between the transporter and the nanodisc scaffold or from lipid properties within the nanodisc. Comparable size-dependent effects have been observed for the G-protein-coupled receptor rhodopsin: in smaller discs (SMALP and SMILP, both ≈10 nm in diameter), photo-conversion to the fully active receptor is restricted relative to what is achieved in larger discs [84].

Interestingly, peptide-based nanodiscs ("macrodiscs") offer tunable sizes up to ≈30 nm and may be less prone to scaffold interference [85]. Notably, macrodiscs formed by the 14A peptide (Ac-DYLKAFYDKLKEAF-NH_2), derived from the 18A peptide by removing one helical turn, align with the magnetic field and can serve as alignment media for measuring residual dipolar couplings (RDCs) of membrane proteins without detergents [85]. Peptide-based nanodiscs also have limitations relative to MSP-based discs: they are typically less homogeneous, and controlling polydispersity can be challenging, though not prohibitive. On the other hand, these amphipathic peptides can solubilize membranes and thus replace detergents as an intermediate platform to extract MPs for subsequent incorporation into MSP nanodiscs[86].

These studies underscore the importance of scaffold design and motivate the development of size-tunable nanodiscs to test the long-standing hypothesis that larger nanodiscs yield more homogeneous lipid properties. The scaffold is crucial for stabilizing the nanodisc architecture. However, there is evidence that MSPs can alter lipid tail and headgroup conformations and modify lipid dynamics; as a result, lipid structural properties in nanodiscs can differ from those in planar bilayers. Because in such cases, like mechanosensitive membrane proteins respond to membrane tension and lipid-mediated allosteric interactions[87, 88], the local lipid environment around MPs is critical [89]. It is therefore essential to characterize both structure and lipid dynamics within nanodiscs, and to determine whether nanodisc size is related to lipid properties.

In this presented thesis, to address these gaps, we focus primarily on peptide-based nanodiscs to elucidate their structural details using MD simulations. In particular, for the 14A peptide-based nanodisc, we identify key interactions that stabilize this peptide-lipid assembly using all-atom molecular dynamics simulations, and we back-calculate NMR observables, namely ^{2}H quadrupolar splittings and ^{15}-N chemical shifts, to compare with solid-state NMR measurements and infer the local orientations of peptides around the discoidal bilayer. In addition, we quantify how different-sized nanodiscs modulate lipid properties and compare these with those of planar lipid bilayers.

1.5 Studying Nanodisc Assembly and Structure

Understanding how the physico-chemical properties of nascent high-density lipoprotein particles, such as structure, size, morphology, molecular organization, and dynamics, relate to biological function requires a combination of experimental and computational approaches. Complementary biophysical techniques include ultracentrifugation, size-exclusion chromatography (SEC), native polyacrylamide gel electrophoresis (native PAGE), dynamic light scattering (DLS), transmission electron microscopy (TEM), cryo-TEM, X-ray and neutron scattering, and NMR spectroscopy. Alongside these experiments, molecular modeling and MD simulations provide atomistic insights into structure and dynamics that are otherwise difficult to obtain for such complex assemblies. Detailed structural knowledge of nanodiscs is crucial for elucidating HDL functions, designing more effective mimetic peptides, and accurately characterizing membrane proteins.

The first all-atom (AA) MD simulations of planar lipid bilayers were reported in 1994 [90], marking the beginning of membrane simulations. Within a few years, the first nanodisc simulations of nHDL were reported [91]. Those early studies aimed to determine the preferred local orientation of apoA-I around a discoidal lipid bilayer by comparing two "picket-fence" dimer configurations, head-to-tail and head-to-head. wing to limited computational power at the time, trajectories were shorter than a nanosecond, which was insufficient to unambiguously identify the dominant conformation. In subsequent years, the first all-atom MD study of an apoA-I mimetic peptide nanodisc (Ac-18A-NH_2) was reported[92]. A 700-ps simulation of a preassembled "picket-fence" arrangement of the peptide around the disc highlighted the importance of interhelical interactions. owever, later work showed that the picket-fence model for Ac-18A-NH_2 was not consistent with experimental data [93] as well as MD simulation [86].

Following the proposal of a "double-belt" conformation for apoA-I [24–26], A. E. Klon et al. [94] simulated three nHDL models with different apoA-I registries (≈1-ns replicates). Although the simulations did not converge to a single optimal registry, they revealed characteristic salt-bridge triads in which an acidic residue on one monomer bridged two basic residues on the other. Importantly, based on these data, they posited two factors that hinder sliding once optimal alignment is reached: (i) proline-induced kinks that should overlap to minimize hydrophobic penalties, forming a continuous helical wrap around the discoidal bilayer, and (ii) the presence of two 11-mer helices that interrupt the periodic 22-mer helical motif, thereby enforcing a preferred registry.

Shih et al. [95] simulated MSP-based nanodiscs in four double-belt configurations containing 160 1,2-dipalmitoylphosphatidylcholine (DPPC) lipids for 4–6 ns. They inferred that the first 17–18 residues of the ≈200-residue apoA-I lipid-binding domain are not involved in forming the protein "belts" that encircle the bilayer. They also simulated bacteriorhodopsin, a seven-helix integral membrane protein, embedded in an MSP-stabilized nanodisc for 4.5 ns, observing a planar disk with a slightly

rectangular shape. Attempts to compare simulation-derived SAXS curves with experimental data revealed discrepancies, highlighting the need for longer sampling and improved models.

The first coarse-grained (CG) simulations of nanodiscs by Shih et al. [96] confirmed that preassembled CG models preserve overall particle shape and key structural features of discoidal HDL. In self-assembly simulations, scaffold proteins aggregated with lipids over time; by ≈175 ns, both scaffold proteins had fully associated with the lipids. The proteins bound opposite sides of the bilayer and continued to rearrange through 1.5 µs, without approaching closely enough to interact directly. The MSPs appeared disordered yet loosely reminiscent of a picket-fence orientation. An improved CG model—partly [97] adopting bonded and non-bonded parameters from MARTINI [98] subsequently produced self-assembled nanodiscs that strongly favored the double-belt over the picket-fence arrangement.

Debnath et al. [99] investigated the self-assembly and physical properties of nanodiscs composed of 160 phospholipids and a double-belt MSP using two 42-µs CG simulations and a 50-ns AA simulation. All lipids were incorporated into the MSP-encircled region within ≈7.5 µs. In the AA trajectories, lipids near the nanodisc center were highly ordered, whereas annular lipids in contact with the proteins were disordered due to perturbed packing relative to an infinite lamellar bilayer. Nanodisc lipids exhibited lower configurational entropy and higher acyl-chain order—consistent with SANS and fluorescence measurements on DMPC/apoA-I nanodiscs [100].

Interest in apoA-I mimetic peptides has grown due to their biomedical potential and as alternative platforms for membrane-protein studies (see sections 1.4 and 1.4.1). CG simulations with an implicit solvent model probed the self-assembly and structure of 18A-peptide nanodiscs; Small peptide–lipid assemblies formed rapidly and fused into larger assemblies of varying size; some peptides also self-associated. These findings informed the SEC–SAXS data analysis [86].

In follow-up work, the self-assembly of DMPC nanodiscs stabilized by three dimeric 18A peptides was examined using three 2-microsecond (scaled time) CG simulations with implicit water [101]. The 18A dimers were either directly connected (no linker) or linked by Pro or Gly-Gly. Smaller particles collided to form larger nanodiscs, with final sizes consistent with small-angle scattering models. The number of lipids in the largest particles converged after ≈1.1 ms, indicating that full-sized peptide nanodiscs form on millisecond timescales. Total simulation energies correlated with stability measured by static light scattering (SLS): Pro-linked dimers yielded the least stable discs and the highest energies, whereas the no-linker dimers produced the most stable discs and the lowest energies. Although 18A-peptide nanodiscs had total energies similar to those of the Pro-linked systems, SLS showed that 18A-peptide nanodiscs were substantially more stable. This discrepancy underscores the limitations of the implicit-solvent CG simulations.

Extensive in vitro studies by the Anantharamaiah group provided valuable structural

information on apo A-I mimetic peptide lipid assemblies [93, 102, 103]. Importantly, Peptide–lipid assemblies of AC-18-NH_2 and 4F nuclear overhauser effects (NOEs) measurements indicated that the amphipathic helix lies parallel to the bilayer plane at the nanodisc rim. Further NMR data suggest that a head-to-tail anti-parallel arrangement of helices that cover the discoidal bilayer[93, 102].

Islam et al.[104] investigated nanodiscs stabilized by four ELK peptides—one cationic (pos), one anionic (neg), and two neutral that differed in hydrophobicity (hyd, neu) using all-atom molecular dynamics simulations, and compared the simulation outcomes with experimentally measured cholesterol-efflux activities. All peptides initially adopted antiparallel 'picket-fence' arrangements at the rim of the discoidal lipid bilayer. The hyd and neu variants remained at the rim, stabilized by favorable salt-bridge interactions, whereas the pos and neg variants experienced mutual repulsion and migrated onto the disc surface. These behaviors correlated with peptides' cholesterol efflux abilities by quantifying the lipid-peptide interactions. Overall, the study concluded that ELK-peptide nanodiscs favor an antiparallel 'picket-fence' organization (Fig.8 in [104]).

Across decades, nHDL and sHDL particles have been interrogated with diverse experimental techniques and complemented by MD simulations that elucidate formation mechanisms and the interactions governing nanodisc stability [105]. The underlying structural models continue to evolve, and in some cases, the integration of MD with experiment has yielded mechanistic insights into cholesterol efflux [104].

Established MD methodologies [105] and reported in-vitro structural data for MSP nanodiscs and apoA-I mimetic peptide nanodiscs provide a robust foundation for modeling and characterizing the 4F, 4F-P4F, and 14A systems. A persistent open question is how amphipathic helices arrange at the rim of discoidal nanodiscs. Simulations of ELK-type helices often favor an anti-parallel "picket-fence" topology[104], whereas NMR data for 4F, Ac-18A-NH_2, and 14A support an anti-parallel "double-belt" architecture[93, 102, 106]. At least in the case of peptide-lipid nanodiscs, the definitive model has not yet emerged: the rationale for helix orientation and registry, and the relative contributions of peptide–peptide and peptide–lipid interactions to rim stabilization, remain unresolved.

References

[1] Kenneth R Feingold. Lipid and lipoprotein metabolism. *Endocrinology and Metabolism Clinics*, 51(3):437–458, 2022.

[2] Shlomo Eisenberg and Robert I Levy. Lipoprotein metabolism. *Advances in lipid research*, 13:1–89, 1975.

[3] Louis C Smith, Henry J Pownall, and Antonio M Gotto Jr. The plasma lipoproteins: structure and metabolism. *Annual Review of Biochemistry*, 47 (1):751–777, 1978.

[4] Carlos Pérez-Medina, Edward A Fisher, Zahi A Fayad, Willem JM Mulder, and Abraham JP Teunissen. Radiolabeling lipoproteins to study and manage disease. *European Journal of Nuclear Medicine and Molecular Imaging*, pages 1–18, 2025.

[5] Børge G Nordestgaard and Anne Langsted. Lipoprotein (a) as a cause of cardiovascular disease: insights from epidemiology, genetics, and biology. *Journal of lipid research*, 57(11):1953–1975, 2016.

[6] World Health Organization. Cardiovascular diseases (cvds) fact sheet. https://www.who.int/news-room/fact-sheets/detail/cardiovascular-diseases-%28cvds%29, 2025. Accessed: 2025-09-18.

[7] George A Mensah, Valentin Fuster, and Gregory A Roth. A heart-healthy and stroke-free world: using data to inform global action, 2023.

[8] Daniel J Rader and G Kees Hovingh. Hdl and cardiovascular disease. *The Lancet*, 384(9943):618–625, 2014.

[9] Daniel J Rader, Eric T Alexander, Ginny L Weibel, Jeffrey Billheimer, and George H Rothblat. The role of reverse cholesterol transport in animals and humans and relationship to atherosclerosis. *Journal of lipid research*, 50:S189–S194, 2009.

[10] Mohammad Al Zein, Alicia Khazzeka, Alessandro El Khoury, Jana Al Zein, Dima Zoghaib, and Ali H Eid. Revisiting high-density lipoprotein cholesterol in cardiovascular disease: Is too much of a good thing always a good thing? *Progress in Cardiovascular Diseases*, 87:50–59, 2024.

[11] Ernst J Schaefer, Raul D Santos, and Bela F Asztalos. Marked hdl deficiency and premature coronary heart disease. *Current opinion in lipidology*, 21(4): 289–297, 2010.

[12] Arnold von Eckardstein and Dimitris Kardassis. *High density lipoproteins: from biological understanding to clinical exploitation*. Springer Nature, 2015.

[13] P Duriez and JC Fruchart. High-density lipoprotein subclasses and apolipoprotein ai. *Clinica chimica acta*, 286(1-2):97–114, 1999.

[14] Gerd Utermann. Isolation and partial characterization of an arginine-rich apolipoprotein from human plasma very-low-density lipoproteins: apolipoprotein e. 1975.

[15] Jere P Segrest, Martin K Jones, Hans De Loof, Christie G Brouillette, YV Venkatachalapathi, and GM Anantharamaiah. The amphipathic helix in the exchangeable apolipoproteins: a review of secondary structure and function. *Journal of lipid research*, 33(2):141–166, 1992.

[16] Jere P Segrest, David W Garber, Christie G Brouillette, Stephen C Harvey, and GM Anantharamaiah. The amphipathic α helix: a multifunctional structural motif in plasma apolipoproteins. *Advances in protein chemistry*, 45: 303–369, 1994.

[17] Hui-hua Li, Douglas S Lyles, Wei Pan, Eric Alexander, Michael J Thomas, and Mary G Sorci-Thomas. Apoa-i structure on discs and spheres: variable helix registry and conformational states. *Journal of Biological Chemistry*, 277 (42):39093–39101, 2002.

[18] Shaila Bhat, Mary G Sorci-Thomas, Rubina Tuladhar, Michael P Samuel, and Michael J Thomas. Conformational adaptation of apolipoprotein ai to discretely sized phospholipid complexes. *Biochemistry*, 46(26):7811–7821, 2007.

[19] RA Gangani D Silva, Rong Huang, Jamie Morris, Jianwen Fang, Elena O Gracheva, Gang Ren, Anatol Kontush, W Gray Jerome, Kerry-Anne Rye, and W Sean Davidson. Structure of apolipoprotein ai in spherical high density lipoproteins of different sizes. *Proceedings of the National Academy of Sciences*, 105(34):12176–12181, 2008.

[20] Feifei Gu, Martin K Jones, Jianguo Chen, James C Patterson, Andrea Catte, W Gray Jerome, Ling Li, and Jere P Segrest. Structures of discoidal high density lipoproteins: A combined computational-experimental approach 2. *Journal of Biological Chemistry*, 285(7):4652–4665, 2010.

[21] Rong Huang, RA Gangani D Silva, W Gray Jerome, Anatol Kontush, M John Chapman, Linda K Curtiss, Timothy J Hodges, and W Sean Davidson. Apolipoprotein ai structural organization in high-density lipoproteins isolated from human plasma. *Nature structural & molecular biology*, 18(4):416–422, 2011.

[22] Jere P Segrest, Martin K Jones, and Andrea Catte. Md simulations suggest important surface differences between reconstituted and circulating spherical hdl1 [s]. *Journal of Lipid Research*, 54(10):2718–2732, 2013.

[23] Patrick Linsel-Nitschke and Alan R Tall. Hdl as a target in the treatment of atherosclerotic cardiovascular disease. *Nature reviews Drug discovery*, 4(3): 193–205, 2005.

[24] David W Borhani, Danise P Rogers, Jeffrey A Engler, and Christie G Brouillette. Crystal structure of truncated human apolipoprotein ai suggests a lipid-bound conformation. *Proceedings of the National Academy of Sciences*, 94 (23):12291–12296, 1997.

[25] Vishwanath Koppaka, Loraine Silvestro, Jeffrey A Engler, Christie G Brouillette, and Paul H Axelsen. The structure of human lipoprotein ai: evidence for the "belt" model. *Journal of Biological Chemistry*, 274(21):14541–14544, 1999.

[26] Jere P Segrest, Martin K Jones, Anthony E Klon, Christopher J Sheldahl, Matthew Hellinger, Hans De Loof, and Stephen C Harvey. A detailed molecular belt model for apolipoprotein ai in discoidal high density lipoprotein. *Journal of Biological Chemistry*, 274(45):31755–31758, 1999.

[27] John A Glomset. The plasma lecithin: cholesterol acyltransferase reaction. *Journal of lipid research*, 9(2):155–167, 1968.

[28] Bronwyn A Kingwell, M John Chapman, Anatol Kontush, and Norman E Miller. Hdl-targeted therapies: progress, failures and future. *Nature reviews Drug discovery*, 13(6):445–464, 2014.

[29] Tavia Gordon, William P Castelli, Marthana C Hjortland, William B Kannel, and Thomas R Dawber. High density lipoprotein as a protective factor against coronary heart disease: the framingham study. *The American journal of medicine*, 62(5):707–714, 1977.

[30] PW Wilson, Robert D Abbott, and William P Castelli. High density lipoprotein cholesterol and mortality. the framingham heart study. *Arteriosclerosis: An Official Journal of the American Heart Association, Inc.*, 8(6):737–741, 1988.

[31] PJ Jenkins, RW Harper, and PJ Nestel. Severity of coronary atherosclerosis related to lipoprotein concentration. *Br Med J*, 2(6134):388–391, 1978.

[32] David J Gordon, Jeffrey L Probstfield, Robert J Garrison, James D Neaton, William P Castelli, James D Knoke, David R Jacobs Jr, Shrikant Bangdiwala, and H Alfred Tyroler. High-density lipoprotein cholesterol and cardiovascular disease. four prospective american studies. *Circulation*, 79(1):8–15, 1989.

[33] Haris Riaz, Safi U Khan, Hammad Rahman, Nishant P Shah, Edo Kaluski, A Michael Lincoff, and Steven E Nissen. Effects of high-density lipoprotein

targeting treatments on cardiovascular outcomes: a systematic review and meta-analysis. *European journal of preventive cardiology*, 26(5):533–543, 2019.

[34] K Mahdy Ali, A Wonnerth, K Huber, and J Wojta. Cardiovascular disease risk reduction by raising hdl cholesterol–current therapies and future opportunities. *British journal of pharmacology*, 167(6):1177–1194, 2012.

[35] Paul L Canner, Kenneth G Berge, Nanette K Wenger, Jeremiah Stamler, Lawrence Friedman, Ronald J Prineas, William Friedewald, Coronary Drug Project Research Group, et al. Fifteen year mortality in coronary drug project patients: long-term benefit with niacin. *Journal of the American College of Cardiology*, 8(6):1245–1255, 1986.

[36] HPS2-Thrive Collaborative Group. Effects of extended-release niacin with laropiprant in high-risk patients. *New England Journal of Medicine*, 371(3): 203–212, 2014.

[37] LeAnne T Bloedon, Richard Dunbar, Danielle Duffy, Paula Pinell-Salles, Robert Norris, Bruce J DeGroot, Rajesh Movva, Mohamad Navab, Alan M Fogelman, and Daniel J Rader. Safety, pharmacokinetics, and pharmacodynamics of oral apoa-i mimetic peptide d-4f in high-risk cardiovascular patients. *Journal of lipid research*, 49(6):1344–1352, 2008.

[38] Aruna D Pradhan, Nina P Paynter, Brendan M Everett, Robert J Glynn, Pierre Amarenco, Marshall Elam, Henry Ginsberg, William R Hiatt, Shun Ishibashi, Wolfgang Koenig, et al. Rationale and design of the pemafibrate to reduce cardiovascular outcomes by reducing triglycerides in patients with diabetes (prominent) study. *American heart journal*, 206:80–93, 2018.

[39] Philip J Barter, Mark Caulfield, Mats Eriksson, Scott M Grundy, John JP Kastelein, Michel Komajda, Jose Lopez-Sendon, Lori Mosca, Jean-Claude Tardif, David D Waters, et al. Effects of torcetrapib in patients at high risk for coronary events. *New England journal of medicine*, 357(21):2109–2122, 2007.

[40] Steven E Nissen, Jean-Claude Tardif, Stephen J Nicholls, James H Revkin, Charles L Shear, William T Duggan, Witold Ruzyllo, William B Bachinsky, Gabriel P Lasala, and E Murat Tuzcu. Effect of torcetrapib on the progression of coronary atherosclerosis. *New England journal of medicine*, 356(13):1304–1316, 2007.

[41] Gregory G Schwartz, Anders G Olsson, Markus Abt, Christie M Ballantyne, Philip J Barter, Jochen Brumm, Bernard R Chaitman, Ingar M Holme, David Kallend, Lawrence A Leiter, et al. Effects of dalcetrapib in patients with a recent acute coronary syndrome. *New England Journal of Medicine*, 367(22): 2089–2099, 2012.

[42] A Michael Lincoff, Stephen J Nicholls, Jeffrey S Riesmeyer, Philip J Barter, H Bryan Brewer, Keith AA Fox, C Michael Gibson, Christopher Granger, Venu Menon, Gilles Montalescot, et al. Evacetrapib and cardiovascular outcomes in

high-risk vascular disease. *New England Journal of Medicine*, 376(20):1933–1942, 2017.

[43] HPS3/TIMI55-Reveal Collaborative Group. Effects of anacetrapib in patients with atherosclerotic vascular disease. *New England Journal of Medicine*, 377 (13):1217–1227, 2017.

[44] GM Anantharamaiah. [36] synthetic peptide analogs of apolipoproteins. In *Methods in Enzymology*, volume 128, pages 627–647. Elsevier, 1986.

[45] GM Anantharamaiah, JL Jones, CG Brouillette, CF Schmidt, BYUNG HONG Chung, TA Hughes, AuS Bhown, and JP Segrest. Studies of synthetic peptide analogs of the amphipathic helix. structure of complexes with dimyristoyl phosphatidylcholine. *Journal of Biological Chemistry*, 260(18):10248–10255, 1985.

[46] YV Venkatachalapathi, Michael C Phillips, Richard M Epand, Raquel F Epand, Ewan M Tytler, Jere P Segrest, and GM Anantharamaiah. Effect of end group blockage on the properties of a class a amphipathic helical peptide. *Proteins: Structure, Function, and Bioinformatics*, 15(4):349–359, 1993.

[47] W Sean Davidson, Sissel Lund-Katz, William J Johnson, GM Anantharamaiah, Mayakonda N Palgunachari, Jere P Segrest, George H Rothblat, and Michael C Phillips. The influence of apolipoprotein structure on the efflux of cellular free cholesterol to high density lipoprotein. *Journal of Biological Chemistry*, 269(37):22975–22982, 1994.

[48] Geeta Datta, Manjula Chaddha, Susan Hama, Mohamad Navab, Alan M Fogelman, David W Garber, Vinod K Mishra, Richard M Epand, Raquel F Epand, Sissel Lund-Katz, et al. Effects of increasing hydrophobicity on the physical-chemical and biological properties of a class a amphipathic helical peptide. *Journal of lipid research*, 42(7):1096–1104, 2001.

[49] Mohamad Navab, GM Anantharamaiah, Srinivasa T Reddy, Susan Hama, Greg Hough, Victor R Grijalva, Nicholas Yu, Benjamin J Ansell, Geeta Datta, David W Garber, et al. Apolipoprotein ai mimetic peptides. *Arteriosclerosis, thrombosis, and vascular biology*, 25(7):1325–1331, 2005.

[50] Mohamad Navab, GM Anantharamaiah, Susan Hama, Greg Hough, Srinivasa T Reddy, Joy S Frank, David W Garber, Shaila Handattu, and Alan M Fogelman. D-4f and statins synergize to render hdl antiinflammatory in mice and monkeys and cause lesion regression in old apolipoprotein e–null mice. *Arteriosclerosis, thrombosis, and vascular biology*, 25(7):1426–1432, 2005.

[51] Geoffrey D Wool, Catherine A Reardon, and Godfrey S Getz. Apolipoprotein ai mimetic peptide helix number and helix linker influence potentially antiatherogenic properties. *Journal of lipid research*, 49(6):1268–1283, 2008.

[52] Xianglan Yao, Michael P Vitek, Alan T Remaley, and Stewart J Levine. Apolipoprotein mimetic peptides: a new approach for the treatment of asthma. *Frontiers in pharmacology*, 3:37, 2012.

[53] Malgorzata Wygrecka, Ioannis Alexopoulos, Daniel P Potaczek, and Liliana Schaefer. Diverse functions of apolipoprotein ai in lung fibrosis. *American Journal of Physiology-Cell Physiology*, 324(2):C438–C446, 2023.

[54] Oleg F Sharifov, Xin Xu, Amit Gaggar, William E Grizzle, Vinod K Mishra, Jaideep Honavar, Silvio H Litovsky, Mayakonda N Palgunachari, C Roger White, GM Anantharamaiah, et al. Anti-inflammatory mechanisms of apolipoprotein ai mimetic peptide in acute respiratory distress syndrome secondary to sepsis. *PLoS One*, 8(5):e64486, 2013.

[55] Jie Tang, Dan Li, Lindsey Drake, Wenmin Yuan, Sara Deschaine, Emily E Morin, Rose Ackermann, Karl Olsen, David E Smith, and Anna Schwendeman. Influence of route of administration and lipidation of apolipoprotein ai peptide on pharmacokinetics and cholesterol mobilization. *Journal of lipid research*, 58(1):124–136, 2017.

[56] Wilissa D'Souza, John A Stonik, Andrew Murphy, Steven J Demosky, Amar A Sethi, Xiao L Moore, Jaye Chin-Dusting, Alan T Remaley, and Dmitri Sviridov. Structure/function relationships of apolipoprotein ai mimetic peptides: implications for antiatherogenic activities of high-density lipoprotein. *Circulation research*, 107(2):217–227, 2010.

[57] Karin Kornmueller, Ivan Vidakovic, and Ruth Prassl. Artificial high density lipoprotein nanoparticles in cardiovascular research. *Molecules*, 24(15):2829, 2019.

[58] Rui Kuai, Dan Li, Y Eugene Chen, James J Moon, and Anna Schwendeman. High-density lipoproteins: nature's multifunctional nanoparticles. *ACS nano*, 10(3):3015–3041, 2016.

[59] Sean Marrache and Shanta Dhar. Biodegradable synthetic high-density lipoprotein nanoparticles for atherosclerosis. *Proceedings of the National Academy of Sciences*, 110(23):9445–9450, 2013.

[60] Maki Tsujita, Anna Wolska, Daniel AP Gutmann, and Alan T Remaley. Reconstituted discoidal high-density lipoproteins: Bioinspired nanodiscs with many unexpected applications. *Current atherosclerosis reports*, 20(12):59, 2018.

[61] Song Ih Ahn, Hyun-Ji Park, Jiwon Yom, Taeyoung Kim, and YongTae Kim. High-density lipoprotein mimetic nanotherapeutics for cardiovascular and neurodegenerative diseases. *Nano Research*, 11(10):5130–5143, 2018.

[62] TK Ritchie, YV Grinkova, TH Bayburt, IG Denisov, JK Zolnerciks, WM Atkins, and SG Sligar. Reconstitution of membrane proteins in phospholipid bilayer nanodiscs. *Methods in enzymology*, 464:211–231, 2009.

[63] Bankala Krishnarjuna, Gaurav Sharma, Sang-Choul Im, Richard Auchus, GM Anantharamaiah, and Ayyalusamy Ramamoorthy. Characterization of nanodisc-forming peptides for membrane protein studies. *Journal of colloid and interface science*, 653:1402–1414, 2024.

[64] Ilia G Denisov and Stephen G Sligar. Nanodiscs in membrane biochemistry and biophysics. *Chemical reviews*, 117(6):4669–4713, 2017.

[65] Ilia G Denisov and Stephen G Sligar. Nanodiscs for structural and functional studies of membrane proteins. *Nature structural & molecular biology*, 23(6): 481–486, 2016.

[66] Alan T Remaley, Marcelo Amar, and Dmitri Sviridov. Hdl-replacement therapy: mechanism of action, types of agents and potential clinical indications. *Expert review of cardiovascular therapy*, 6(9):1203–1215, 2008.

[67] Alan T Remaley, Fairwell Thomas, John A Stonik, Steve J Demosky, Samantha E Bark, Edward B Neufeld, Alexander V Bocharov, Tatyana G Vishnyakova, Amy P Patterson, Thomas L Eggerman, et al. Synthetic amphipathic helical peptides promote lipid efflux from cells by an abca1-dependent and an abca1-independent pathway. *Journal of lipid research*, 44(4):828–836, 2003.

[68] Muhammed A Yıldırım, Kwang-Il Goh, Michael E Cusick, Albert-László Barabási, and Marc Vidal. Drug—target network. *Nature biotechnology*, 25 (10):1119–1126, 2007.

[69] Christofer S Tautermann. Gpcr structures in drug design, emerging opportunities with new structures. *Bioorganic & medicinal chemistry letters*, 24(17): 4073–4079, 2014.

[70] Hang Yin and Aaron D Flynn. Drugging membrane protein interactions. *Annual review of biomedical engineering*, 18(1):51–76, 2016.

[71] Artem Stetsenko and Albert Guskov. An overview of the top ten detergents used for membrane protein crystallization. *Crystals*, 7(7):197, 2017.

[72] Rafael Fernandez-Leiro and Sjors HW Scheres. Unravelling biological macromolecules with cryo-electron microscopy. *Nature*, 537(7620):339–346, 2016.

[73] Peng Jin, David Bulkley, Yanmeng Guo, Wei Zhang, Zhenhao Guo, Walter Huynh, Shenping Wu, Shan Meltzer, Tong Cheng, Lily Yeh Jan, et al. Electron cryo-microscopy structure of the mechanotransduction channel nompc. *Nature*, 547(7661):118–122, 2017.

[74] Theresia Gutmann, Kelly H Kim, Michal Grzybek, Thomas Walz, and Ünal Coskun. Visualization of ligand-induced transmembrane signaling in the full-length human insulin receptor. *Journal of Cell Biology*, 217(5):1643–1649, 2018.

[75] Masakazu Miyazaki, Yoko Tajima, Tetsurou Handa, and Minoru Nakano. Static and dynamic characterization of nanodiscs with apolipoprotein ai and its model peptide. *The Journal of Physical Chemistry B*, 114(38):12376–12382, 2010.

[76] Thirupathi Ravula, Nathaniel Z Hardin, and Ayyalusamy Ramamoorthy. Polymer nanodiscs: Advantages and limitations. *Chemistry and physics of lipids*, 219:45–49, 2019.

[77] Ali Flayhan, Haydyn DT Mertens, Yonca Ural-Blimke, Maria Martinez Molledo, Dmitri I Svergun, and Christian Löw. Saposin lipid nanoparticles: a highly versatile and modular tool for membrane protein research. *Structure*, 26(2):345–355, 2018.

[78] Paul WK Rothemund. Folding dna to create nanoscale shapes and patterns. *Nature*, 440(7082):297–302, 2006.

[79] Vikram Dalal, Mark J Arcario, John T Petroff, Brandon K Tan, Noah M Dietzen, Michael J Rau, James AJ Fitzpatrick, Grace Brannigan, and Wayland WL Cheng. Lipid nanodisc scaffold and size alter the structure of a pentameric ligand-gated ion channel. *Nature communications*, 15(1):25, 2024.

[80] Jeong Joo Kim, Anant Gharpure, Jinfeng Teng, Yuxuan Zhuang, Rebecca J Howard, Shaotong Zhu, Colleen M Noviello, Richard M Walsh Jr, Erik Lindahl, and Ryan E Hibbs. Shared structural mechanisms of general anaesthetics and benzodiazepines. *Nature*, 585(7824):303–308, 2020.

[81] Vikram Babu Kasaragod, Martin Mortensen, Steven W Hardwick, Ayla A Wahid, Valentina Dorovykh, Dimitri Y Chirgadze, Trevor G Smart, and Paul S Miller. Mechanisms of inhibition and activation of extrasynaptic $\alpha\beta$ gabaa receptors. *Nature*, 602(7897):529–533, 2022.

[82] Jeffrey D Pilot, J Malcolm East, and Anthony G Lee. Effects of bilayer thickness on the activity of diacylglycerol kinase of escherichia coli. *Biochemistry*, 40(28):8188–8195, 2001.

[83] Annabella Nouel Barreto, Luis G Cuello, and Maria E Zoghbi. Abc transporter activity is affected by the size of lipid nanodiscs. *FEBS letters*, 599(4):502–511, 2025.

[84] Rachael L Grime, Richard T Logan, Stephanie A Nestorow, Pooja Sridhar, Patricia C Edwards, Christopher G Tate, Bert Klumperman, Tim R Dafforn, David R Poyner, Philip J Reeves, et al. Differences in sma-like polymer architecture dictate the conformational changes exhibited by the membrane protein rhodopsin encapsulated in lipid nano-particles. *Nanoscale*, 13(31): 13519–13528, 2021.

[85] Sang Ho Park, Sabrina Berkamp, Gabriel A Cook, Michelle K Chan, Hector Viadiu, and Stanley J Opella. Nanodiscs versus macrodiscs for nmr of membrane proteins. *Biochemistry*, 50(42):8983–8985, 2011.

[86] Søren Roi Midtgaard, Martin Cramer Pedersen, Jacob Judas Kain Kirkensgaard, Kasper Kildegaard Sørensen, Kell Mortensen, Knud J Jensen, and Lise Arleth. Self-assembling peptides form nanodiscs that stabilize membrane proteins. *Soft matter*, 10(5):738–752, 2014.

[87] Moutusi Manna, Miia Niemelä, Joona Tynkkynen, Matti Javanainen, Waldemar Kulig, Daniel J Müller, Tomasz Rog, and Ilpo Vattulainen. Mechanism of allosteric regulation of β2-adrenergic receptor by cholesterol. *Elife*, 5:e18432, 2016.

[88] OH Samuli Ollila, Martti Louhivuori, Siewert J Marrink, and Ilpo Vattulainen. Protein shape change has a major effect on the gating energy of a mechanosensitive channel. *Biophysical journal*, 100(7):1651–1659, 2011.

[89] Piotr Stepien, Bozena Augustyn, Chetan Poojari, Wojciech Galan, Agnieszka Polit, Ilpo Vattulainen, Anna Wisnieska-Becker, and Tomasz Rog. Complexity of seemingly simple lipid nanodiscs. *Biochimica et Biophysica Acta (BBA)-Biomembranes*, 1862(11):183420, 2020.

[90] Richard W Pastor. Molecular dynamics and monte carlo simulations of lipid bilayers. *Current Opinion in Structural Biology*, 4(4):486–492, 1994.

[91] James C Phillips, Willy Wriggers, Zhigang Li, Ana Jonas, and Klaus Schulten. Predicting the structure of apolipoprotein ai in reconstituted high-density lipoprotein disks. *Biophysical journal*, 73(5):2337–2346, 1997.

[92] Christopher Sheldahl and Stephen C Harvey. Molecular dynamics on a model for nascent high-density lipoprotein: role of salt bridges. *Biophysical journal*, 76(3):1190–1198, 1999.

[93] Vinod K Mishra, GM Anantharamaiah, Jere P Segrest, Mayakonda N Palgunachari, Manjula Chaddha, SW Simon Sham, and N Rama Krishna. Association of a model class a (apolipoprotein) amphipathic α helical peptide with lipid: High resolution nmr studies of peptide· lipid discoidal complexes. *Journal of Biological Chemistry*, 281(10):6511–6519, 2006.

[94] Anthony E Klon, Jere P Segrest, and Stephen C Harvey. Molecular dynamics simulations on discoidal hdl particles suggest a mechanism for rotation in the apo ai belt model. *Journal of molecular biology*, 324(4):703–721, 2002.

[95] Amy Y Shih, Ilia G Denisov, James C Phillips, Stephen G Sligar, and Klaus Schulten. Molecular dynamics simulations of discoidal bilayers assembled from truncated human lipoproteins. *Biophysical journal*, 88(1):548–556, 2005.

[96] Amy Y Shih, Anton Arkhipov, Lydia Freddolino, and Klaus Schulten. Coarse grained protein- lipid model with application to lipoprotein particles. *The Journal of Physical Chemistry B*, 110(8):3674–3684, 2006.

[97] Amy Y Shih, Peter L Freddolino, Anton Arkhipov, and Klaus Schulten. Assembly of lipoprotein particles revealed by coarse-grained molecular dynamics simulations. *Journal of structural biology*, 157(3):579–592, 2007.

[98] Siewert J Marrink, Alex H De Vries, and Alan E Mark. Coarse grained model for semiquantitative lipid simulations. *The Journal of Physical Chemistry B*, 108(2):750–760, 2004.

[99] Ananya Debnath and Lars V Schafer. Structure and dynamics of phospholipid nanodiscs from all-atom and coarse-grained simulations. *The Journal of Physical Chemistry B*, 119(23):6991–7002, 2015.

[100] Minoru Nakano, Masakazu Fukuda, Takayuki Kudo, Masakazu Miyazaki, Yusuke Wada, Naoya Matsuzaki, Hitoshi Endo, and Tetsurou Handa. Static and dynamic properties of phospholipid bilayer nanodiscs. *Journal of the American Chemical Society*, 131(23):8308–8312, 2009.

[101] Andreas N Larsen, Kasper K Sørensen, Nicolai T Johansen, Anne Martel, Jacob JK Kirkensgaard, Knud J Jensen, Lise Arleth, and Søren Roi Midtgaard. Dimeric peptides with three different linkers self-assemble with phospholipids to form peptide nanodiscs that stabilize membrane proteins. *Soft Matter*, 12 (27):5937–5949, 2016.

[102] Vinod K Mishra, Mayakonda N Palgunachari, N Rama Krishna, John Glushka, Jere P Segrest, and GM Anantharamaiah. Effect of leucine to phenylalanine substitution on the nonpolar face of a class a amphipathic helical peptide on its interaction with lipid: high resolution solution nmr studies of 4f-dimyristoylphosphatidylcholine discoidal complex. *Journal of Biological Chemistry*, 283(49):34393–34402, 2008.

[103] Vinod K Mishra and Gattadahalli M Anantharamaiah. High-resolution structural studies elucidate antiatherogenic and anti-inflammatory properties of peptides designed to mimic amphipathic α-helical domains of apolipoprotein ai. *Natural product communications*, 14(5):1934578X19849131, 2019.

[104] Rafique M Islam, Mohsen Pourmousa, Denis Sviridov, Scott M Gordon, Edward B Neufeld, Lita A Freeman, B Scott Perrin Jr, Richard W Pastor, and Alan T Remaley. Structural properties of apolipoprotein ai mimetic peptides that promote abca1-dependent cholesterol efflux. *Scientific Reports*, 8(1):2956, 2018.

[105] Mohsen Pourmousa and Richard W Pastor. Molecular dynamics simulations of lipid nanodiscs. *Biochimica et Biophysica Acta (BBA)-Biomembranes*, 1860 (10):2094–2107, 2018.

[106] Evgeniy S Salnikov, GM Anantharamaiah, and Burkhard Bechinger. Supramolecular organization of apolipoprotein-ai-derived peptides within disc-like arrangements. *Biophysical journal*, 115(3):467–477, 2018.

2 Methods

This chapter details the methods used to investigate the structure, dynamics, and morphology of peptide–lipid nanodiscs. We first introduce the classical MD framework (equations of motion, statistical ensembles, ergodicity, and integrators) alongside practical choices for force fields, long-range electrostatics, and thermostat/barostat control. We then describe the nanodisc-building protocol using the custom diskus.py tool, followed by the simulation setup in GROMACS (CHARMM36m, hydrogen-mass repartitioning, NVT and NPT equilibration, production run conditions). Finally, we summarize how key observables are calculated and, where applicable, compared with experiment: global size measures (radius of gyration and density-based diameters), peptide–lipid interactions with cutoffs established using radial distribution functions and interaction counts, peptide secondary structure (DSSP helicity), membrane organization (thickness and acyl-chain order maps), and ssNMR observables (^{2}H quadrupolar splittings and ^{15}N chemical shifts). We conclude with SAXS: how profiles are calculated from explicit-solvent MD trajectories using GROMACS-SWAXS and compared to experiment, and how SAXS curves are analyzed using Guinier plots and indirect Fourier transform (GNOM) to obtain R_g, $I(0)$, and $D_{\max}$.

Note: *In this chapter, we detail the methods used to build, simulate, and analyze the nanodisc systems. Analytical procedures that are specific to particular results are provided in the corresponding sections of Chapter 3, under Computational Details.*

2.1 Molecular Dynamics Simulations

Classical Molecular Dynamics simulation is a computational technique used to study the behavior of molecules at atomic resolution by representing them as interacting particles. The system evolves over time through the integration of Newton's equations of motion, capturing the dynamics of many-body systems. The term classical indicates that nuclear motion is treated using classical mechanics, which provides a good approximation for the translational and rotational motion of atoms in many systems [1].

Electronic degrees of freedom are neglected under the Born-Oppenheimer approx-

imation [2], which assumes that the motion of electrons and nuclei can be decoupled. This allows the system's potential energy to be expressed solely in terms of nuclear coordinates. However, this simplification limits MD's ability to capture quantum mechanical effects such as bond formation, bond breaking, and charge transfer—processes that are essential for simulating chemical reactions and charge transfer [3].

In the context of biological systems, MD simulations rely on force fields, empirical potential energy functions designed to approximate the forces between atoms [4]. These force fields are critical for determining the accuracy and reliability of simulations. Over the past few decades, force fields such as AMBER [5], CHARMM [6], and OPLS [7] have been extensively refined to reproduce a wide range of structural, kinetic, and thermodynamic properties of proteins, lipids, and nucleic acids under physiological conditions. While they are not perfect, these models have proven sufficiently accurate for many applications, particularly when simulating systems near room temperature and atmospheric pressure.

Despite these advances, MD simulations face a fundamental limitation in terms of timescale. Many biologically relevant processes, such as protein folding, protein aggregation, signal transduction, or membrane remodeling, occur over timescales ranging from nanoseconds to seconds and may involve systems with millions to billions of atoms. Simulating such large-scale events remains beyond the reach of current computational resources. Nevertheless, MD remains an invaluable tool for exploring biological mechanisms, especially when combined with prior structural knowledge or used to probe specific regions of interest within complex systems [8].

2.1.1 Newtonian Framework in Molecular Dynamics

In molecular mechanics [1], the motion of particles in a system is governed by Newton's second law of motion:

$$m_i \frac{d^2\mathbf{r}_i}{dt^2} = \mathbf{F}_i, \tag{2.1}$$

where m_i is the mass, $\mathbf{r}_i$ is the position vector, and $\mathbf{F}_i$ is the net force acting on the i-th particle. Depending on the level of resolution, a particle can represent an individual atom (in all-atom MD), a heavy atom along with its bonded hydrogens (in united-atom MD), or a group of atoms (in coarse-grained MD). To numerically solve this equation of motion, one must provide initial values for the particles' positions and velocities, as well as compute the forces acting on them at each time step.

Atomic interactions are described by a potential energy function $U(\mathbf{r}_1, ..., \mathbf{r}_N)$, which defines the energy landscape of the system as a function of atomic positions. This potential is typically derived from empirical force fields that capture the system's physical and chemical behavior. The force on any given particle is obtained by

taking the negative gradient of the potential energy with respect to its position:

$$\mathbf{F}_i = -\nabla_{\mathbf{r}_i} U(\mathbf{r}_1, ..., \mathbf{r}_N) = -\left(\frac{\partial U}{\partial x_i}, \frac{\partial U}{\partial y_i}, \frac{\partial U}{\partial z_i}\right). \tag{2.2}$$

Because molecular systems involve many interacting particles, these equations cannot be solved analytically. Instead, they are discretized and integrated numerically. The resulting MD trajectory describes the system's time evolution in phase space through its position and velocity vectors. These are updated iteratively at each time step using numerical integration algorithms such as the Verlet or velocity-Verlet methods.

2.1.2 Ensembles of statistical thermodynamics

MD simulations bridge microscopic details to macroscopic observables by sampling a vast number of microstates, which are the specific configurations of particles [9]. In a classical system, a microstate is defined by the complete set of microscopic variables (e.g., the positions and momenta of every particle. For example, specifying the coordinates and velocities of all atoms in a MD simulation defines one microstate. In contrast, a macrostate is defined by a few bulk parameters (such as total energy, volume, number of particles, temperature, pressure, etc.), which include some extensive and intensive properties of matter that describe the system's overall condition. Many different microstates can correspond to the same macrostate. For instance, if we fix a gas's total energy, volume, and particle number, there are astronomically many microscopic arrangements of molecules (positions/velocities) consistent with those values. Statistical thermodynamics provides the framework to connect these microstates to thermodynamic macrostates by considering ensembles – collections of virtual copies of the system, each representing a possible microstate consistent with given macrostate conditions. This collection of virtual copies, in other words MD trajectory.

Thermodynamic ensembles characterize the allowed fluctuations in a system's macrostate. Each ensemble is defined by which macroscopic variables are held fixed and which are allowed to fluctuate, reflecting different physical constraints. Below, we outline the major ensembles:

- Microcanonical ensemble(NVE): the number of atoms N , volume V and energy of the system E are constrained;
- Canonical ensemble(NVT): he number of atoms N , volume V and temperature E are constrained;
- Isobaric-isothermal ensemble (NPT): the number of atoms N, pressure P and temperature T are constrained;
- Grand canonical ensemble (μVT): the chemical potential μ, volume V and temperature T are constrained.

2.1.3 Ergodicity and Its Role in MD Sampling

Experiments probe macroscopic samples containing on the order of $\approx 10^{23}$ molecules, each visiting a vast configuration space. As a result, any experimental measurement, whether it's a calorimetric heat capacity, an NMR relaxation rate, or a scattering intensity, reflects an ensemble average $\langle A \rangle$, taken over all those simultaneous molecular configurations. Over all microstates $\{\mathbf{r}, \mathbf{p}\}$ with probability density $\rho(\mathbf{r}, \mathbf{p})$, the ensemble average is,

$$\langle A \rangle = \int A(\mathbf{r}, \mathbf{p})\, \rho(\mathbf{r}, \mathbf{p})\, \mathrm{d}\mathbf{r}\, \mathrm{d}\mathbf{p}. \tag{2.3}$$

In contrast, MD simulations are fundamentally constrained by computational power, they can only follow a relatively small number of particles as it evolves in times, it is possible to calculate the time average $\overline{A}$ over a large number independent copies of the system at a single instant, MD lets you compute a time average and sampling over a sufficiently long simulation. The time average is defined as,

$$\overline{A} = \lim_{T \to \infty} \frac{1}{T} \int_0^T A\big(\mathbf{r}(t), \mathbf{p}(t)\big)\, \mathrm{d}t. \tag{2.4}$$

Here, T is the total simulation time and $A\big(\mathbf{r}(t), \mathbf{p}(t)\big)$ is the observable of interest.

Despite these two very different approaches — ensemble averaging in experiments versus time averaging in MD simulations — both yield the same result under the ergodic hypothesis, a cornerstone of statistical mechanics. Ergodicity states that, provided the simulation runs long enough, the time spent in each microstate is proportional to its statistical weight. In mathematical terms, the time average of any property equals its ensemble average.

$$\overline{A} \;=\; \langle A \rangle. \tag{2.5}$$

To satisfy ergodicity, MD trajectories must be long enough for the system to cross all relevant energy barriers and explore the full configuration space. When this condition holds, one can extract experimentally relevant structural, dynamical, and thermodynamic properties directly from the trajectory. However, in practice, high free-energy barriers often trap the system in a single free-energy basin. To overcome this limitation, various enhanced-sampling techniques are employed to accelerate barrier crossing and ensure truly ergodic sampling.

2.1.4 Numerical Integrators for MD Trajectories

$$\mathbf{r}_i(t+\Delta t) = \mathbf{r}_i(t) + \Delta t\,\mathbf{v}_i(t) + \frac{\Delta t^2}{2}\,\mathbf{a}_i(t) + \frac{\Delta t^3}{6}\,\dot{\mathbf{a}}_i(t) + \mathcal{O}(\Delta t^4), \tag{2.6}$$

$$\mathbf{v}_i(t+\Delta t) = \mathbf{v}_i(t) + \Delta t\,\mathbf{a}_i(t) + \frac{\Delta t^2}{2}\,\dot{\mathbf{a}}_i(t) + \mathcal{O}(\Delta t^3), \tag{2.7}$$

Three widely used schemes, Verlet, leap-frog, and velocity-Verlet, are discussed in this section [10], [11].

Verlet Integration In the Verlet algorithm, the new positions are obtained from the current and previous positions plus the current force:

$$\mathbf{r_i}(t+\Delta t) = 2\,\mathbf{r_i}(t) - \mathbf{r_i}(t-\Delta t) + \frac{\Delta t^2}{m_i}\,\mathbf{F_i}(t) + \mathcal{O}(\Delta t^4). \tag{2.8}$$

$$\mathbf{v_i}(t) \;=\; \frac{\mathbf{r_i}(t+\Delta t) \;-\; \mathbf{r_i}(t-\Delta t)}{2\,\Delta t} \;+\; \mathcal{O}(\Delta t^2). \tag{2.9}$$

Velocities are then reconstructed by finite differences of positions, which suffices for computing observables (*e.g.* Kinetic energy) but is not required to compute the trajectory.

Velocity-Verlet Integration Velocity-Verlet provides positions, velocities, and forces at the same integer time steps. Positions are advanced using current velocities and forces:

$$\mathbf{r_i}(t+\Delta t) = \mathbf{r_i}(t) + \Delta t\,\mathbf{v_i}(t) + \frac{\Delta t^2}{2m_i}\,\mathbf{F_i}(t), \tag{2.10}$$

and velocities are then corrected using the average of the old and new forces:

$$\mathbf{v_i}(t+\Delta t) = \mathbf{v_i}(t) + \frac{\Delta t}{2m_i}\Big[\mathbf{F_i}(t) + \mathbf{F_i}(t+\Delta t)\Big]. \tag{2.11}$$

This scheme is algebraically equivalent to the original Verlet integrator but yields velocities at integer steps, simplifying thermostatting and observable evaluation.

Leap-Frog Integration The leap-frog scheme staggers positions and velocities by half a time step. First, velocities at $t + \frac{1}{2}\Delta t$ are updated using the force at time t:

$$\mathbf{v_i}\Big(t + \tfrac{1}{2}\Delta t\Big) = \mathbf{v_i}\Big(t - \tfrac{1}{2}\Delta t\Big) + \frac{\Delta t}{m_i}\,\mathbf{F_i}(t), \tag{2.12}$$

then positions at $t + \Delta t$ follow directly:

$$\mathbf{r_i}(t + \Delta t) = \mathbf{r_i}(t) + \Delta t\, \mathbf{v_i}\Big(t + \tfrac{1}{2}\Delta t\Big). \tag{2.13}$$

Because positions and velocities "leap" past one another, the leapfrog method reduces local error compared to the basic Verlet method.

To ensure energy conservation, Δt must be smaller than the period of the fastest molecular motions, typically bond vibrations. A common approach is to constrain bonds involving hydrogen using algorithms such as SHAKE [12], RATTLE [13], LINCS [14], or SETTLE [15], which enforce fixed bond lengths via Lagrange multipliers or projection methods (only for the water molecules). This allows stable integration with $\Delta t \approx 2$ fs.

In this thesis, all simulations were performed with GROMACS utilizing the default leap-frog integrator. To accelerate the MD simulation, we implemented hydrogen mass repartitioning (HMR) [16], a technique that redistributes a small fraction of mass from each heavy atom onto its bonded hydrogen(s). By increasing hydrogen masses (e.g., from $\approx 1.0amu$ to $\approx 3.0amu$) and correspondingly decreasing the adjacent heavy-atom masses, HMR attenuates the highest-frequency X–H vibrational modes, thereby permitting a stable integration time step of 4 fs instead of the conventional 2 fs. This redistribution conserves the total mass of each residue. The HMR method yields approximately a twofold acceleration in trajectory generation with only minimal perturbation to structural ensembles and thermodynamic properties.

2.1.5 Force Fields and Potential Energy Functions

Molecular dynamics simulations derive atomic forces from a predefined *force field*, a potential energy function U that balances accuracy with computational efficiency. Common biomolecular force fields (GROMOS [17], CHARMM [6], AMBER [5]) employ a classical treatment of particle-particle interactions, following the fixed-bond framework, which does not allow the bonds to dissociate, and the function U typically decomposes into bonded and non-bonded contributions:

$$U \;=\; E_{\text{bond}} + E_{\text{angle}} + E_{\text{torsion}} + E_{\text{elec}} + E_{\text{vdw}} \tag{2.14}$$

Bonded interactions:

$$E_{\text{bond}} = \sum_{i,j} k^b_{ij}\,(r_{ij} - r^0_{ij})^2 \quad \text{(bond stretching)} \tag{2.15}$$

$$E_{\text{angle}} = \sum_{i,j,k} k^a_{ijk}\,(\alpha_{ijk} - \alpha^0_{ijk})^2 \quad \text{(angle bending)} \tag{2.16}$$

$$E_{\text{torsion}} = \sum_{i,j,k,l} k^t_{ijkl}\big[1 + \cos(n\,\omega_{ijkl} - \omega^0_{ijkl})\big] \quad \text{(torsional rotation)} \tag{2.17}$$

where r_{ij} is the distance between atoms i and j, r^0_{ij} their equilibrium bond length, α_{ijk} the angle formed by atoms i, j, and k with equilibrium value α^0_{ijk}, ω_{ijkl} the dihedral angle about the bond $i{-}j{-}k{-}l$ with reference phase ω^0_{ijkl} and multiplicity n; and k^b_{ij}, k^a_{ijk}, k^t_{ijkl} are the bond, angle and torsion force constants, respectively.

Non-bonded interactions:

$$E_{\text{elst}} = \sum_{i,j} \frac{q_i q_j}{4\pi\varepsilon_0\, r_{ij}} \quad \text{(Coulomb electrostatics)} \tag{2.18}$$

$$E_{\text{vdw}} = \sum_{i,j} \varepsilon_{ij}\left[\left(\frac{\sigma_{ij}}{r_{ij}}\right)^{12} - 2\left(\frac{\sigma_{ij}}{r_{ij}}\right)^{6}\right] \quad \text{(van der Waals / Lennard-Jones)} \tag{2.19}$$

where q_i and q_j are the partial charges on atoms i and j; ε_{ij} and σ_{ij} are the Lennard–Jones well depth and collision diameter; and ε_0 is the permittivity of free space. In this thesis, all simulations were conducted using the CHARMM36m force field [18].

2.1.6 Periodic Boundary Conditions and Long-range interactions

A typical MD simulation contains anywhere from thousands to millions of atoms; in our work, we simulated a system of roughly 7×10^5 atoms. Under these conditions, a large fraction of atoms lies near the boundaries of the simulation box, making it inappropriate for deriving true bulk properties, since most atoms feel the influence of the walls. To minimize this surface effect—often called the boundary effect and more closely mimic the behavior of a real macroscopic system, we employ periodic boundary conditions (PBCs) [1].

The essential idea behind PBCs is to simulate an infinite system by replicating our finite cell indefinitely. When a particle exits one face of the box, it re-enters through the opposite face, and the "loss" of the original particle is exactly balanced by its periodic image. Because we only integrate the primary cell and retrieve any replica positions by simple translations, we dramatically reduce computational cost while preserving bulk behavior.

However, long-range nonbonded interactions require special attention under PBCs. Van der Waals forces decay rapidly ($\sim r^{-6}$), so we can safely truncate them beyond a cutoff (typically 9–12 Å), chosen to be less than half the box length to prevent a particle from interacting with its own image. In contrast, electrostatic interactions, described by the Coulomb potential ($\sim r^{-1}$), decay much more slowly, so a naive cutoff introduces significant errors. The most widely used remedy is Ewald summation [19], and its modern, efficient implementation is the particle-mesh Ewald (PME) method [20].

In PME, the total electrostatic potential

$$\varphi(\mathbf{r}) = \varphi_{\mathrm{sr}}(\mathbf{r}) + \varphi_{\ell}(\mathbf{r}) \tag{2.20}$$

is split into a short-range component, φ_{sr}, summed directly in real space, and a long-range component, φ_{ℓ}, summed in Fourier space (Reciprocal-space). The total energy:

$$E_{\mathrm{tot}} = \sum_{i,j} \varphi(\mathbf{r}_j - \mathbf{r}_i) = E_{\mathrm{sr}} + E_{\ell} \tag{2.21}$$

The short-ranged potential in real space:

$$E_{\mathrm{sr}} = \sum_{i,j} \varphi_{\mathrm{sr}}(\mathbf{r}_j - \mathbf{r}_i) \tag{2.22}$$

The long-range contribution in reciprocal space:

$$E_{\ell} = \sum_{\mathbf{k}} \tilde{\Phi}_{\ell}(\mathbf{k}) \left|\tilde{\rho}(\mathbf{k})\right|^2. \tag{2.23}$$

where $\tilde{\rho}(\mathbf{k})$ is the Fourier transform of the charge density and $\tilde{\Phi}_{\ell}(\mathbf{k})$ is the transformed long-range kernel. Because both sums converge rapidly in their respective domains, they can be truncated with minimal loss of accuracy, yielding a significant speed-up over direct all-pairs Coulomb calculations.

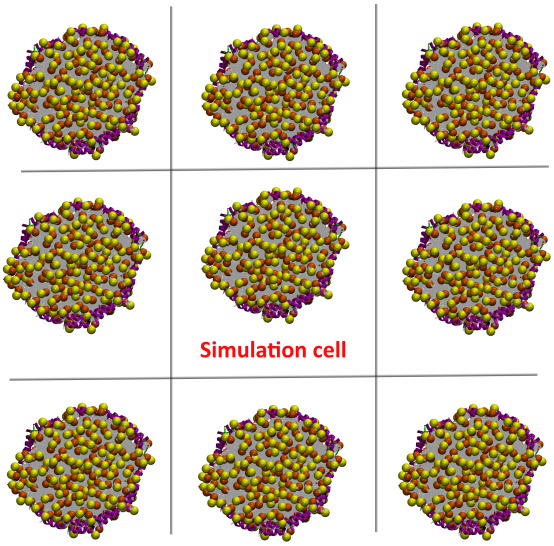

Figure 2.1: Illustration of periodic boundary conditions (PBC) in a molecular simulation. A finite number of atoms is modeled within a central simulation cell, which is replicated in all three spatial directions to approximate bulk behavior and minimize finite-size effects. For clarity, only the two in-plane periodic images (x–y plane) surrounding the primary cell are shown.

2.1.7 Thermostats

Molecular dynamics simulations are fundamentally governed by the integration of classical Newtonian equations of motion, thereby generating trajectories that sample the microcanonical (NVE) ensemble by default [1]. However, to replicate experimental conditions such as constant temperature or pressure and it is often necessary to sample from alternative statistical ensembles. Consequently, MD simulations are typically conducted under conditions in which temperature (and pressure, when applicable) is held constant on average.

Temperature control in simulations is typically implemented by modifying the equations of motion or altering particle velocities. The algorithms employed to regulate the system's temperature toward a predefined target are referred to as thermostats.

For isothermal–isochoric (NVT) ensemble simulations, a variety of thermostats have been widely adopted, including the Andersen thermostat, stochastic dynamics (SD), Berendsen thermostat, velocity-rescaling (V-rescale) thermostat, and the Nosé–Hoover thermostat. These methods are broadly categorized into two classes:

2.1.7.1 Velocity randomizing algorithms (Andersen and SD thermostats):

Andersen thermostat [21] enforces temperature control through stochastic velocity reassignment, wherein particle velocities are periodically redrawn from the Maxwell–Boltzmann distribution.

Two common implementations of the Andersen thermostat are:

(i) In the original Andersen scheme, each particle is randomly selected to have its velocity reassigned at each time step with a fixed probability.

(ii) In the Andersen-Massive (or Andersen-M) approach, the velocities of *all* particles are simultaneously randomized at fixed intervals of $\tau_T/\Delta t$, where Δt is the simulation time step and τ_T is a characteristic coupling time constant.

Another widely used *velocity-randomizing* method is the *stochastic dynamics* (SD) thermostat, which is based on integrating the Langevin equation of motion. This approach maintains the system temperature by incorporating both a frictional damping term and a stochastic noise term into the Newtonian equations of motion:

$$m_i(d^2r_i/dt^2) = -m_i\gamma_i(dr_i/dt) + F_i(r) + r_i \tag{2.24}$$

where γ_i is the friction constant $(1/ps)$ of particle i and r_i is the noise process of particle i.

2.1.7.2 Velocity scaling algorithms (Berendsen, V-rescale and Nosé-Hoover thermostats):

The system's temperature can be regulated by scaling the particles' velocities. In the case of the Berendsen thermostat [22], the heat flow into or out of the system is controlled by rescaling the velocities of all particles at each simulation step (or every n_{TC} steps) by a time-dependent factor λ, defined as:

$$\lambda = \sqrt{\left[1 + \frac{n_{TC}\Delta}{\tau_T}\left\{\frac{T_0}{T(t-\frac{1}{2})\Delta t} - 1\right\}\right]} \tag{2.25}$$

where T_0 is the target temperature, T is the instantaneous temperature of the system, Δt is the integration time step, and τ_T is the temperature coupling time constant (which is close to, but not exactly equal to, the characteristic temperature relaxation time τ). The main consequence of this algorithm is that it does not strictly generate a canonical ensemble but rather exhibits weak coupling to the heat bath, leading to exponential relaxation of the system's temperature toward T_0.

$$\frac{dT}{dt} = \frac{T_0 - T}{\tau_T} \tag{2.26}$$

A later extension of the Berendsen thermostat, the *velocity-rescale* (V-rescale) thermostat [23], improves upon this by enforcing the correct canonical distribution of kinetic energy. This is achieved by adding a carefully constructed stochastic term to the Berendsen formalism. The kinetic energy K evolves according to the following stochastic differential equation:

$$dK = (K_0 - k)\frac{dt}{\tau_T} + 2\frac{dW}{\tau_T}\sqrt{\frac{K_0 K}{N_f}} \tag{2.27}$$

where N_f is the number of degrees of freedom and dW is a Wiener process representing Gaussian white noise.

The Nosé–Hoover thermostat employs an extended system formalism to regulate temperature. It introduces an additional dynamical variable ξ acting as a thermal reservoir, and modifies the equations of motion through a non-Newtonian friction term. The evolution of the friction coefficient is governed by:

$$\frac{d^2 r_i}{dt^2} = \frac{F_i}{m_i} - \frac{P_\xi}{Q}\frac{dr_i}{dt} \tag{2.28}$$

$$\frac{dp_\xi}{dt} = (T - T_0) \tag{2.29}$$

where p_ξ is the momentum associated with the thermostat variable ξ, Q is the mass parameter of the thermostat (controlling the coupling strength).

Among the thermostats discussed above, the Andersen and stochastic dynamics (SD) thermostats, which are classified as *velocity randomizing* methods, can rigorously sample the canonical (NVT) ensemble. However, because velocity reassignment is stochastic, it may dampen the system's intrinsic dynamics.

In contrast, Berendsen, V-rescale, and Nosé–Hoover thermostats [24] are considered *velocity scaling* approaches, which generally preserve the system's dynamical behavior. The Berendsen thermostat suppresses kinetic energy fluctuations and does not correctly sample the canonical ensemble. The Nosé–Hoover thermostat, in principle, generates a proper NVT distribution, but its deterministic dynamics can lead to oscillatory behavior, especially in systems far from equilibrium. Nevertheless, as our system operates near equilibrium, the use of the Nosé–Hoover thermostat is expected to be appropriate.

2.1.8 Barostats

When molecular dynamics simulations are performed to sample the isothermal–isobaric (NPT) ensemble, specialized algorithms known as *barostats* are employed. These algorithms modify the equations of motion (or velocities) of particles to maintain the system's pressure constant on average, analogous to how thermostats control temperature.

Among the widely used barostats, the *Berendsen barostat* [22] adjusts the system's pressure by scaling atomic coordinates and simulation box vectors at each time step. This results in a first-order kinetic relaxation of the system's pressure toward a target reference pressure P_0, governed by:

$$\frac{dP}{dt} = \frac{P_0 - P}{\tau_P} \tag{2.30}$$

where τ_P is the pressure coupling time constant, P is the instantaneous pressure, and P_0 is the target pressure. Although the Berendsen barostat quickly equilibrates the system, it suppresses natural volume fluctuations and therefore does not correctly sample the NPT ensemble.

In contrast, the *Parrinello–Rahman barostat* [24], [25] extends the system's Hamiltonian by introducing additional degrees of freedom associated with the simulation box, analogous to the approach used in the Nosé–Hover thermostat for temperature control. This barostat allows each unit vector of the simulation cell to fluctuate independently, enabling changes not only in volume but also in box shape. The box

dynamics are governed by:

$$\frac{d^2 r_i}{dt^2} = \frac{F_i}{m_i} - M\frac{dr_i}{dt} \tag{2.31}$$

$$M = b^{-1}[b\frac{db'}{dt} + \frac{db}{dt}b']b'^{-1} \tag{2.32}$$

$$\frac{db^2}{dt^2} = VW^{-1}b^{-1}(P - P_{ref}) \tag{2.33}$$

where **b** is the matrix of box vectors, V is the current volume, **P** and $\mathbf{P}_{\text{ref}}$ are the instantaneous and reference pressures, respectively, and **W** is a mass parameter matrix controlling the strength of coupling.

The Parrinello–Rahman barostat correctly samples the NPT ensemble and permits anisotropic deformation of the simulation box. However, it can introduce unphysical oscillations, especially when the system is far from equilibrium. Overall, Nosé-Hoover/V-rescale thermostat and Parrinello-Rahman barostat with moderate coupling strength are recommended for common NVT/NPT production simulations. In this thesis, we employed the Nosé-Hoover thermostat and the Parrinello-Rahman barostat algorithm to maintain constant temperature and constant pressure during the simulation.

2.2 Building Peptide-based Nanodiscs

In this thesis, we set out to characterize apoA-I mimetic peptide-based nanodiscs. Because no widely accepted model or standardized protocol exists for constructing this type of nanodisc, we decided to establish a working procedure from scratch. These peptide-based nanodiscs are distinct from membrane scaffold protein-based nanodiscs: in MSP systems, several α-helices are covalently linked to form a continuous belt around the lipid bilayer patch, whereas in peptide-based nanodiscs, the peptides interact exclusively through noncovalent forces. Over the past few decades, researchers have attempted to determine peptide orientation in the presence of lipid bilayers using ssNMR, as well as a range of other biophysical techniques such as CD spectroscopy, DLS, and SAXS, to assess α-helix content, overall shape, and particle size. Based on the existing data, we built a general protocol for preparing peptide-based nanodiscs. We developed a Python-based script, *diskus.py*, for the construction and optimization of lipid nanodisks. The rest of this section will explain how the script works and how to use it to construct nanodisk models. In the Results section, we further validate the model and test the system's stability by analyzing the factors that contribute to it.

2.2.1 Peptides of Interest

As outlined in the Sections:1.4 and 1.4.1, apoA-I mimetic peptide/lipid particles have mainly been studied using variants of an 18-amino-acid amphipathic α-helical peptide of the so-called class A type. The canonical apoA-I mimetic peptide "18A"—also referred to by the number of phenylalanines it contains (e.g., 2F) has frequently been modified through targeted substitutions to enhance functionality [26–29]. Replacing leucines at positions 3 and 14 with phenylalanines yields the 4F peptide. Phase I trials of 4F have shown improvements in the cholesterol efflux when administered in vivo [30]. Linking two such 4F peptides with a proline spacer produces 4FP4F, which our collaborators have demonstrated can suppress eosinophil recruitment and chemotaxis [31]. A shorter derivative, 14A [32], was generated by substituting the tryptophan residue of 18A with tyrosine—reducing background fluorescence when other polypeptides are reconstituted into 14A–lipid nanodiscs and assessed by fluorescence spectroscopy—and by omitting one helical turn. This shortening simplifies synthesis and facilitates stable-isotope labeling for NMR studies, while maintaining strong peptide–lipid interactions, making 14A a suitable platform for membrane protein characterization.

We selected these peptides both for their documented in vivo activities and for their capacity to serve as platforms for characterizing membrane proteins. Additionally, our collaborators performed extensive biophysical characterization and preliminary and advanced biological testing of apoA-I mimetic nanoparticles. Guided by these findings, we sought to investigate the intramolecular interactions that determine the supramolecular assemblies at a molecular level and to identify sequence “hot spots” that stabilize the particles.

Investigated peptides:
18A/2F: Ac-DWLKAFYDKVAEKLKEAF-NH_2
4F: Ac-DWFKAFYDKVAEKFKEAF-NH_2
4FP4F: Ac-DWFKAFYDKVAEKFKEAF-P-DWFKAFYDKVAEKFKEAF-NH_2
14A: Ac-DWFKAFYDKLKEAF-NH_2

2.2.2 Construction of Peptide-based Nanodiscs: *diskus.py*

2.2.2.1 Peptide Orientation:

In order to build the apoA-I mimetic peptide-based nanodiscs, synthetic peptide-based nanodiscs at the atomic level resolution, the first step is to generate the peptides using the PEP-FOLD webserver [33], with subsequent N- and C-terminal modifications by acetylation and amidation performed through CHARMM-GUI [34]. This capping group has been shown to increase the helical content of peptides, both lipid-associated and non-lipid-associated, in aqueous solution.

Based on the previous NMR studies on 18A (Fig. 9 in [27]), 14A (Fig. 4 in [32]), and 4F (Fig. 12 in [28]), peptides were assembled into antiparallel dimers, ensuring the charged residues were oriented outwards. This initial dimer configuration was optimized through iterative trials involving short energy minimizations to resolve the steric clashes between the peptide side chains. This optimized peptide dimeric arrangement is the best possible guess to start, which is based on existing reported ssNMR studies on AAM peptides. This optimized dimeric arrangement of peptides facilitated the pre-assembly of an amphipathic, belt-like structure encircling the lipid bilayer discolidal patch.

2.2.2.2 Arranging the peptides and optimizing the belt

The next step involves constructing a peptide belt by arranging the optimized dimeric form. The input peptide's length is computed under the default assumption that the peptide exists as a dimer. Consequently, the program calculates the distance between atom-1, the first atom in the peptide, and atom-2, the last atom of the first monomer, as illustrated in the Figure 2.2.

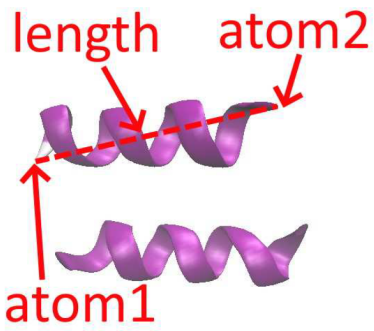

Figure 2.2: Measured length of an input peptide, which consists of two α-helical monomers.

It is crucial to recognize that this measurement is approximate and subject to minor inaccuracies, serving only as an initial estimate. Next, the belt's dimensions are determined based on the user-defined number of dimers. The peptide belt can be most closely approximated by a polygon with edges equal to the number of peptide dimers. However, for simplicity, it is approximated by a circle. Initially, the circle's circumference is determined by multiplying the peptide length by the desired number of peptides in the nanodisk. From this circumference, the radius of the circle is then calculated according to the Equation 2.34, where N peptides denote the number of peptide dimers in the system.

$$Radius = \frac{length.N.peptides}{2\pi} \tag{2.34}$$

$$\alpha = \frac{2\pi}{N.peptides} \tag{2.35}$$

Once we have the radius, we construct the first approximation of the belt. This is achieved by positioning the peptide dimer blocks in a circular arrangement based on the calculated radius. Each dimer is first translated by the calculated radius and rotated from its original coordinates by a multiple of α to fit around the circle. The translation vector is determined by the current radius, which dictates how far each dimer should be placed from the center of the circle. The angle of rotation For each dimer, the calculation is based on the total number of dimers, ensuring they are evenly spaced around the circle's circumference, as shown in the Equation 2.35 and Figure 2.3.

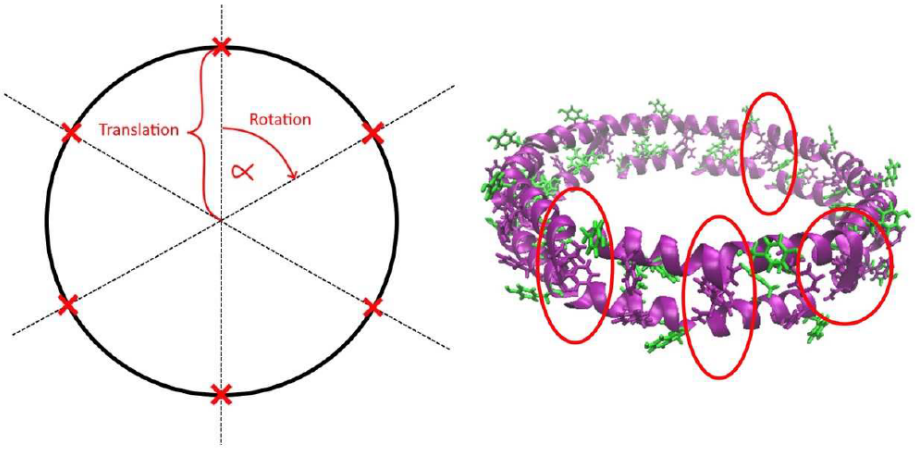

Figure 2.3: Left: Diagram explaining the rotation and translation of each dimer in the initial configuration. Right: Initial configuration of a belt with 10 proteins. Several collisions are visible (highlighted in red).

After all dimeric blocks are positioned, the next step is to check for collisions at the interface. This involves measuring the distances between atoms of different dimeric blocks. If any distances are found to be less than a predefined collision threshold (2 Å by default), it indicates an overlap, or collision, between proteins, as shown in the Figure 2.3. This is almost always the case, as both the measured length of the dimer and the approximation with a circle are imperfect.

When collisions are detected, the radius is incrementally increased by 1 Å to provide more space between the peptides, and the positioning process is repeated. This iterative approach ensures that the peptide dimeric blocks are repositioned with each increase in radius, continuously improving the structure until no collisions are present. This process is repeated until an optimal radius is found where all blocks are positioned without any overlap. This adjustment guarantees a stable and optimized belt structure, as shown in the Figure 2.4. Once the peptide belt is ready, the next step is filling the inside with an equilibrated lipid bilayer.

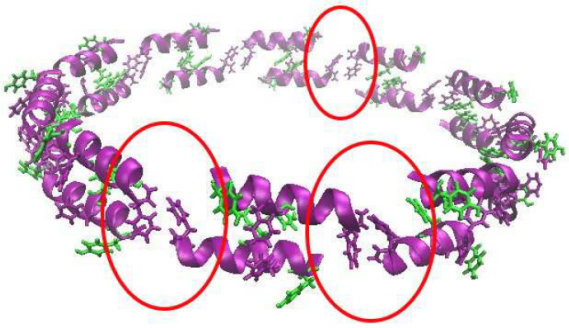

Figure 2.4: Optimized configuration of a belt with 10 proteins. The collisions from Figure 2.3 have been resolved (highlighted in red) by increasing the radius of the belt.

2.2.2.3 Equilibrated lipid bilayer-slab to Lipid-disc

The initial lipid bilayer slab was constructed with the CHARMM-GUI Membrane Builder and equilibrated following the simulation protocol described in Section 2.2.3. To create the nanodisc core, a circular patch of the bilayer was carved out with a default radius of 5Å—chosen to be smaller than the peptide-belt radius. First, the phosphorus atoms of all phospholipid headgroups were selected, and their geometric center in the xy-plane was calculated. This center served as the reference from which the distance of every atom in the slab was measured; only atoms lying within the target radius were retained and written to a new coordinate file.

Starting from a pre-equilibrated membrane ensures that the extracted disc inherits a realistic area per lipid and acyl-chain order. A limitation of this approach is that it assumes a single lipid species; tailoring the disc to arbitrary mixtures in precise ratios is not yet supported. Future versions of the script will address this by inserting additional lipid molecules sequentially until the desired composition is reached.

2.2.2.4 Assembly and solvation

The final stage in nanodisc construction consists of merging the peptide belt with the pre-trimmed lipid disc. At this point, all steric clashes between lipid molecules and belt peptides must be eliminated, as even a single collision can compromise nanodisc stability. Accordingly, every lipid molecule located at the disc rim is screened: all inter-atomic distances between that lipid and the peptide belt are computed, and if any pair lies below the van-der-Waals cutoff, the entire lipid is removed. The remaining lipids are then combined with the peptide belt and saved as a single coordinate file.

The peptide–lipid assembly is subsequently solvated in explicit water containing 0.15

M NaCl. The required numbers of water molecules and ions are calculated from the solvent-accessible volume of the chosen simulation box and the target ionic strength, after which the system is packed using Packmol [35]. The overall workflow of the pipeline is sketched out in a figure. 2.5

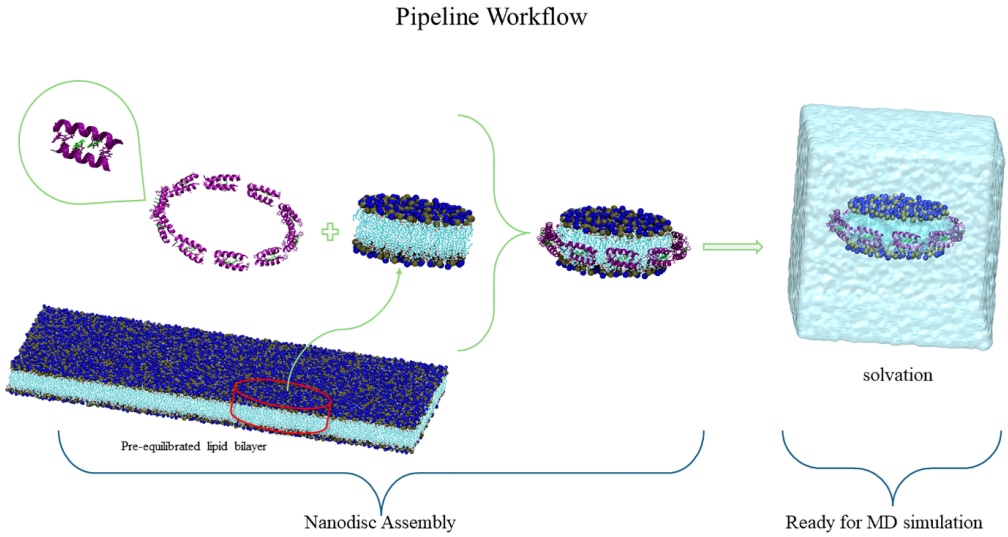

Figure 2.5: The picture illustrates a two-part continuous process. In Part 1, the assembly of nanodiscs is depicted, showing their sequential formation. Part 2 demonstrates the use of Packmol for the organized packing of water and ions around the assembled nanodiscs.

Throughout this thesis, nanodiscs were built from DMPC. Although the construction script still requires minor manual intervention, it reliably produces the peptide-based nanodiscs needed for the present work. Future developments will focus on fully automating the pipeline and adding an optimization step that orients peptides automatically on the basis of ssNMR-derived parameters, namely quadrupolar splittings and chemical-shift restraints.

2.2.3 Simulation Protocol

All simulations were conducted using the CHARMM36m force field [18] and the GROMACS software suite [36]. Before the long equilibration and production runs, each system was first energy-minimized using the steepest descent algorithm to relax any unfavorable steric clashes or bond strains introduced during setup. In this stage, atomic coordinates were iteratively adjusted along the negative gradient of the potential energy surface until either the maximum force on any atom dropped below 1000 $kJmol^{-1}nm^{-1}$ or 5000 steps were completed. This ensures that no atoms sit unphysically close and that the system starts from a low-energy configuration.

Following energy minimization, each system underwent a multi-step equilibration protocol, beginning with 2 ns simulations at constant temperature and volume

(NVT), followed by constant temperature and pressure (NPT) simulations using a 1 fs timestep. During equilibration, positional restraints on peptide backbones and lipid headgroups were gradually released to allow the system to relax. Production MD simulations were then performed with a 4 fs timestep using HMR [37] at constant temperatures of either 303.15 K or 310.15 K and a constant pressure of 1 bar. Temperature was controlled using the Nosé–Hoover thermostat [24] with a relaxation time $\tau_t = 0.5$ ps. Pressure was maintained isotropically at 1 bar, with a compressibility of $3 \times 10^{-4}\,\mathrm{bar}^{-1}$, using the Parrinello–Rahman barostat [38] with a relaxation time $\tau_p = 4.0$ ps.

Long-range electrostatics beyond 1.0 nm were computed using the PME method [20], and van der Waals interactions were switched to zero for distances larger than 1.0 nm. All simulations employed three-dimensional periodic boundary conditions. This protocol ensured robust nanodisc construction and simulation, enabling a detailed investigation of their structure, dynamics, and stability. In addition, a pure bilayer of DMPC was simulated using the same protocol, except with the NPT ensemble and anisotropic pressure control. Specific simulation details for each system are provided in the relevant sections of the chapter. Unless stated otherwise, all systems in this thesis were simulated using this same protocol.

2.3 Analysing Simulation

Unless otherwise noted, all analyses were performed with GROMACS tools [36] and the MDAnalysis [39] library. When existing tools were available but proved too slow, we accelerated those calculations with optimized in-house scripts, and in cases where no suitable code existed, we developed new programs from scratch to fulfill the required analyses.

2.3.1 Radius of Gyration (Rg)

Radius of Gyration (Rg) is a structural property that quantifies the compactness of a molecule. It is defined as the mass-weighted root mean square distance of a collection of atoms from their common center of mass:

$$R_g = \sqrt{\frac{1}{M}\sum_{i=1}^{N} m_i \left|\mathbf{r}_i - \mathbf{r}_{\mathrm{com}}\right|^2}, \tag{2.36}$$

where M is the total mass, m_i is the mass of atom i, $\mathbf{r}_i$ is the position vector of atom i, and $\mathbf{r}_{\mathrm{com}}$ is the center of mass of the system. A lower R_g indicates a more compact structure, while a higher value suggests a more extended conformation.

In **GROMACS**, the radius of gyration can be calculated using the built-in tool `gmx gyrate` [36]. This tool computes R_g along a trajectory for a specified group of atoms, enabling analysis of structural changes such as folding, unfolding, or compaction. We performed a preliminary analysis by assessing (R_g) as an initial indicator of system equilibration. While R_g alone does not definitively prove system equilibration, it enables us to assess the convergence of the overall dimension of the nanodisc convergence point.

2.3.2 Radial Distribution Function (RDF)

The radial distribution function, $g(r)$, quantifies the probability of finding a particle at a distance r from a reference particle relative to an ideal, spatially uniform distribution. In molecular dynamics, it is a central descriptor of structure because it captures short- and medium-range order directly from trajectories and is readily connected to coordination numbers and specific interactions.

For a mixture of species α and β, the partial pair distribution function is

$$g_{\alpha\beta}(r) = \frac{1}{4\pi r^2 \rho_\beta} \left\langle \frac{1}{N_\alpha} \sum_{i\in\alpha} \sum_{\substack{j\in\beta \\ j\neq i}} \delta\big(r - |\mathbf{r}_i - \mathbf{r}_j|\big) \right\rangle, \tag{2.37}$$

where ρ_β is the number density of species β, N_α is the number of reference particles of type α, and the angle brackets denote an average over time frames of the MD trajectory. In discretized form, $g_{\alpha\beta}(r)$ is obtained by binning interparticle distances, normalizing by the shell volume $4\pi r^2 \Delta r$ and ρ_β, and averaging over time. In homogeneous bulk systems $g_{\alpha\beta}(r) \to 1$ as $r \to \infty$; peaks at short r mark preferred separations and interaction shells.

The coordination number of β around α up to a cutoff r_c is given by

$$n_{\alpha\beta}(r_c) = 4\pi\rho_\beta \int_0^{r_c} g_{\alpha\beta}(r)\, r^2\, \mathrm{d}r, \tag{2.38}$$

and is typically evaluated by integrating to the first minimum of $g_{\alpha\beta}(r)$, yielding the average number of neighbors in the first shell. In practice, we compute $g_{\alpha\beta}(r)$ with `gmx rdf` in GROMACS, selecting chemically meaningful groups (for example, peptide side-chain heavy atoms vs. lipid phosphate P or choline N, or lipid acyl carbons to assess chain packing), using bin widths Δr in the range 0.005–0.01 nm and cutoffs limited by half the smallest box dimension. Periodic boundary conditions and minimum-image conventions are handled internally by the software.

2.3.3 Atomic Mass Density Distribution

To estimate the average nanodisc diameter, we calculated the atomic mass density distribution, assuming a discoidal shape. The diameter was determined by measur-

ing the span along both the major and minor axes of the disc, denoted as x and y, respectively. These measurements were derived from the spatial mass density profiles centered on the nanodisc's center of mass.

The mass density distributions of the peptide and lipid components were computed using the `gmx density` [36] tool in GROMACS. The density was calculated as a function of position in the x and y directions by dividing the system into spatial bins and summing the mass contributions in each bin:

$$\rho(\mathbf{r}) = \frac{1}{V_{\text{bin}}} \sum_{i \in \text{bin}} m_i, \tag{2.39}$$

where $\rho(\mathbf{r})$ is the local mass density at position $\mathbf{r}$, V_{bin} is the volume of each bin, and m_i is the mass of atom i within the bin.

To ensure symmetry and consistency in the measurements, the density profiles were symmetrized about the nanodisc's center of mass. The nanodisc's average diameter was then calculated by identifying the distances from the center of mass to the points on either side of the x and y axes where the mass density dropped to 1 kg/m^3. These cutoff points defined the edge of the nanodisc along each axis, and the diameters were taken as twice those distances. The final average diameter was computed as the mean of the major and minor axis diameters:

$$D_{\text{avg}} = \frac{1}{2}(D_x + D_y), \tag{2.40}$$

where D_x and D_y are the measured diameters along the x and y axes, respectively.

2.3.4 DSSP algorithm and Helicity Calculation

The Dictionary of Secondary Structure of Proteins (DSSP) [40] is a widely adopted algorithm for assigning per-residue secondary structure based on backbone hydrogen-bond patterns and local geometry. DSSP identifies intra-backbone hydrogen bonds by computing an electrostatic interaction energy E for each potential N–H O=C contact. A hydrogen bond is considered present if:

$$E = 0.084 \left(\frac{1}{r_{\text{ON}}} + \frac{1}{r_{\text{CH}}} - \frac{1}{r_{\text{OH}}} - \frac{1}{r_{\text{CN}}} \right) \times 332 \quad \text{(kcal/mol)}$$

where:

- $r_{\text{ON}}, r_{\text{CH}}, r_{\text{OH}}, r_{\text{CN}}$ are interatomic distances between O–N, C–H, O–H, and C–N, respectively;

- A hydrogen bond is assigned if $E < -0.5$ kcal/mol.

Based on patterns of these hydrogen bonds, secondary structure labels are assigned to residues using the following one-letter codes:

H	α-helix
G	3_{10}-helix
I	π-helix
E	β-strand (extended)
B	$isolated\beta$-bridge
T	$turn(H-bonded)$
S	$bend(highcurvature)$
C	$coil/loop$

2.3.4.1 Calculation of Helicity (%)

To quantify the fraction of residues adopting α-helical conformation over a simulation, the following formula is used:

$$\text{Helicity } (\%) = \frac{N_H}{N_{\text{total}}} \times 100 \tag{2.41}$$

where: N_H = number of residue per peptide labeled as "H" and

N_{total} = total number of residue per peptide.

Thus, DSSP enables robust secondary-structure annotation at the per-residue level, and the helicity percentage derived from it provides a quantitative measure of α-helix content across trajectories.

2.3.5 To Calculate the Interactions: Radial Density Distribution

To characterize interactions between peptide residues or between lipid head-groups and peptide residues, we computed the radial distribution function $g_{AB}(r)$ between two groups of atoms A and B, selected based on chemical intuition.

$$g_{AB}(r) = \frac{1}{N_A\, N_B} \sum_{i=1}^{N_A} \sum_{j=1}^{N_B} \left\langle \delta\big(|\mathbf{r}_i - \mathbf{r}_j| - r\big) \right\rangle, \tag{2.42}$$

where:

- N_A and N_B are the number of atoms (or groups) in sets A and B, respectively,
- $\mathbf{r}_i$ and $\mathbf{r}_j$ are their instantaneous position vectors,
- $\langle \cdot \rangle$ denotes time averaging over trajectory frames,
- The normalization ensures $g_{AB}(r) \to 1$ at large r in a homogeneous system.

To quantify interaction distances:

- We identified the first peak in $g_{AB}(r)$, corresponding to the most probable interaction distance.
- We selected the first minimum immediately following that peak as the cutoff distance r_{cut}.

Using r_{cut}, interaction events were counted across the trajectory:

$$\langle n_{\text{int}} \rangle = \frac{1}{N_A \cdot N_{\text{frames}}} \sum_{\text{frames}} \sum_{i \in A} \sum_{j \in B} \Theta\big(r_{\text{cut}} - r_{ij}\big), \tag{2.43}$$

with the function $\Theta\big(r_{\text{cut}} - r_{ij}\big)$ operating as follows:

$$\Theta\big(r_{\text{cut}} - r_{ij}\big) = \begin{cases} 1, & r_{ij} \leq r_{\text{cut}}, \\ 0, & r_{ij} > r_{\text{cut}}. \end{cases}$$

where, N_{frames} is the total number of frames or snapshots and $r_{ij} = |\mathbf{r}_i - \mathbf{r}_j|$.

This yields the average number of interactions between reference atoms/groups across the trajectory. Employing the first minimum after the initial RDF peak ensures an empirically grounded, chemically relevant cutoff for defining interactions.

2.3.6 Membrane Thickness and Lipid Order Parameter Calculations

2.3.6.1 Membrane Thickness: `thickness.py`

GROMACS does not include a native tool for calculating bilayer thickness. Existing tools such as GridMAT-MD [41] can perform this analysis but operate on a single CPU core, becoming prohibitively slow for large trajectories, such as those from simulations of nanodiscs.

To overcome this limitation, we developed a Python script that leverages `numpy` for efficient matrix handling and the Python `multiprocessing` module to utilize all available logical CPU cores. This parallelized implementation runs approximately ten times faster than GridMAT-MD for long trajectories.

We define the bilayer thickness as the minimal distance along the membrane normal between pairs of phosphate headgroup atoms in opposing leaflets. For each frame:

1. Identify headgroup pairs and record the minimal distance and their corresponding (x,y) coordinates. 2. Bin these data into a two-dimensional grid subdivided by the simulation box in the xy-plane, treating top and bottom leaflets separately. 3. Compute the average thickness for each grid cell by combining data from both leaflets.

This approach yields a spatial thickness map of the nanodisc at high temporal resolution and with minimal computational cost.

2.3.6.2 Lipid Chain Order Parameter: `order.py`

GROMACS provides the tool `gmx order` [36] to compute lipid tail order parameters (S_{CH}), but it is inherently single-threaded and becomes inefficient when processing large lipid systems or long simulations.

We addressed this by developing a parallel Python script using `numpy` and `multiprocessing`, achieving a tenfold speedup over `gmx order`.

The lipid tail order parameter was calculated using:

$$S_{CH} = \frac{1}{2} \left\langle 3 \cos^2 \theta - 1 \right\rangle, \tag{2.44}$$

where θ is the angle between the C-H bond and the bilayer normal. The S_{CH} values were computed over all trajectories for each lipid and each carbon along both lipid tails [42, 43]. These values were then averaged across the two tails and binned onto a grid. An additional average was calculated over all frames and lipids within each bin.

Both scripts (`thickness.py` and `order.py`) implement scientifically established measurement definitions while significantly improving computational throughput. By parallelizing across CPU cores and vectorizing calculations, they deliver fast, scalable analysis of membrane structure in the simulations.

2.3.7 Calculation of ssNMR Parameters: ^{15}N-Chemical shift.py and ^{2}H Splitting.py

We computed the ^{2}H-NMR quadrupole splitting of the $C_\alpha - C_\beta$-H_3 and the ^{15}N chemical shifts for the labeled residues, following the same procedures used experimentally [43–45]. These quantities inform the orientation of the peptides relative to the nanodisc bilayer.

For a fair comparison between experimental and MD simulation values, we calculated the experimental-like ^{2}H quadrupole splitting corresponding to the orientation of the C_α-C_β bonds in the selected residues (labeled residues) with respect to the membrane normal (Fig.2.6A). In the experiments, the nanodisc normal is aligned parallel to the external magnetic field; accordingly, in our simulations, we oriented the nanodisc normal along the z-axis.

The static quadrupole splitting ($|\langle \Delta\nu_Q \rangle|$) for each residue at a particular trajectory snapshot is calculated as:

$$|\langle \Delta\nu_Q \rangle| = \frac{3}{2}\,(e^{2qQ})/h \;\cdot\; \frac{3\cos^2\theta - 1}{2} \tag{2.45}$$

where θ is the angle between the C_α-C_β bond and the hypothetical magnetic field taken as z axis, and $(e^2qQ)/h$ is the static quadrupole coupling constant.

Additionally, we calculated the ^{15}N chemical shift [46], following the experimental methodology. This chemical shift depends directly on the orientation of its tensor eigenvectors relative to the external magnetic field. The eigenvector $\vec{\sigma}33$ is oriented approximately 16° from the N–H bond toward the N–C bond, lying in the peptide plane. The eigenvector $\vec{\sigma}11$ is perpendicular to $\vec{\sigma}33$, also within the peptide plane, while $\vec{\sigma}22$ is orthogonal to both, thus perpendicular to the peptide plane. All vectors originate from the nitrogen atom (Fig.2.6B).

Defining the Euler angles Φ, Θ, and Ψ to transform from the eigenvector reference frame to the laboratory frame (z axis), the chemical shift component $\vec{\sigma}_{zz}$ can be calculated as:

$$\sigma_{zz} = \sigma_{11}\sin^2\Theta cos^2\Phi + \sigma_{22}\sin^2\Theta sin^2\Phi + \sigma_{33} cos^2\Theta \tag{2.46}$$

where σzz is the ^{15}N chemical shift aligned with the membrane normal, and the eigenvalues of the chemical shift tensor σ_{11}, σ_{22}, and σ_{33} are respectively taken as 56 ppm, 81 ppm, and 223 ppm, as used in experimental NMR studies[32]. Because MD simulations take discrete snapshots at finite time intervals, the raw distributions of both the static quadrupole splittings ($\Delta\nu_Q$) and the ^{15}N chemical shifts (σ_{zz}) are intrinsically discontinuous. We therefore applied the kernel density estimation (KDE) implementation from scikit-learn [47] to obtain smooth, continuous approx-

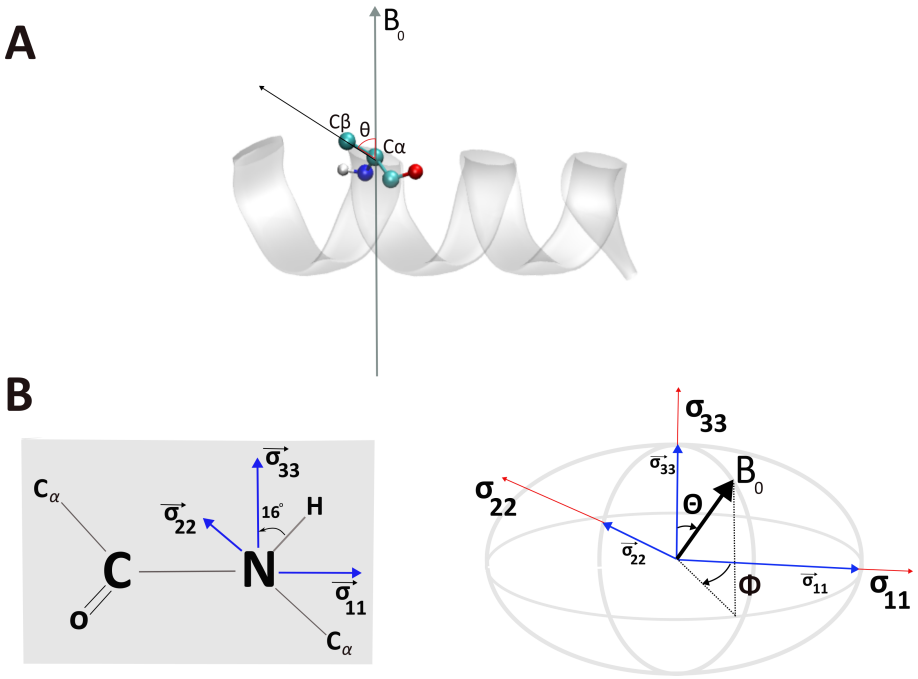

Figure 2.6: Pictorial representation of the method used to compute ^{2}H quadrupolar splitting and ^{15}N chemical-shift anisotropy (CSA). **(A)** The ^{2}H splitting is obtained from the angle θ between the $C_\alpha - C_\beta$ bond vector and the magnetic-field direction $\mathbf{B}_0$. **(B)** The ^{15}N CSA tensor is shown in its principal-axis system placed next to the molecular frame of the peptide-bond. ^{15}N chemical shift is obtained by determining the polar (Θ) and azimuthal (Φ) angles of $\mathbf{B}_0$ within the molecular frame relative to the principal axes of the CSA tensor. Axes $\vec{\sigma}_{11}$ and $\vec{\sigma}_{33}$ lie in the peptide plane within the plane of the paper, while $\vec{\sigma}_{22}$ is perpendicular to it. Θ is measured between $\vec{\sigma}_{33}$ and $\mathbf{B}_0$, and Φ is measured between the $\vec{\sigma}_{11}$ and the projection of $\mathbf{B}_0$.

imations of these probability distributions. The mean (μ) and standard deviation (σ) were then computed from the KDE-derived profiles for direct comparison with experimental values.

2.3.8 Small Angle X-ray Scattering (SAXS)

SAXS is widely used to probe the structure of biomolecules in solution [48, 49]. In this work, we do not detail the experimental setup—which is outside the scope of the thesis—but focus instead on the preliminary data analysis that is essential for calculating global parameters such as the radius of gyration (R_g), the maximum particle dimension (D_{max}), and signs of aggregation. Accurate interpretation of SAXS curves also requires reliable prediction of scattering from structural models, which is non-trivial. Because SAXS is a contrast method, the scattering from solvent displaced by the solute must be accounted for and subtracted. Moreover, the hydration layer surrounding biomolecules contributes appreciably to the signal; its electron density is typically higher than that of bulk solvent, thereby increasing the apparent R_g. Thermal fluctuations and internal motions further modulate the scattering, especially toward wider angles.

Biomolecules in solution are free to diffuse and rotate within the buffer. Under these conditions, the measured scattering intensity represents a time- and ensemble-averaged signal over all particle orientations and conformations. The scattering from the system can therefore be expressed as

$$I(q) = \left\langle \int_v \gamma(r) e^{-iqr} dr \right\rangle_\Omega = 4\pi \int \gamma(r) r^2 \frac{\sin(qr)}{qr} dr = 4\pi \int P(r) \frac{\sin(qr)}{qr} dr, \quad (2.47)$$

where $\gamma(r)$ denotes the autocorrelation function of the scattering length density, and $P(r)$ is the real-space pair distance distribution function (PDDF).

In the absence of interparticle interactions, the scattering from the sample can be written as the incoherent sum of contributions from all identical particles:

$$I(q) = n \cdot I_{\text{particle}}(q) = n \int_0^{D_{\max}} P(r) \frac{\sin(qr)}{qr} dr \quad (2.48)$$

where n is the number of particles in solution, and $D_{\max}$ is the maximum intraparticle dimension. The function $P(r)$ contains the structural information of the particle, encoding the distribution of all interatomic distances within the scattering object.

2.3.8.1 Model free analysis

Model-free analysis methods are commonly used for the initial assessment of SAXS datasets. They provide a quick quality check of the scattering curve and allow the extraction of key size parameters, most notably the radius of gyration and the maximum particle dimension for the particles present in solution.

2.3.8.2 Guinier analysis

The first type of model-free analysis is the Guinier approximation proposed by Guinier in 1939 [50]. This approximation is made by expanding the $sin(qr)$ term in equation: 2.47 into a Taylor series:

$$\begin{aligned} I(q) &= \int_0^{D_{\max}} P(r)\,\frac{\sin(qr)}{qr}\,dr = \int_0^{D_{\max}} P(r)\left(1-\frac{(qr)^2}{6}+\cdots\right)dr \\ &= \int_0^{D_{\max}} P(r)\,dr - \frac{q^2}{6}\int_0^{D_{\max}} P(r)\,r^2\,dr + \cdots \\ &= I(0) - \frac{q^2}{3}\,I(0)\,\frac{\displaystyle\int_0^{D_{\max}} P(r)\,r^2\,dr}{\displaystyle 2\int_0^{D_{\max}} P(r)\,dr} + \cdots \\ &\approx I(0)\left(1-\frac{q^2R_g^2}{3}\right), \end{aligned} \tag{2.49}$$

The forward scattering is

$$I(0) = \int_0^{D_{\max}} P(r)\,dr.$$

The final approximation is valid in the Guinier regime, i.e., for a small $q^2R_g^2$ value (typically $q^2R_g^2 \leq 1.3$), where higher-order terms are negligible. Equivalently, the expression above corresponds to the first two terms of the Taylor expansion of an exponential, yielding

$$I(q) \;\approx\; I(0)\,\exp\left(-\frac{q^2R_g^2}{3}\right). \tag{2.50}$$

Owing to the exponential form of the Guinier equation 3.3, both R_g and I(0) can be determined by performing a linear fit of lnI(q) versus q^2, a representation commonly referred to as the Guinier plot. The range of data points used for this linear fit defines the Guinier region.

The Guinier analysis serves two main purposes. First, it provides the parameters R_g and I(0). The radius of gyration reflects the particle's overall size, while I(0) is proportional to the product of the molecular weight and the concentration. These

quantities not only serve as fundamental descriptors of the system under study, but also act as inputs for further SAXS-based determinations, such as molecular weight and excluded volume.

Second, and equally important, the Guinier fit is one of the most reliable means of assessing SAXS data quality. Deviations from linearity in the Guinier region often indicate experimental issues such as aggregation, radiation damage, interparticle interactions, or—in some cases—imperfect buffer subtraction [48]. A well-defined linear Guinier region strongly suggests that the data originate from a monodisperse, artifact-free sample. Conversely, if a satisfactory linear fit cannot be obtained, or if substantial portions of the low-q region must be excluded to achieve linearity, the data are likely compromised by one or more of the aforementioned problems and may not be suitable for further quantitative analysis.

2.3.8.3 Indirect Fourier Transform Method

When examining equation 2.47, it may seem straightforward to obtain the pair distance distribution function $P(r)$ by directly applying a Fourier transform to the measured scattering data. In principle, this would be correct; however, such an approach requires experimental data covering the full scattering range from $q = 0$ to $q = \infty$. In practice, this is not possible. At very low scattering angles, the beam stop prevents access to the forward scattering region, while at high scattering angles, the scattering signal becomes indistinguishable from the instrumental background.

To overcome these limitations, Glatter [51] proposed in 1977 the method of *indirect Fourier transformation (IFT)*. Instead of attempting a direct Fourier transform, one defines a trial $P(r)$ function and evaluates how well it reproduces the measured scattering curve. This is an ill-posed problem, since many different $P(r)$ functions can fit the data equally well. To make the solution unique and physically meaningful, two constraints are imposed:

1. **Finite support** — the maximum dimension of the particle, $D_{\max}$, is assumed to be finite, such that $P(r) = 0$ for $r > D_{\max}$.
2. **Smoothness** — the $P(r)$ function must vary smoothly, which is justified by the finite resolution of small-angle scattering experiments.

With these constraints, the problem becomes well-defined. The $P(r)$ function is represented as a sum of cubic B-splines, $\phi_i(r)$, equally spaced between $r = 0$ and $r = D_{\max}$, and weighted by coefficients c_i:

$$P(r) = \sum_{i=1}^{k} c_i \, \phi_i(r). \tag{2.51}$$

The corresponding scattering curve is obtained by substituting into equation 3.19, yielding:

$$I_m(q) = \sum_{i=1}^{k} c_i \, \phi_i(q), \tag{2.52}$$

where $\phi_i(q)$ are the Fourier transforms of the spline basis functions. The best-fitting $P(r)$ is then found by minimizing a target function consisting of two terms:

$$Q = \chi^2 + \alpha N_c, \tag{2.53}$$

where χ^2 measures the agreement between the experimental data and the model curve, while N_c quantifies the smoothness of $P(r)$. The parameter α is a Lagrange multiplier that balances the relative weight between data fitting and smoothness.

To perform the IFT analysis, three inputs are required: $D_{\max}$, the number of spline functions k, and the regularization parameter α. Typically, $D_{\max}$ can be estimated from prior knowledge of the system. The number of splines must be sufficient to allow a smooth $P(r)$ across the full range from 0 to $D_{\max}$. The optimal α is chosen using the *point of inflection criterion*: as α increases, χ^2 remains relatively stable until a critical point where it begins to rise sharply. This point, identified by a change in the sign of the second derivative of χ^2, provides the best compromise between smoothness and fidelity to the data.

Thus, the constraints imposed on $P(r)$ finite size and smoothness ensure that the IFT method yields the smoothest physically meaningful solution consistent with the scattering data.

IFT provides the pair distance distribution function $P(r)$, which describes the probability of finding intraparticle distances. From $P(r)$, one can obtain the radius of gyration R_g, the forward scattering intensity $I(0)$, and the maximum particle dimension $D_{\max}$. IFT also acts as a quality check, since a smooth $P(r)$ that decays to zero at $D_{\max}$ indicates reliable scattering data. Thus, IFT provides a model-independent method for extracting global structural parameters from SAXS curves.

Since Glatter introduced the indirect Fourier transform (IFT) method in 1977, many implementations and refinements have followed, including statistical procedures for estimating the maximum particle distance and the Lagrange multiplier. In this work, we use **GNOM** to analyze the SAXS curves, both for its robustness and to align with the analysis workflow used by our experimental collaborators. **GNOM**, part of the widely used `ATSAS` suite (Svergun group, EMBL Hamburg) [47], performs IFT to obtain the real-space pair-distance distribution $P(r)$. It provides reliable estimates of key global parameters—including the maximum particle dimension $D_{\max}$, the radius of gyration R_g, and the forward scattering $I(0)$—and employs smoothness regularization to stabilize the inversion from reciprocal space.

2.3.9 Small Angle X-ray Scattering from All-Atomic MD simulation:

Several computational methods are available for predicting SAXS/SWAXS curves from structural models, including CRYSOL [52], FoXS [53], AquaSAXS [54], Pepsi-SAXS [55], and SASTBX [56]. However, these approaches rely on multiple fitting parameters to match predicted curves with experimental data. Most commonly, a fitting parameter is introduced to account for the hydration layer density, while additional parameters for displaced solvent or buffer subtraction vary between methods. Although such fitting procedures can produce good agreement with experiments, they reduce the amount of structural information that can be extracted and may introduce overfitting [57]. Moreover, thermal fluctuations are difficult to capture with these implicit approaches.

In this work, we employ the GROMACS-SWAXS method [58], which uses explicit-solvent all-atom MD trajectories to predict SAXS curves. A key advantage of this approach is that MD simulations naturally reproduce the increase in radius of gyration caused by the hydration shell, providing a physically accurate model of hydration [59]. Consequently, SAXS curves computed from MD simulations do not require fitting of the hydration shell, thereby avoiding artificial modifications of the radius of gyration. Likewise, when scattering from excluded solvent is calculated using explicit water rather than dummy atoms (as in implicit-solvent methods), no scaling parameters are required. Finally, MD simulations inherently account for thermal fluctuations, offering a more realistic prediction of SAXS data. Importantly, the more realistic back-calculated SAXS curves resulting from MD simulations provide an opportunity for direct comparison with experimental data, including the radius of gyration that can be directly related to the structural model.

By leveraging explicit solvent all-atom molecular dynamics simulations, we can provide a more detailed interpretation of the SAXS data. The physicochemical information embedded in the MD force field complements the SAXS data, enhancing the overall understanding of the system. This combination of theoretical and experimental data allows for a more accurate representation of the nanodisc's structure and dynamics in solution, overcoming the limitations of SAXS data interpretation.

2.3.9.1 GROMACS-SWAXS software details

We used GROMACS-SWAXS to calculate theoretical SAXS [58] curves from the MD simulation data, allowing us to compare these with experimental SAXS curves and gain structural information about the nanodiscs in solution. This approach was chosen due to the inherent challenges in interpreting experimental SAXS data, which often have low information content and include scattering contributions from the solvent.

To calculate the $I(q)$, two scattering intensities are typically measured, that is, the

scattering intensity of the solution$I_A(q)$, and the intensity of the pure solvent $I_B(q)$. then subtracting each other to get the $I(q)$ is the scattering intensity of the solute present in the solution.

$$I(q) = I_A(q) - I_B(q) \tag{2.54}$$

$$I_a(q) = \langle |A(q)^2| \rangle \tag{2.55}$$

$$I_b(q) = \langle |B(q)^2| \rangle \tag{2.56}$$

where $< .... >$ denotes the ensemble average over all solute and solvent degrees of freedom, $A(q)$ and $B(q)$ are the Fourier transforms of the instantaneous electron densities of the solution and the pure solvent.

2.3.9.2 Atomic form factors

The equations below are used to calculate the scattering amplitude for an individual simulation frame.

$$A(q) = \sum_{j=1}^{N_a} f_j(q) e^{-iq.r_j} \tag{2.57}$$

$$B(q) = \sum_{j=1}^{N_b} f_j(q) e^{-iq.r_j} \tag{2.58}$$

where N_A is the number of atoms $f_j(q)$ is atomic form factor, and r_j is the coordinate of atom j. The form factors are well approximated as follows;

$$f_j(q) = \sum_{k=1}^{4} a_k . e^{-b_k . (q/4\pi)^2} + c \tag{2.59}$$

where a_k, b_k, c are Cromer-Mann parameter which are published in the tables in [60]. These X-ray scattering factors are computed from a numerical Hartree-Fock wave function.

2.3.9.3 Fitting procedure

The theoretical SAXS intensity was computed directly from the MD-derived atomic structure and its explicit hydration shell [58]; no empirical adjustments of shell contrast or excluded volume were introduced. Consequently, fitting to the experimental profile employed a single global scaling factor c.

Given the experimental profile $I_{\mathrm{exp}}(q)$ and the theoretical profile $I_{\mathrm{theor}}(q)$, the optimal scale c was obtained by minimizing the chi-squared (goodness of the fit),

$$\chi^2 = \frac{1}{N-1} \sum_j \left[\frac{I_{\mathrm{exp}}(q_j) - c\, I_{\mathrm{theor}}(q_j)}{\sigma(q_j)} \right]^2, \tag{2.60}$$

where N is the number of data points and $\sigma(q_j)$ is the experimental uncertainty at q_j.

The scale factor c has the analytic solution [52]:

$$c = \frac{\sum_j \dfrac{I_{\mathrm{exp}}(q_j)\, I_{\mathrm{theor}}(q_j)}{\sigma(q_j)^2}}{\sum_j \dfrac{I_{\mathrm{theor}}(q_j)^2}{\sigma(q_j)^2}}. \tag{2.61}$$

When pointwise uncertainties were not available, they were estimated as a fixed fraction of the intensity:

$$\sigma(q) = 0.01 \times I_{\mathrm{exp}}(q). \tag{2.62}$$

No additional free parameters (e.g., hydration-shell contrast or excluded-volume scaling) were used, ensuring that agreement between theory and experiment reflects the physical realism of the MD model rather than empirical tuning.

References

[1] Daan Frenkel and Berend Smit. *Understanding molecular simulation: from algorithms to applications*. Elsevier, 2023.

[2] John C Tully. Perspective on "zur quantentheorie der molekeln" born m, oppenheimer r (1927) ann phys 84: 457. *Theoretical chemistry accounts*, 103(3): 173–176, 2000.

[3] István Mayer. *Simple theorems, proofs, and derivations in quantum chemistry*. Springer Science & Business Media, 2003.

[4] Martin Karplus and J Andrew McCammon. Molecular dynamics simulations of biomolecules. *Nature structural biology*, 9(9):646–652, 2002.

[5] Wendy D Cornell, Piotr Cieplak, Christopher I Bayly, Ian R Gould, Kenneth M Merz, David M Ferguson, David C Spellmeyer, Thomas Fox, James W Caldwell, and Peter A Kollman. A second generation force field for the simulation of proteins, nucleic acids, and organic molecules. *Journal of the American Chemical Society*, 117(19):5179–5197, 1995.

[6] Alex D MacKerell Jr, Donald Bashford, MLDR Bellott, Roland Leslie Dunbrack Jr, Jeffrey D Evanseck, Martin J Field, Stefan Fischer, Jiali Gao, Houyang Guo, Sookhee Ha, et al. All-atom empirical potential for molecular modeling and dynamics studies of proteins. *The journal of physical chemistry B*, 102(18): 3586–3616, 1998.

[7] William L Jorgensen, David S Maxwell, and Julian Tirado-Rives. Development and testing of the opls all-atom force field on conformational energetics and properties of organic liquids. *Journal of the american chemical society*, 118 (45):11225–11236, 1996.

[8] Anne M Brown and Justin A Lemkul. Robustness in biomolecular simulations: Addressing challenges in data generation, analysis, and curation. *Cell Reports Physical Science*, 6(5), 2025.

[9] Mark E. Tuckerman. *Statistical Mechanics: Theory and Molecular Simulation*. Oxford University Press, Oxford, 2023. doi: 10.1093/oso/9780198825562.001.0001.

[10] Loup Verlet. Computer" experiments" on classical fluids. i. thermodynamical properties of lennard-jones molecules. *Physical review*, 159(1):98, 1967.

[11] William C Swope, Hans C Andersen, Peter H Berens, and Kent R Wilson. A computer simulation method for the calculation of equilibrium constants for the formation of physical clusters of molecules: Application to small water clusters. *The Journal of chemical physics*, 76(1):637–649, 1982.

[12] Jean-Paul Ryckaert, Giovanni Ciccotti, and Herman JC Berendsen. Numerical integration of the cartesian equations of motion of a system with constraints: molecular dynamics of n-alkanes. *Journal of computational physics*, 23(3):327–341, 1977.

[13] Hans C Andersen. Rattle: A "velocity" version of the shake algorithm for molecular dynamics calculations. *Journal of computational Physics*, 52(1):24–34, 1983.

[14] Berk Hess, Henk Bekker, Herman JC Berendsen, and Johannes GEM Fraaije. Lincs: A linear constraint solver for molecular simulations. *Journal of computational chemistry*, 18(12):1463–1472, 1997.

[15] Shuichi Miyamoto and Peter A Kollman. Settle: An analytical version of the shake and rattle algorithm for rigid water models. *Journal of computational chemistry*, 13(8):952–962, 1992.

[16] Mark James Abraham, Teemu Murtola, Roland Schulz, Szilárd Páll, Jeremy C Smith, Berk Hess, and Erik Lindahl. Gromacs: High performance molecular simulations through multi-level parallelism from laptops to supercomputers. *SoftwareX*, 1:19–25, 2015.

[17] Chris Oostenbrink, Alessandra Villa, Alan E Mark, and Wilfred F Van Gunsteren. A biomolecular force field based on the free enthalpy of hydration and solvation: the gromos force-field parameter sets 53a5 and 53a6. *Journal of computational chemistry*, 25(13):1656–1676, 2004.

[18] Jing Huang, Sarah Rauscher, Grzegorz Nawrocki, Ting Ran, Michael Feig, Bert L De Groot, Helmut Grubmüller, and Alexander D MacKerell Jr. Charmm36m: an improved force field for folded and intrinsically disordered proteins. *Nature methods*, 14(1):71–73, 2017.

[19] Simon W de Leeuw, John William Perram, and Edgar Roderick Smith. Simulation of electrostatic systems in periodic boundary conditions. i. lattice sums and dielectric constants. *Proceedings of the Royal Society of London. A. Mathematical and Physical Sciences*, 373(1752):27–56, 1980.

[20] Tom Darden, Darrin York, Lee Pedersen, et al. Particle mesh ewald: An n log (n) method for ewald sums in large systems. *Journal of chemical physics*, 98: 10089–10089, 1993.

[21] Hans C Andersen. Molecular dynamics simulations at constant pressure and/or temperature. *The Journal of chemical physics*, 72(4):2384–2393, 1980.

[22] Herman JC Berendsen, JPM van Postma, Wilfred F Van Gunsteren, ARHJ DiNola, and Jan R Haak. Molecular dynamics with coupling to an external bath. *The Journal of chemical physics*, 81(8):3684–3690, 1984.

[23] Giovanni Bussi, Davide Donadio, and Michele Parrinello. Canonical sampling through velocity rescaling. *The Journal of chemical physics*, 126(1), 2007.

[24] Denis J Evans and Brad Lee Holian. The nose-hoover thermostat. *Journal of Chemical Physics*, 83(8):4069–4074, 1985.

[25] Shuichi Nosé and Michael L Klein. Constant pressure molecular dynamics for molecular systems. *Molecular Physics*, 50(5):1055–1076, 1983.

[26] Anna Wolska, Mart Reimund, Denis O Sviridov, Marcelo J Amar, and Alan T Remaley. Apolipoprotein mimetic peptides: potential new therapies for cardiovascular diseases. *Cells*, 10(3):597, 2021.

[27] Vinod K Mishra, GM Anantharamaiah, Jere P Segrest, Mayakonda N Palgunachari, Manjula Chaddha, SW Simon Sham, and N Rama Krishna. Association of a model class a (apolipoprotein) amphipathic α helical peptide with lipid: High resolution nmr studies of peptide· lipid discoidal complexes. *Journal of Biological Chemistry*, 281(10):6511–6519, 2006.

[28] Vinod K Mishra, Mayakonda N Palgunachari, N Rama Krishna, John Glushka, Jere P Segrest, and GM Anantharamaiah. Effect of leucine to phenylalanine substitution on the nonpolar face of a class a amphipathic helical peptide on its interaction with lipid: high resolution solution nmr studies of 4f-dimyristoylphosphatidylcholine discoidal complex. *Journal of Biological Chemistry*, 283(49):34393–34402, 2008.

[29] GM Anantharamaiah, JL Jones, CG Brouillette, CF Schmidt, BYUNG HONG Chung, TA Hughes, AuS Bhown, and JP Segrest. Studies of synthetic peptide analogs of the amphipathic helix. structure of complexes with dimyristoyl phosphatidylcholine. *Journal of Biological Chemistry*, 260(18):10248–10255, 1985.

[30] LeAnne T Bloedon, Richard Dunbar, Danielle Duffy, Paula Pinell-Salles, Robert Norris, Bruce J DeGroot, Rajesh Movva, Mohamad Navab, Alan M Fogelman, and Daniel J Rader. Safety, pharmacokinetics, and pharmacodynamics of oral apoa-i mimetic peptide d-4f in high-risk cardiovascular patients. *Journal of lipid research*, 49(6):1344–1352, 2008.

[31] Alankrita Rani, Denys Balandin, Rohith Ravi, Julia Teppan, Ivan Vidakovic, Melanie Kienzl, Thomas Bärnthaler, Michael Holzer, Lamija Zijadic, Akos Heinemann, et al. Peptide-based lipid nanodiscs suppress eosinophil recruitment and chemotaxis. *Journal of Controlled Release*, page 114060, 2025.

[32] Evgeniy S Salnikov, GM Anantharamaiah, and Burkhard Bechinger. Supramolecular organization of apolipoprotein-ai-derived peptides within disc-like arrangements. *Biophysical journal*, 115(3):467–477, 2018.

[33] Julien Rey, Samuel Murail, Sjoerd de Vries, Philippe Derreumaux, and Pierre Tuffery. Pep-fold4: A ph-dependent force field for peptide structure prediction in aqueous solution. *Nucleic acids research*, 51(W1):W432–W437, 2023.

[34] Yifei Qi, Jumin Lee, Jeffery B Klauda, and Wonpil Im. Charmm-gui nanodisc builder for modeling and simulation of various nanodisc systems. *Journal of computational chemistry*, 40(7):893–899, 2019.

[35] Leandro Martínez, Ricardo Andrade, Ernesto G Birgin, and José Mario Martínez. Packmol: A package for building initial configurations for molecular dynamics simulations. *Journal of computational chemistry*, 30(13):2157–2164, 2009.

[36] Sander Pronk, Szilárd Páll, Roland Schulz, Per Larsson, Pär Bjelkmar, Rossen Apostolov, Michael R Shirts, Jeremy C Smith, Peter M Kasson, David Van Der Spoel, et al. Gromacs 4.5: a high-throughput and highly parallel open source molecular simulation toolkit. *Bioinformatics*, 29(7):845–854, 2013.

[37] Chad W Hopkins, Scott Le Grand, Ross C Walker, and Adrian E Roitberg. Long-time-step molecular dynamics through hydrogen mass repartitioning. *Journal of chemical theory and computation*, 11(4):1864–1874, 2015.

[38] Michele Parrinello and Aneesur Rahman. Polymorphic transitions in single crystals: A new molecular dynamics method. *Journal of Applied physics*, 52 (12):7182–7190, 1981.

[39] Naveen Michaud-Agrawal, Elizabeth J Denning, Thomas B Woolf, and Oliver Beckstein. Mdanalysis: a toolkit for the analysis of molecular dynamics simulations. *Journal of computational chemistry*, 32(10):2319–2327, 2011.

[40] Wolfgang Kabsch and Christian Sander. Dictionary of protein secondary structure: pattern recognition of hydrogen-bonded and geometrical features. *Biopolymers: Original Research on Biomolecules*, 22(12):2577–2637, 1983.

[41] William J Allen, Justin A Lemkul, and David R Bevan. Gridmat-md: a grid-based membrane analysis tool for use with molecular dynamics. *Journal of computational chemistry*, 30(12):1952–1958, 2009.

[42] Egbert Egberts, Siewert-Jan Marrink, and Herman JC Berendsen. Molecular dynamics simulation of a phospholipid membrane. *European biophysics journal*, 22(6):423–436, 1994.

[43] Trivikram R Molugu, Soohyun Lee, and Michael F Brown. Concepts and methods of solid-state nmr spectroscopy applied to biomembranes. *Chemical reviews*, 117(19):12087–12132, 2017.

[44] Christopher Aisenbrey and Burkhard Bechinger. Investigations of polypeptide rotational diffusion in aligned membranes by 2h and 15n solid-state nmr spectroscopy. *Journal of the American Chemical Society*, 126(50):16676–16683, 2004.

[45] Burkhard Bechinger and Evgeniy S Salnikov. The membrane interactions of antimicrobial peptides revealed by solid-state nmr spectroscopy. *Chemistry and physics of lipids*, 165(3):282–301, 2012.

[46] Burkhard Bechinger and Christina Sizun. Alignment and structural analysis of membrane polypeptides by 15n and 31p solid-state nmr spectroscopy. *Concepts in Magnetic Resonance Part A: An Educational Journal*, 18(2):130–145, 2003.

[47] Fabian Pedregosa, Gaël Varoquaux, Alexandre Gramfort, Vincent Michel, Bertrand Thirion, Olivier Grisel, Mathieu Blondel, Peter Prettenhofer, Ron Weiss, Vincent Dubourg, et al. Scikit-learn: Machine learning in python. *the Journal of machine Learning research*, 12:2825–2830, 2011.

[48] Christopher D Putnam, Michal Hammel, Greg L Hura, and John A Tainer. X-ray solution scattering (saxs) combined with crystallography and computation: defining accurate macromolecular structures, conformations and assemblies in solution. *Quarterly reviews of biophysics*, 40(3):191–285, 2007.

[49] Melissa A Graewert and Dmitri I Svergun. Impact and progress in small and wide angle x-ray scattering (saxs and waxs). *Current opinion in structural biology*, 23(5):748–754, 2013.

[50] André Guinier. La diffraction des rayons x aux tres petits angles: applications a l'etude de phenomenes ultramicroscopiques. In *Annales de physique*, number 11. Sér. 12, pages 161–237. EDP Sciences, 1939.

[51] OTTO Glatter. A new method for the evaluation of small-angle scattering data. *Applied Crystallography*, 10(5):415–421, 1977.

[52] DIBC Svergun, Claudio Barberato, and Michel HJ Koch. Crysol–a program to evaluate x-ray solution scattering of biological macromolecules from atomic coordinates. *Applied Crystallography*, 28(6):768–773, 1995.

[53] Dina Schneidman-Duhovny, Michal Hammel, and Andrej Sali. Foxs: a web server for rapid computation and fitting of saxs profiles. *Nucleic acids research*, 38(suppl_2):W540–W544, 2010.

[54] Frederic Poitevin, Henri Orland, Sebastian Doniach, Patrice Koehl, and Marc Delarue. Aquasaxs: a web server for computation and fitting of saxs profiles with non-uniformally hydrated atomic models. *Nucleic acids research*, 39 (suppl_2):W184–W189, 2011.

[55] Sergei Grudinin, Maria Garkavenko, and Andrei Kazennov. Pepsi-saxs: an adaptive method for rapid and accurate computation of small-angle x-ray scattering profiles. *Biological Crystallography*, 73(5):449–464, 2017.

[56] Haiguang Liu, Alexander Hexemer, and Peter H Zwart. The small angle scattering toolbox (sastbx): an open-source software for biomolecular small-angle scattering. *Applied Crystallography*, 45(3):587–593, 2012.

[57] Alexander Grishaev, Liang Guo, Thomas Irving, and Ad Bax. Improved fitting of solution x-ray scattering data to macromolecular structures and structural ensembles by explicit water modeling. *Journal of the American Chemical Society*, 132(44):15484–15486, 2010.

[58] Christopher J Knight and Jochen S Hub. Waxsis: a web server for the calculation of saxs/waxs curves based on explicit-solvent molecular dynamics. *Nucleic acids research*, 43(W1):W225–W230, 2015.

[59] Po-chia Chen and Jochen S Hub. Validating solution ensembles from molecular dynamics simulation by wide-angle x-ray scattering data. *Biophysical journal*, 107(2):435–447, 2014.

[60] Don T Cromer and Joseph B Mann. X-ray scattering factors computed from numerical hartree–fock wave functions. *Acta Crystallographica Section A: Crystal Physics, Diffraction, Theoretical and General Crystallography*, 24(2):321–324, 1968.

3 Results

In this chapter, we used MD simulations and complementary experiments from our collaborators to investigate how apoA-I mimetic peptides organize and stabilize discoidal lipid bilayers, and how that supramolecular architecture links to function. We study three scaffolds 14A, 4F, and the tandem 4F-P-4F around DMPC and benchmark simulation outputs directly against experimental data using Solid-State NMR (ssNMR) observables, small-angle X-ray scattering (SAXS) profiles, pair-distance distributions, and circular dichroism (CD) spectra. The primary goal is to validate the models and then use them to uncover the key interactions and physical principles that may govern nanodisc structure, dynamics, and stability.

The chapter is organized into three sections, and we address these questions as follows. In Section 3.1, we present our results concerning 14A/DMPC nanodisc structure, stability, and dynamics. In particular, we calculated NMR parameters, namely ^{15}N chemical shifts and ^{2}H quadrupolar splittings, from the trajectories and compared them with previous ssNMR measurements to quantify peptide orientation around the lipid bilayer, and we further characterized critical peptide–peptide interactions and peptide–lipid interactions responsible for nanodisc stability. In the following Section 3.2, we extend our investigation to 4F/DMPC and 4F-P-4F/DMPC nanodiscs. Lacking comprehensive local orientational restraints, we built models guided by our 14A-based nanodisc study and by previously reported NMR studies on related apoA-I mimetic peptides. To assess global size and shape, we computed SAXS profiles from MD snapshots and compared them with experimental data, constraining plausible disc sizes/morphologies and identifying sources of mismatch. Finally, in Section 3.3, in collaboration with biophysical and biomedical groups studying 4F-P-4F lipid nanodiscs, we found that 4F-P-4F remains α-helical in free and lipidated forms, forms stable peptide–lipid assemblies in aqueous solution, and shows calculated CD spectra consistent with experiment; MD identified key peptide–lipid contacts that confer stability and we attempted to provide structural relevance to the biological functionality, especially in terms of cholesterol efflux.

Note: *Throughout this chapter, a superscript * denotes experimental data.*

3.1 Molecular Dynamics Simulations of 14A Peptide–Lipid Complexes: Comparison to NMR

In the Introduction, we highlighted the importance of investigating apoA-I mimetic peptide–based nanodiscs from a structural perspective. Recently, our collaborator Salnikov et al. explored a shorter variant of the 18A peptide [1], termed 14A. The 18A peptide was shortened by removing one helical turn, simplifying synthesis and enabling stable isotope labeling for NMR investigations, while preserving the essential functional properties (sequence details are provided in Section: 2.2.1). In addition, substituting the tryptophan residue in 18A with tyrosine significantly reduced background signals in fluorescence spectroscopy when other polypeptides were incorporated into 14A–lipid nanodiscs.

Using solid-state NMR spectroscopy under conditions that promoted disc formation at higher peptide-to-lipid ratios, Salnikov et al [1] provided strong evidence that the peptides adopt an orientation parallel to the discoidal lipid patch and antiparallel with each other. Site-specific labeling further indicated that these peptides localize at the nanodisc rim and may form dimers in an antiparallel arrangement. Nevertheless, the atomistic details of how the amphipathic helices are arranged to stabilize the rim of the discoidal lipid patches remain unresolved.

In the first part of the results section, we investigated 14A peptide–based nanodiscs composed of DMPC stabilized by 14A peptides using all-atom molecular dynamics simulations. We considered the antiparallel orientation of the peptides around the nanodisc, informed by experimental data from our collaborators. We optimized the antiparallel arrangement based on the earlier speculation [1] that the peptide could stabilize as a dimer by aromatic interactions (Section: 5.1). The peptide-to-lipid ratio for each system was optimized using our protocol for nanodisc assembly (Section: 2.2).

MD Simulations were performed at 30 °C and 37 °C for two different nanodisc sizes (Table 3.1), and the resulting peptide orientations were compared with solid-state NMR data collected at 37 °C. This comparison allows us to assess how temperatures near and below the experimental condition, particularly in relation to the DMPC phase transition and peptide thermal fluctuations, influence peptide orientation, thereby helping to validate the accuracy and transferability of our simulation model.

3.1.1 Computational Details

Atomistic molecular dynamics simulations of apoA-I mimetic 14A/DMPC nanodiscs were built (section:2.2) and performed simulations according to a defined Simulation protocol (section:2.2.3). The initial antiparallel arrangement of the peptide was based on a 14A/DMPC ssNMR study by our collaborators (Fig. 4 in [1]) and the optimization of the initial configuration in section 5.1. This protocol ensured

reliable assembly and simulation of 14A/DMPC nanodiscs for in-depth analysis of their structure, dynamics, and stability. Additionally, a pure DMPC bilayer was simulated using the same simulation protocol, except employing an anisotropic NPT ensemble. Detailed parameters for each system are compiled in Table 3.1.

To characterize the major peptide-peptide interactions, we calculated the free energy profiles corresponding to the most probable intermolecular interactions involving tyrosines (Y7–Y7) and phenylalanines (F14–F14) aromatic rings independently, which stabilize the dimer, leading to a stable belt-like structure around the lipid bilayer patch. For each pairwise interaction, we computed the distance r between the centers of mass of the aromatic rings and the angle θ between their ring normal vectors. These two geometric parameters together define the relative orientation and proximity of the aromatic side chains, allowing classification of common π–π interaction motifs: *face-to-face stacking*, *parallel-displaced stacking*, and *T-stacking* (edge-to-face). Relative Gibbs free energy $\Delta G(r, \theta)$ was estimated through the Boltzmann distribution based on the resulting probability distribution $P(r, \theta)$:

$$\Delta G(r, \theta) = -k_B T \ln P(r, \theta) \tag{3.1}$$

where k_B is the Boltzmann constant (in kcal/(mol·K)) and T is the simulation temperature (310 K) in Kelvin.

System	No. of 14A Peptide	No. of DMPC	Total no. of atoms	Simulation length per-replica(ns)	Replicas	
					30°C	37°C
A	24	186	326485	1000	3	3
B	40	665	1447090	400	1	1
Pure DMPC bilayer	0	154	38948	500	1	1

Table 3.1: Simulation system details for MD studies of DMPC bilayer patches stabilized by 14A peptides. System A contains 24 peptides (12 dimers) and System B contains 40 peptides (20 dimers). For each system, we report the number of DMPC lipids, the total number of atoms, the simulation length per replica, and the number of replicas run at 30°C and 37°C. Here, "simulation length" refers to the production run only, without any positional restraints.

3.1.2 Priliminary Analysis

We began our analysis by evaluating the radius of gyration (R_g) as a preliminary measure of system equilibration. In all systems examined, R_g stabilized after approximately 200 ns (Fig. 3.1A, B). Although R_g alone does not conclusively confirm equilibration, it provides insight into the convergence of the nanodisc's overall dimensions. Additionally, we examined the time evolution of peptide secondary structure over the full 6.8 µs simulation period at 30°C and 37°C. This analysis showed that the α-helical content of the peptides remained consistently stable, with no notable fluctuations (Table 3.6).

To more accurately determine nanodisc diameters and the spatial positioning of peptides relative to lipid patches, we calculated mass density profiles (Fig. 3.8), and the average diameter for each system was reported in Table 3.6. Across all simulations, no peptide dissociation from the lipid patches was observed.

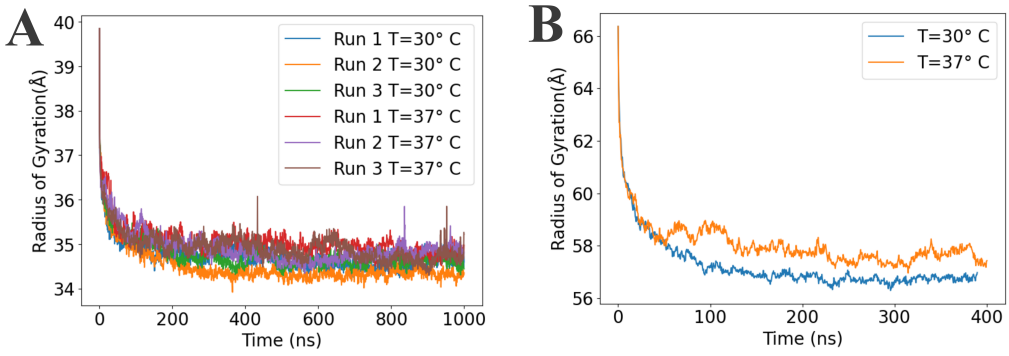

Figure 3.1: (A) Radius of gyration (Rg) for System A and its replicas at 30°C and 37°C, individually plotted over 1µs. System A comprises 24 (14A) peptides and 186 DMPC lipids. (B) Radius of gyration for System B at 30°C and 37°C, plotted over 400ns.

3.1.3 Validation of 14 Peptide Orientation with ssNMR Observation

To enable a fair comparison between our MD simulations and the ssNMR data for 14A peptides assembled around discoidal nanodisc bilayers [1], we computed ^{15}N chemical shifts for Ala5 and Leu10 and ^{2}H–NMR quadrupolar splittings for Ala5 and Ala13, matching the residues isotopically labeled in the experiments done by our collobrators [1]. These observables are orientation-sensitive: the ^{15}N chemical shifts primarily report on the orientations of the C–N and N–H bonds, whereas the ^{2}H quadrupolar splittings reflect the orientation of the C_α–C_β bond relative to the external field. Accordingly, these quantities depend on the peptide's azimuthal rotation and tilt relative to the bilayer normal. The computational protocol used to calculate these NMR parameters from the trajectories is described in Section 2.3.7.

The average chemical shifts and quadrupolar splittings obtained from the 14A/DMPC nanodisc simulations are summarized in the tables 3.3 and 3.4. The ^{2}H quadrupolar splittings exhibit consistent values across nanodiscs of varying sizes. In particular, the simulated quadrupolar splitting for Ala5 closely aligns with experimental observations.

However, a significant discrepancy is observed for Ala13. As a terminal residue, Ala13 likely experiences greater motional freedom in MD simulations, which may lead to excessive motional averaging and, consequently, an underestimation of the time-averaged ^{2}H splitting. In earlier ssNMR studies [2], a ^{2}H quadrupolar tensor

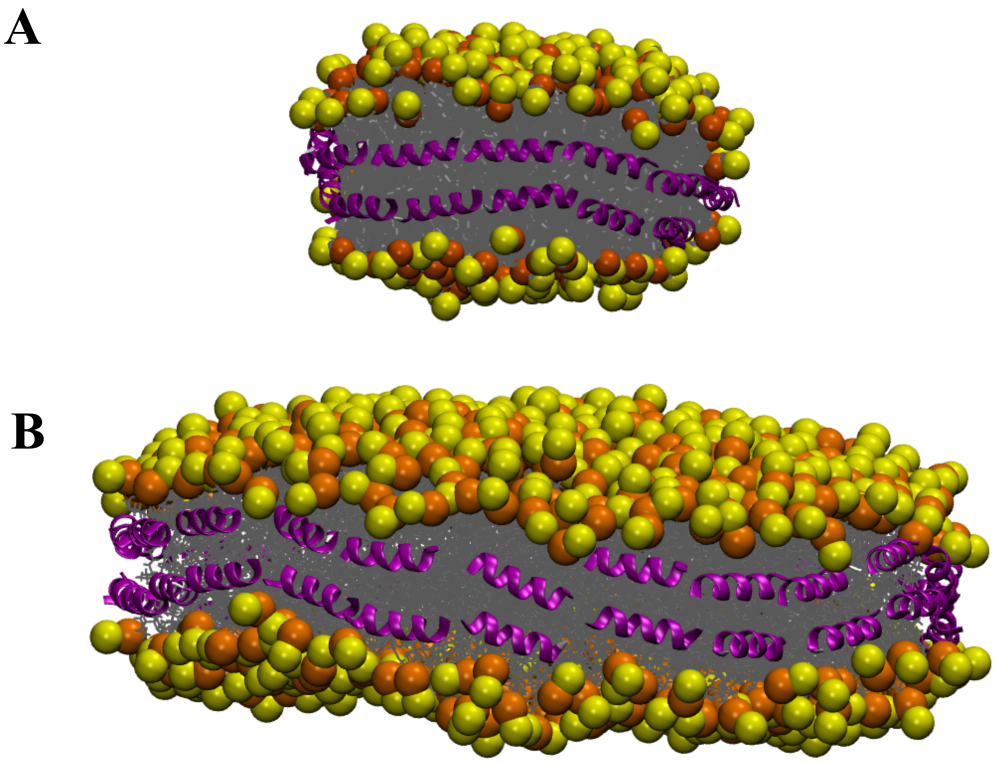

Figure 3.2: Pictorial representation of 14A/DMPC nanodiscs. (A) System A: final snapshot from a 1 μs MD trajectory at 37 ° C (Replica 1). (B) System B: final snapshot from a 400 ns MD trajectory at 37 ° C.

derived from ^{2}H-Ala–labeled peptide powder at room temperature—showing a maximum splitting of 74 kHz was used as a reference. While this serves as a reasonable baseline for examining dynamics in fluid-phase bilayers, MD simulations cannot disentangle the peptide's inherent mobility from membrane-induced fluctuations. To address this, we employed a full ^{2}H quadrupolar tensor value of 84 kHz for MD back-calculations. Although this adjustment slightly modifies the quantitative results, it does not resolve the discrepancy for Ala13.

As an alternative approach, we computed the splittings directly from the average bond angles of Ala5 and Ala13, using a 74 kHz prefactor [1], thereby neglecting membrane-induced motional averaging—similar to the experimental method. Based on mean angles of approximately 45° for Ala5 and 90° for Ala13, we obtained splittings of +18.5 kHz and -37 kHz, respectively. These values match the experimentally measured magnitudes.

Two experimental considerations are noteworthy. First, the sign of the ^{2}H splitting cannot be directly determined, so the angle–splitting relationship (Fig. 3.3) allows for multiple angle ranges to correspond to similar splitting magnitudes (see Table 3.2) when calculated with a 74 kHz prefactor. Second, typical experimental uncertainties are below 4 kHz, corresponding to angular uncertainties of less than 5°.

In contrast, MD simulations inherently provide the sign of the ^{2}H splitting by back-calculating from instantaneous molecular geometries. While this feature is beneficial, MD-derived averages are influenced by larger thermal fluctuations and shorter sampling timescales compared to the experiment. Despite these limitations, the well-characterized angular dependence of ^{2}H quadrupolar splitting and its strong sensitivity to the angle ϑ support the reliability of the angles derived from our trajectories. Consequently, the back-calculated ^{2}H splittings are fully consistent with the experimental data.

Residues	**Possible angle intervals (°)**	**Exp.value**
Ala5	(43 to 47), (64 to 79), (112 to 116), (133 to 137)	19.0 ± 4
Ala13	(35 to 38), (78 to 102), (143 to 147)	34.5 ± 2

Table 3.2: Experimental ^{2}H splitting values for Ala5 and Ala13 and the corresponding possible angle intervals derived from the splitting–vs–angle plot. Because the experimental sign of the splitting cannot be directly determined, all angle intervals that yield positive or negative splittings consistent with the measured magnitude are reported. Note: The possible angle intervals (second column) are calculated in the static peptide case with no membrane fluctuations included.

The back-calculated ^{15}N chemical shifts for Ala5 and Leu10, derived from the orientations of the peptide planes, show strong agreement with experimental measurements. Specifically, average chemical shift values below 100 ppm for these residues suggest that the labeled ^{15}N–H vectors are oriented nearly perpendicular to the membrane normal (see Fig.18 in [3] and Fig.4 in [4]), which closely aligns with the axis of the peptide helix. The observed standard deviations in chemical shift val-

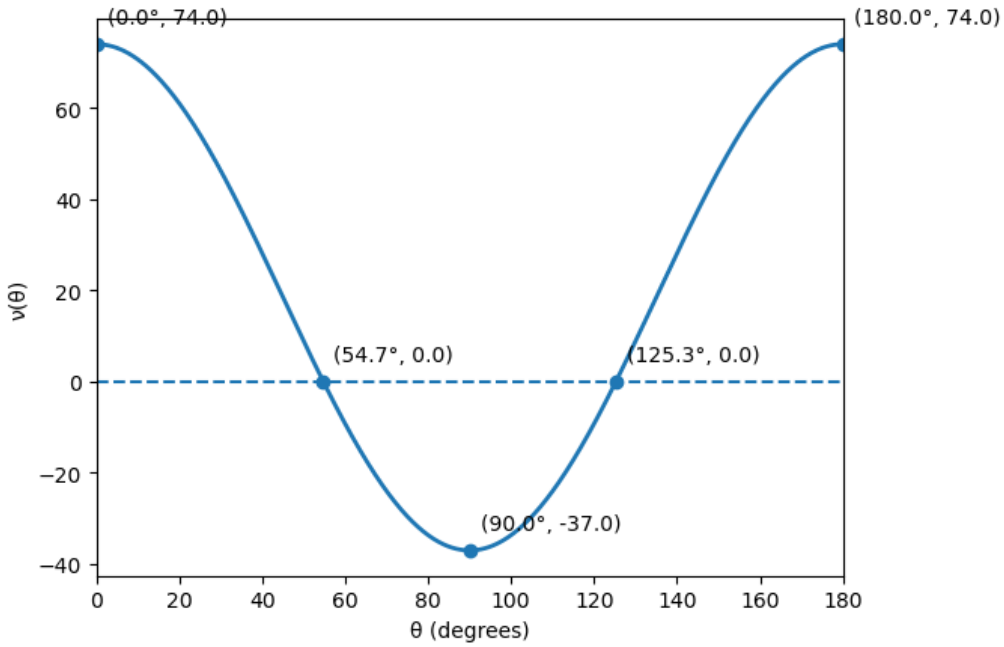

Figure 3.3: ^{2}H quadrupole splittings vs angle (ϑ) plot where X-axis represent the angle between 0 to 180 degree and the Y-axis represents the corresponding splitting values in kHz.The dotted blue line marks the magic angle and the corresponding splitting value.

ues capture contributions from both the intrinsic peptide dynamics and thermal fluctuations present during the simulations.

Despite the presence of these thermal fluctuations, the NMR parameters obtained from simulations align well with experimental data. It is important to highlight that similar degrees of variability (standard deviations from the mean) are commonly reported in studies comparing MD simulations with solid-state NMR data [5–7]. Overall, this agreement confirms that the 14A peptides adopt an antiparallel configuration and that their principal axes are nearly perpendicular to the bilayer normal, validating our structural model and nanodisc setup. Although experimental measurements were performed at 37°C, our calculations revealed no significant differences in NMR parameters between simulations conducted at 30°C and 37°C. Consequently, all further analyses were carried out at 37°C unless stated otherwise. These findings reinforce the validity of the 14A/DMPC models for further structural and dynamic characterization.

SYSTEM A	^{2}H-Ala5		^{2}H-Ala13		^{15}N-Ala5 (ppm)	^{15}N-Leu10 (ppm)	Temp (°C)	Time (ns)
	Splitting (kHz	Angles (°)	Splitting (kHz)	Angles (°)				
Run1	20 ± 26	46 ± 16	20 ± 18	90 ± 23	92 ± 27	76 ± 17	30	1000
Run2	17 ± 23	47 ± 14	21 ± 17	91 ± 23	91 ± 21	73 ± 16	30	1000
Run3	24 ± 24	43 ± 14	21 ± 16	89 ± 21	87 ± 24	80 ± 23	30	1000
Global	20 ± 25	45 ± 15	20 ± 18	90 ± 23	91 ± 25	76 ± 19	30	3000
Run1	15 ± 27	44 ± 14	18 ± 19	89 ± 25	96 ± 28	75 ± 16	37	1000
Run2	23 ± 24	49 ± 12	21 ± 16	89 ± 22	87 ± 22	75 ± 16	37	1000
Run3	13 ± 22	48 ± 16	18 ± 18	91 ± 25	97 ± 24	70 ± 13	37	1000
Global	17 ± 24	47 ± 14	19 ± 18	90 ± 24	93 ± 25	72 ± 16	37	3000
ssNMR*	19 ± 4	N/A	35 ± 2	N/A	96 ± 3	71 ± 2	37	N/A

Table 3.3: Comparison of theoretically obtained ^{2}H quadrupole splittings and ^{15}N chemical shifts for Ala5, Ala13, and Leu10 in System A with ssNMR experimental data. Theoretical values were calculated from molecular dynamics simulations and absolute values are reported. The Global row represents values computed by concatenating all independent simulation runs into a single trajectory before calculating the ssNMR parameters, to capture the overall averaged behavior. Experimental ssNMR* values are taken from Salnikov et al. [1].

SYSTEM B	^{2}H–Ala5		^{2}H–Ala13		^{15}N–Ala5 (ppm)	^{15}N–Leu10 (ppm)	Temp (°C)	Time (ns)
	Splitting (kHz)	Angles (°)	Splitting (kHz)	Angles (°)				
Global	18 ± 23	46 ± 13	22 ± 16	89 ± 22	94 ± 23	72 ± 17	30	400
Global	17 ± 27	47 ± 16	19 ± 18	89 ± 24	95 ± 26	78 ± 22	37	400
ssNMR*	19 ± 4	N/A	35 ± 2	N/A	96 ± 3	71 ± 3	37	N/A

Table 3.4: Comparison of theoretically obtained ^{2}H quadrupole splittings and ^{15}N chemical shifts for Ala5, Ala13, and Leu10 in System B with ssNMR experimental data. Theoretical values were calculated from molecular dynamics simulations and absolute values are reported. The Global row represents values computed by concatenating all independent simulation runs into a single trajectory before calculating the ssNMR parameters, to capture the overall averaged behavior. Experimental ssNMR* values are taken from Salnikov et al. [1].

3.1.4 Uncover the Interactions that Stabilize 14A Peptide-Lipid Assemblies

3.1.4.1 Peptide-peptide interactions

Peptide–peptide contacts are central to nanodisc stability. Unlike MSP-based nanodiscs [8], apoA-I mimetic peptides are held together solely by non-covalent forces as they encircle the discoidal lipid bilayer. ssNMR measurements on the 14A peptide point to antiparallel dimerization [1], yielding a belt-like arrangement around the disc. Using this structural hypothesis, we constructed and ran MD simulations to reproduce the peptide–lipid assembly. ssNMR observables back-calculated from the trajectories closely match experiment, corroborating both the antiparallel configuration and the near-perpendicular orientation of the peptide axes relative to the nanodisc normal (Fig.3.2 A, B). The simulations further delineate the specific molecular interactions that sustain this architecture.

MD analyses highlight a key role for the central tyrosine (Y7) in mediating aromatic π–π stacking between neighboring peptides (Fig. 3.4A). The para-oriented

hydroxyl groups are positioned away from the interacting rings, promoting efficient stacking. The corresponding free-energy profile shows two minima at 4.3–4.7 Å with ring-normal angles of 0–10° and 170–180°, consistent with parallel, aligned stacks. The barrier separating these wells is $<1\ kcalmol^{-1}$, allowing rapid flipping between equivalent orientations without disrupting the interaction. The mean intermolecular separation is 4.5 Å in both simulated disc sizes (Fig. 3.4B, D), indicating that Y7–Y7 stacking occurs near the interface of antiparallel peptides and makes a substantial contribution to dimer stabilization.

Phenylalanine at the peptide terminus (F14) also engages in lateral π–π contacts with F14 residues from neighboring dimer units (Fig. 3.4A). While these interactions assist in overall belt stabilization, they are less persistent in the bound state than the Y7-mediated stacks. Two-dimensional free-energy maps for F14–F14 pairs in both smaller and larger nanodiscs (Fig. 3.4C, E) display a common signature: a continuous low-energy ridge spanning ring-normal angles from 0–180° yet confined to separations of 4–6 Å. Rather than occupying discrete wells, the rings sample a continuum of orientations at a characteristic π–π distance, forming a laterally cohesive but highly compliant network. This mechanical pliability enables the peptide belt to expand, contract, or adopt oval shapes to accommodate lipid fluctuations across nanodiscs of different diameters without loss of integrity.

Together, these non-covalent interactions maintain peptides as stable dimers, while dynamic contacts between dimer blocks help preserve the near-perpendicular alignment of the peptide axes with respect to the disc normal. The peptides orient so that hydrophobic residues cover the lipid acyl chains, creating a predominantly hydrophobic peptide–peptide interface, whereas polar residues effectively shield these surfaces. Overall, the results support a conserved, belt-like organization of peptides around the discoidal bilayer, consistently observed across all simulated systems.

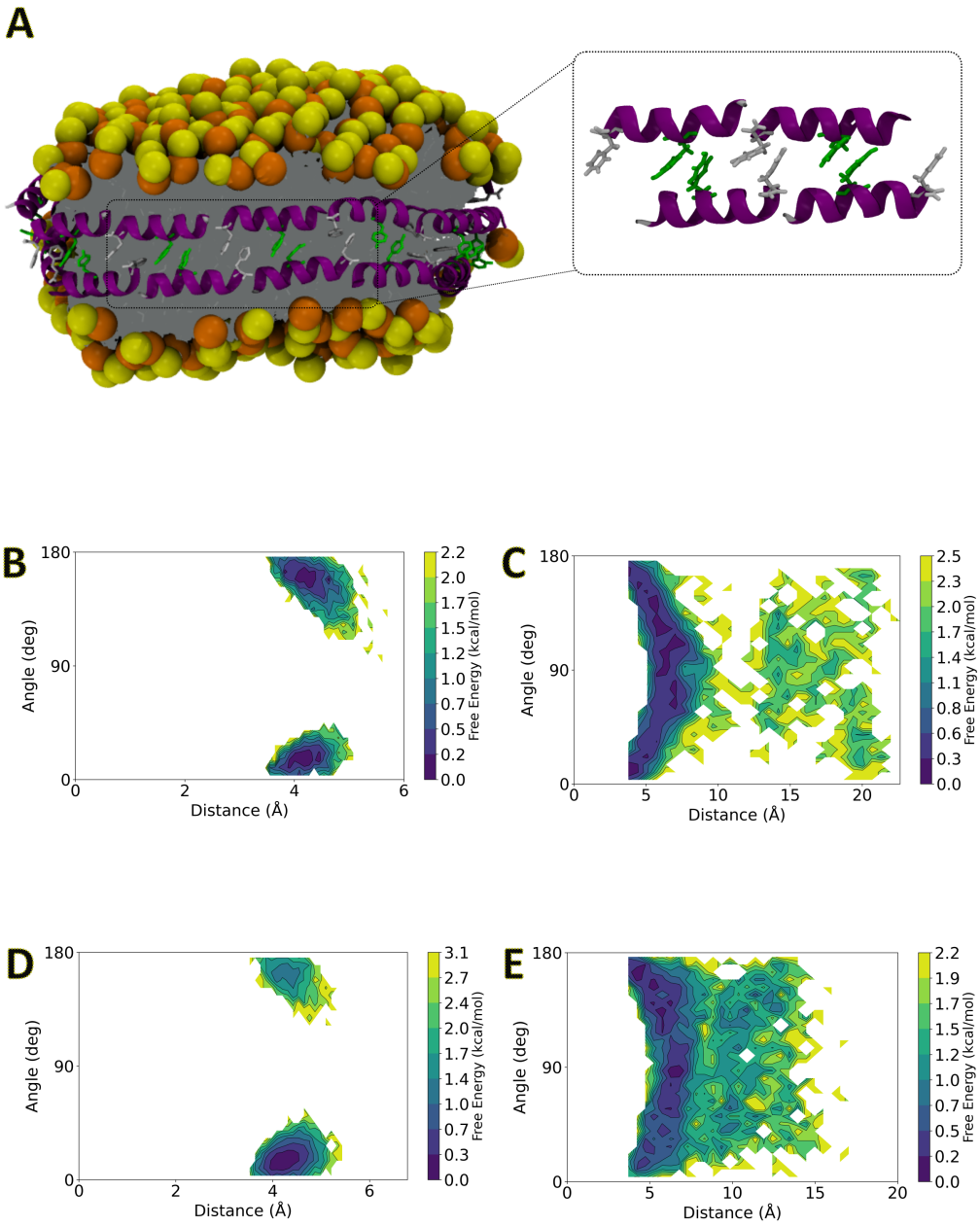

Figure 3.4: (A) Schematic depiction of peptide interactions illustrating both the formation of dimeric units and the lateral contacts established between adjacent dimers. (B) Free energy profile of tyrosine residues (Y7) located at the dimer interfaces for system A, while (D) shows the corresponding profile for system B. (C) Free energy profile of phenylalanine residues (F14), which mediate lateral interactions between neighboring dimer blocks in system A, while (E) shows the corresponding profile for system B.

3.1.4.2 Lipid-peptide interactions

Having characterized the interactions among peptides around the discoidal assembly, we next assessed their contacts with phospholipids. Given the peptides' amphipathic character and spatial arrangement, we anticipated that polar and aromatic residues at the interface would engage both DMPC headgroups and the hydrophobic acyl chains.

To quantify the significant salt bridges between the peptides and lipids, we calculated their radial distribution functions (g(r))(section:2.3.2). We focused on three specific atomic pairings: the nitrogen in lysine with the phosphorus in DMPC, the carbon in glutamate with the choline nitrogen in DMPC, and the hydroxyl group in tyrosine with the choline nitrogen in DMPC. This analysis allowed us to establish interaction cutoff thresholds of $\leq$4.7 Å for the lysine–phosphorus connection and $\leq$ 5.7 Å for the glutamate–nitrogen and tyrosine–nitrogen connections. These thresholds were subsequently used to compute the average number of salt bridges formed by each peptide (see Fig. 3.5).

Consistent with earlier simulation studies [9, 10], both lysine (K9) and glutamic acid (E12) establish salt bridges with the DMPC headgroups, adopting a "snorkel-like" orientation at the edge of the assembly. Specifically, the lysine's ammonium side-chain (NH_3^+) associates with the phosphate group of DMPC, while the glutamic acid's carbonyl group interacts with the choline of DMPC (Table:3.5; Fig.3.6A; Fig.3.5). Although three lysine residues are present in each peptide, the orientation of the peptide places only lysine (K9) at the interface, allowing it to selectively engage with phosphate groups. Moreover, the tyrosine (Y2) residue, which features a hydroxyl group on its aromatic ring, also promotes salt-bridge contacts with the DMPC choline group (Fig.3.6B; Table 3.5).

Aromatic residues such as phenylalanine (F6) and tyrosine (Y2) also engage substantially with the hydrophobic lipid tails. We quantified this by measuring the angle between the normal of the aromatic ring plane and the membrane normal (z-axis) (Section: 5.2). The resulting distribution indicates that the aromatic ring planes are predominantly perpendicular to the membrane normal—thus parallel to the bilayer plane—acting as anchors (Fig.3.6B, C; Fig.3.7). Collectively, these non-covalent interactions stabilize the peptide arrangement in a "belt"-like manner and may modulate lipid properties near the nanodisc rim.

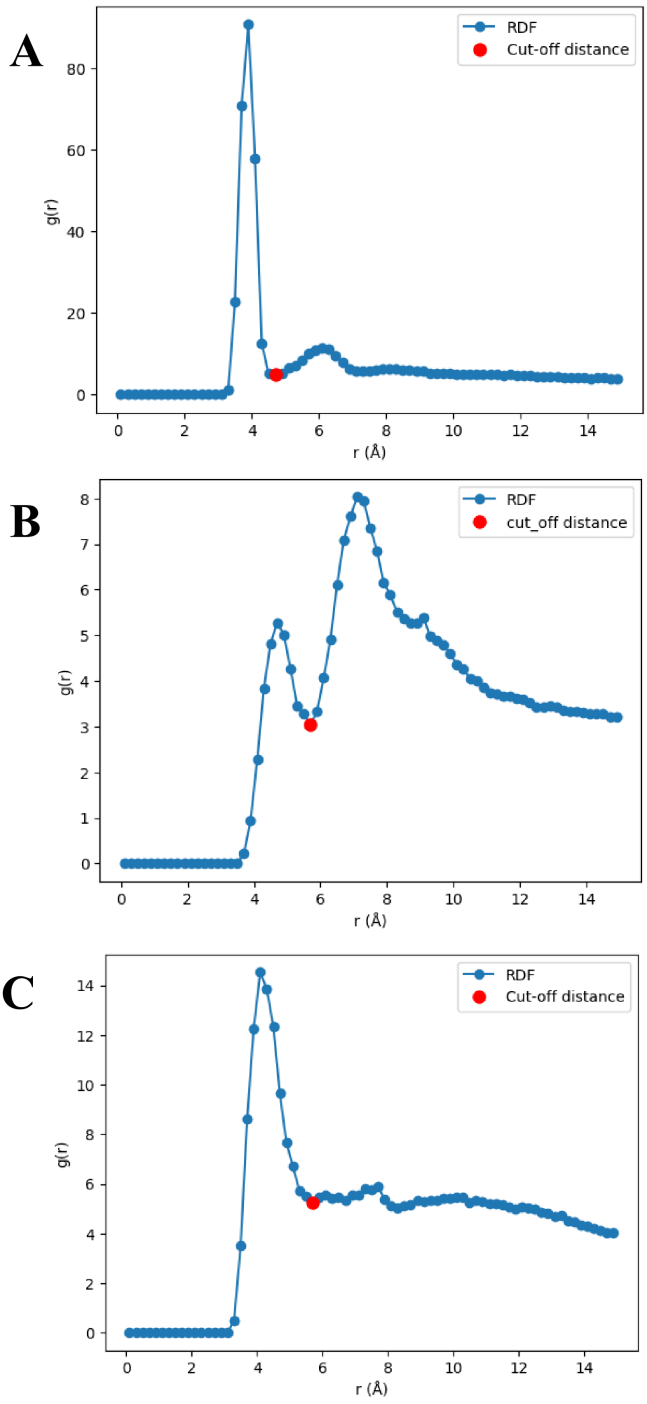

Figure 3.5: Cutoff distances for counting salt bridges were determined from radial distribution functions: (A) 4.7 Å between the nitrogen of the amino group in lysine (9K) side chains and the phosphorus of DMPC molecules; (B) 5.7 Å between the carbon of the carboxyl group in glutamic acid (12E) side chains and the nitrogen of DMPC molecules; (C) 5.7 Å between the hydroxyl group at the para position of tyrosine (2Y) and the nitrogen of DMPC molecules.

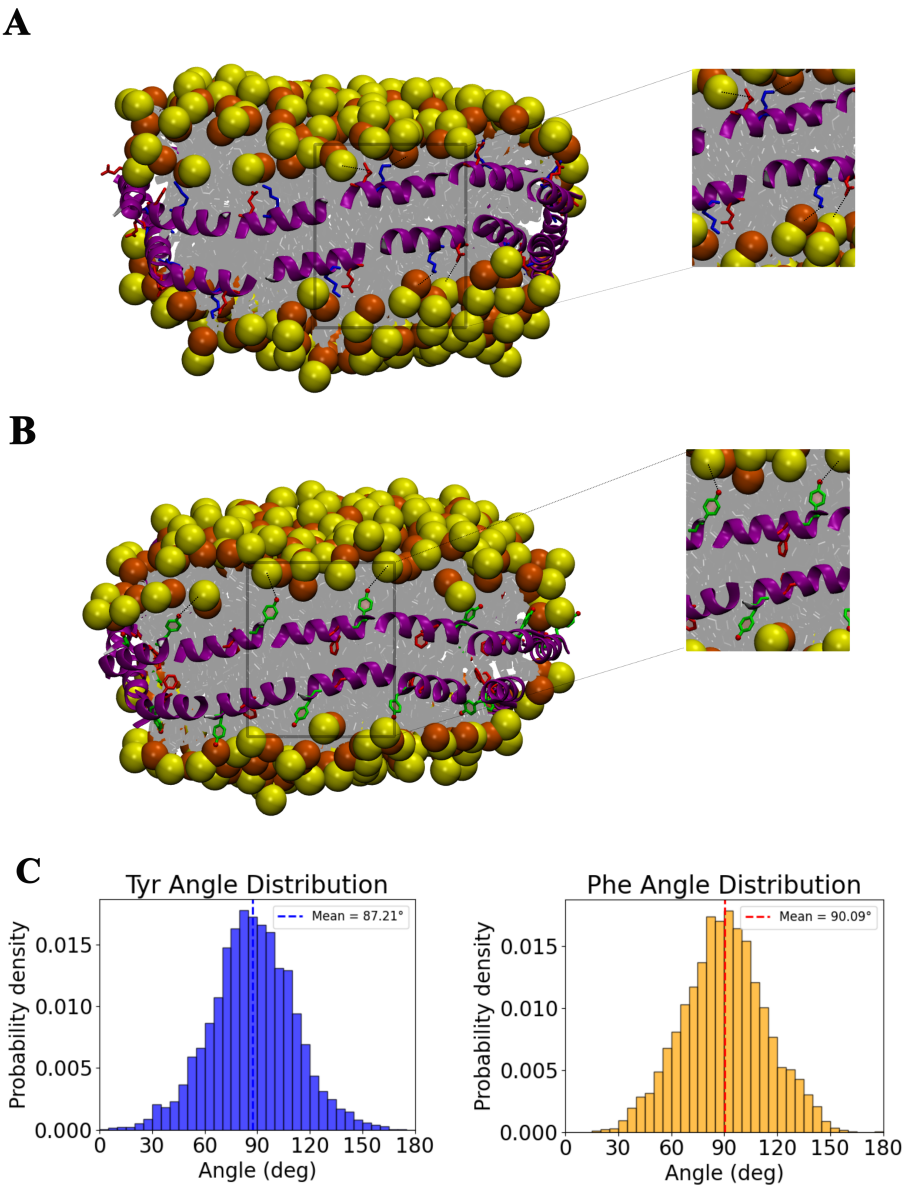

Figure 3.6: Representation of system A configuration sampled during molecular dynamics (MD) simulation, highlighting key interactions and orientations. (A) Salt bridge interactions between peptides and lipid head groups: a lysine (K9) – phosphate salt bridge formed by interactions between the amino group (NH_3^+) of the lysine (blue) and the phosphate group of DMPC (orange), and a glutamic acid (E12) – choline salt bridge formed by interactions between the glutamate carboxyl group (red) and choline group of DMPC (yellow). (B) Orientation of aromatic residues along the bilayer normal, with tyrosine (green) and phenylalanine (red) rings aligned nearly parallel to the membrane normal. Additionally, a salt bridge interaction is observed between the hydroxyl group (red ball) in the para position of the tyrosine aromatic ring and the choline group of the DMPC (yellow). (C) Probability distribution of the aromatic ring normal orientations for tyrosine and phenylalanine within the 0°–180° range of system A.

System	No. of Salt Bridges per Peptide		
	Lys–Phos	Glu–Choline	Tyr–Choline
A	0.50	0.43	0.68
B	0.71	0.68	0.61

Table 3.5: Salt bridges measured as the number of contacts between (i) the amino group (NH_3^+) of Lys (K9) and the phosphate group of DMPC, (ii) the carboxyl group of Glu (E12) and the choline group of DMPC, and (iii) the hydroxyl group of Tyr (Y2) and the choline group of DMPC, averaged over simulation frames and normalized by the number of peptides.

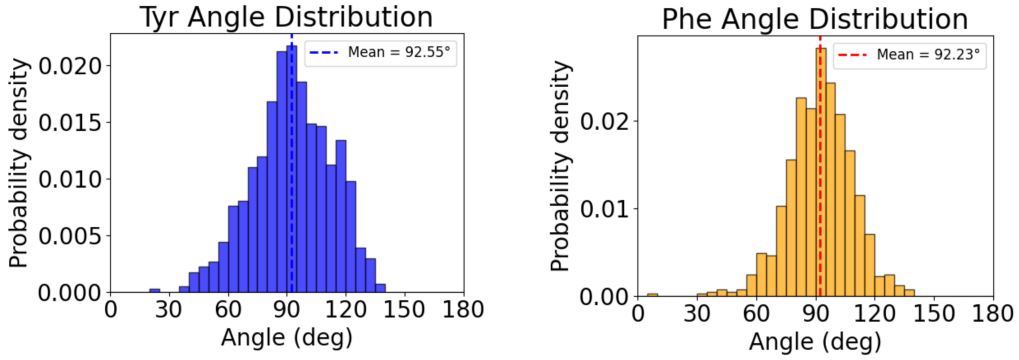

Figure 3.7: Probability density distribution of the aromatic ring normal orientations for tyrosine and phenylalanine within the 0°–180° range. These plots were obtained from the system B simulation.

3.1.4.3 Lipid properties of 14A peptide nanodiscs at different temperature

Building on prior experimental [11, 12] and simulation work [13, 14], nanodisc lipid bilayers display modest deviations from the behavior of pure lipid bilayers. Because nanodiscs incorporate membrane scaffold proteins, lipid–protein interactions drive shape fluctuations that modulate lipid properties. Notably, no simulations have specifically examined the lipid properties of nanodiscs stabilized by apoA1-mimetic peptides. Experimental studies on 14A-based nanodiscs [15] show that they form size-tunable assemblies suitable for membrane-protein characterization and align robustly in static magnetic fields for NMR studies. Because MP structure and dynamics are highly sensitive to the surrounding lipid environment, this gap requires attention. Here, we analyzed a 14A/DMPC nanodisc, quantifying the DMPC bilayer thickness and acyl-chain order parameter (S_{CH}) at 30 °C and 37 °C.

For analysis, the lipid within nanodiscs was partitioned by peptide proximity—within or beyond 10 Å—following established methods [14]. Across temperatures and nanodisc sizes, bilayer thickness and order parameters exhibited consistent trends. Compared with a pure DMPC bilayer slab, 14A/DMPC nanodiscs showed pronounced rim–core heterogeneity: lipids near the rim adjacent to the apoA-I mimetic peptide belt were thinner and less ordered, whereas core lipids were more ordered and tightly packed.

In the small nanodisc (System A), this rim–core inhomogeneity is stronger: lipids at the center are even more ordered than in a pure DMPC bilayer, while those within 10 Å of the peptide belt are thinner and highly disordered (Fig. 3.9A). Raising the temperature from 30 °C to 37 °C reduces both average bilayer thickness and chain order across the disc, yet the core remains distinctly more tightly packed than the rim. The larger nanodisc (System B) displays the same pattern, though less pronounced. At 30 °C, the core closely resembles a pure DMPC bilayer, with only the rim region noticeably thinner and more disordered (Fig. 3.9C). Increasing the temperature to 37 °C produces uniform thinning and a modest drop in chain order at both rim and core (Fig. 3.9D). Even so, core ordering exceeds that of a pure DMPC bilayer, and the rim remains the most perturbed region.

Both System A and System B show slight decreases in thickness and lipid order at the rim and core with increasing temperature (Fig. 3.9A–D). This temperature-induced reduction in thickness and order is consistent with prior observations in MSP1/DMPC nanodiscs above the DMPC phase transition (Fig. 7 in [16]). Across nanodisc sizes and at both temperatures studied, core lipids are consistently thicker and more ordered than in a pure DMPC bilayer.

These results align with previous simulations of DMPC nanodiscs incorporating various MSP constructs, including MSP1, MSP1E1, MSP1E2, and (Δ)-H5 peptides [11–14, 17].

System	Peptide Belt Diameter (nm)		Lipid disc Diameter (nm)		Average Diameter (nm)	Helicity (%)	Temperature (°C)
	X-axis	Y-axis	X-axis	Y-axis			
A	10.97	10.05	10.78	9.54	10.35	85.40	30
A	10.80	10.20	9.96	9.52	10.12	85.45	30
A	10.74	10.47	10.04	9.54	10.20	85.02	30
A	10.99	10.47	10.69	9.66	10.46	85.36	37
A	10.81	10.26	10.24	9.55	10.22	85.38	37
A	10.81	10.78	10.20	10.01	10.45	85.25	37
B	17.92	17.21	16.92	16.28	17.09	85.17	30
B	17.82	17.85	16.74	17.35	17.45	85.34	37

Table 3.6: Average diameter of the nanodiscs measured based on the mass-density distribution profiles of the peptide belt and lipid disc at 30 °C and 37 °C. Helicity (%) corresponds to the time-averaged α-helical content of the peptide calculated over the full production trajectory mentioned in Table 3.1

.

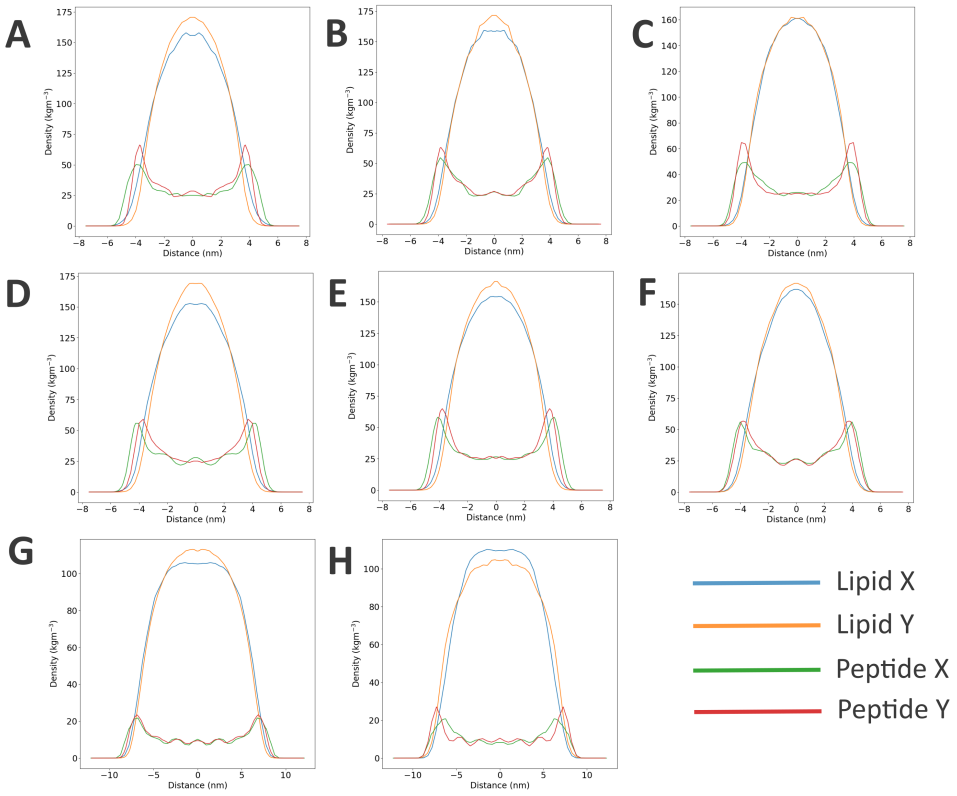

Figure 3.8: Mass density profiles of nanodiscs with varying peptide and lipid compositions. (A–F): System A; panels (A–C) correspond to simulations at 30°C, and (D–F) at 37°C. (G, H): System B; (G) at 30°C and (H) at 37°C. The plots show lipid and peptide mass density distributions along the x and y axes. "Lipid x" and "Lipid y" denote lipid densities along the respective axes, while "Peptide x" and "Peptide y" show peptide mass densities. These profiles were used to calculate the average nanodisc diameter for each system (see section:2.3.3).

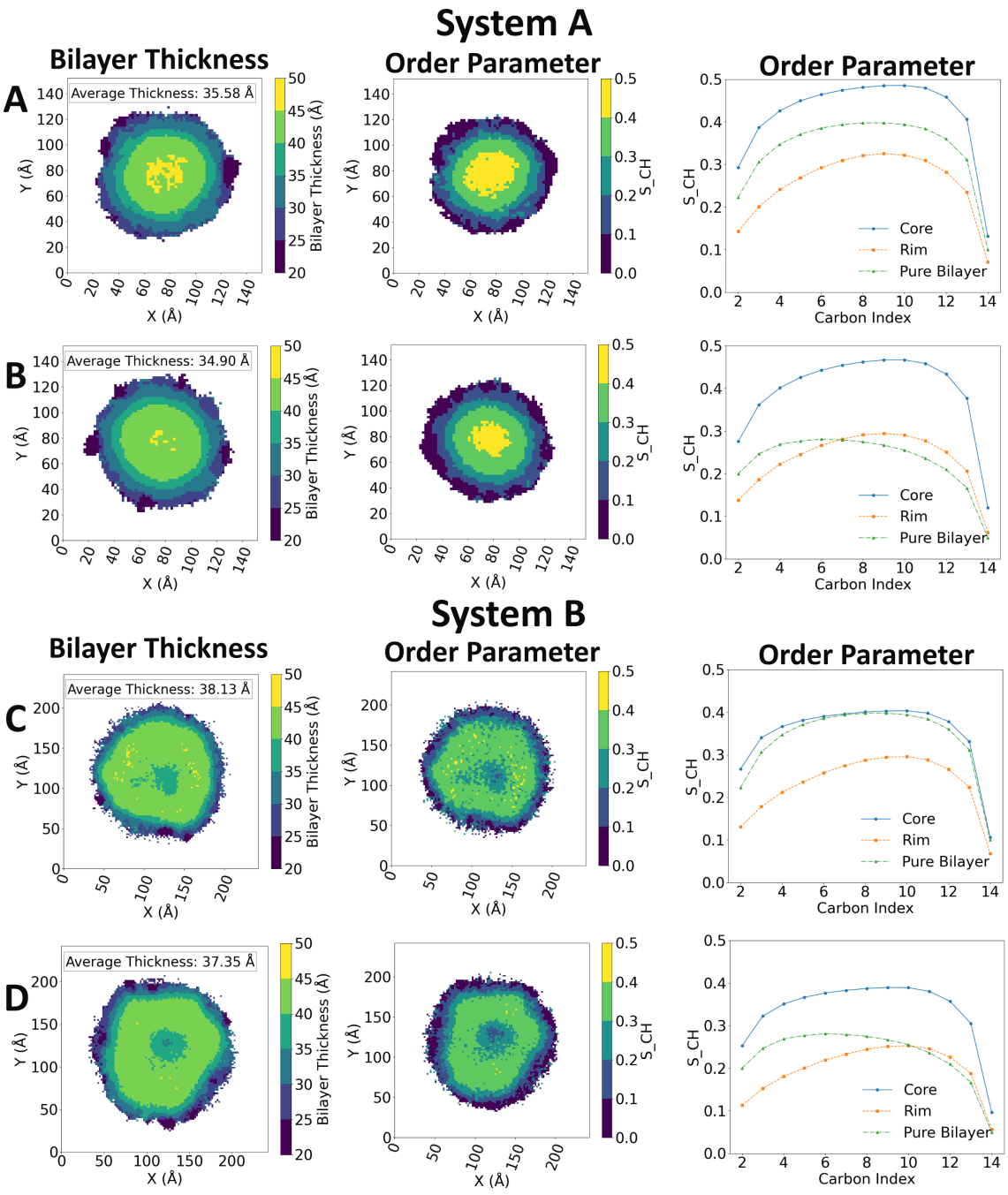

Figure 3.9: 2D maps of bilayer thickness (left panels), average lipid order parameters calculated over all C–H bonds in the two aliphatic tails of DMPC lipids (center panels), and order parameters as a function of carbon position along the lipid tails (right panels). The rim zone is defined as all lipids within 10 Å of the 14A peptides, while the core zone includes all lipids located beyond this distance. Panels (A) and (B) correspond to System A, simulated at 30°C and 37°C, respectively. Panels (C) and (D) correspond to System B, simulated at 30°C and 37°C, respectively.

3.1.5 Discussion

We carried out an in-depth investigation into the structural and dynamic characteristics of lipid nanodiscs formed with the apoA-I mimetic peptide 14A, using all-atom molecular dynamics simulations. The peptide orientations obtained from these simulations were validated by comparing the ^{2}H-NMR quadrupole splittings and ^{15}N chemical shifts of specific residues with solid-state NMR data, showing strong agreement.

Our analysis focused on the dimeric configuration of the 14A peptide, addressing prior hypotheses [1] and identifying key interactions that stabilize the dimer. Specifically, π-π interactions between tyrosine residues (Y7) in anti-parallel peptide orientations were found to play a crucial role in stabilizing the dimers. Phenylalanine residues (F14), located at the junctions between adjacent dimer blocks, also formed π-π interactions, though these were more transient than the tyrosine contacts. The fleeting nature of these F14 interactions may lead to minor openings at dimer interfaces. While lipid exchange was not directly observed in our simulations, experimental evidence suggests that peptide-based nanodiscs facilitate lipid exchange during particle collisions through such interface cleavages, offering an energetically favorable route [18, 19]. This mechanism contrasts with lipid exchange in nascent apoA-I nanodiscs, where diffusion is the dominant mode, as revealed by time-resolved small-angle neutron scattering (SANS) studies in aqueous environments [20].

We also examined specific lipid–peptide interactions. Polar residues such as lysine (K9) and glutamic acid (E12) engage in electrostatic interactions with the charged headgroups of DMPC lipids. Aromatic residues like tyrosine (Y2) and phenylalanine (F6) consistently anchor the peptides to the hydrophobic regions of the lipid tails. Notably, the hydroxyl group of Y2, situated para to its aromatic ring, forms specific interactions with the choline groups of DMPC lipids. A comparison between 14A/DMPC nanodiscs and a pure DMPC bilayer slab revealed clear differences in lipid properties between the rim and the core. Lipids at the nanodisc edge, near the apoA-I mimetic peptide belt, exhibited reduced thickness and order in both nanodisc sizes. Similar temperature-dependent thinning and disorder were observed near the rim and core. In line with prior studies on MSP-based nanodiscs [16, 17] and our findings, we propose that direct lipid–peptide interactions could contribute additional disorder to lipid tails near the rim. Overall, our results are consistent with previous studies of MSP/DMPC nanodiscs [11–14, 16, 17], suggesting that peptide-based nanodiscs may exhibit similar lipid properties.

The short length of the 14A peptide makes it easily synthesizable, yet it effectively retains interactions necessary for stabilizing lipid bilayer patches, closely mimics lipid properties of the MSP-based nanodiscs, and demonstrates an ordered dimeric arrangement of peptides in the apoA-I mimetic peptide family. These 14A peptide-based nanodiscs maintain efficient alignment capabilities in magnetic fields suitable for ssNMR studies and offer size tunability [15]. Thus, they serve as promising plat-

forms for detergent-free membrane protein characterization. Moreover, the ability of 14A to stabilize lipid bilayer patches via strong lipid-peptide interactions could further facilitate the study and development of active therapeutic agents for cardiovascular disease.

We acknowledge the limitations of our study, including restricted conformational sampling and the assumptions underlying our initial structure, which were informed by earlier research [1]. As a result, we explored only a subset of the possible structural configurations. A more comprehensive structural ensemble will require advanced sampling techniques. Nonetheless, our findings support the hypothesis that 14A peptides [1] form a belt-like dimeric arrangement around the lipid bilayer patch and elucidate the key stabilizing interactions in this architecture. Despite these methodological constraints, the study lays a strong foundation for future research, including work on nanodiscs formed by the 18A peptide, 4F, 4F-P-4F, and other related mimetic peptides.

3.2 ApoA-I Mimetic Peptides Nanodisc MD Simulation: Comparing with SAXS Data

Here, we investigate peptide–lipid nanodiscs formed by the 4F peptide and its tandem dimer, 4F-P-4F, to resolve their morphology at the atomic level while simultaneously validating the modeling and analysis protocol used. In parallel, we processed and analyzed collaborator-provided raw SAXS data to assess whether the scattering signal is sufficiently informative to capture structural differences arising from peptide sequence and topology at the nanodisc rim.

Because direct NMR constraints on peptide orientation within discoidal bilayers are limited for 4F and 4F-P-4F, we constructed structural models guided by our prior 14A-based nanodisc study and by published NMR data on related apoA-I mimetic peptides [1, 21, 22]. To probe global shape, size, and structure, we computed SAXS profiles from explicit-solvent [23], all-atom MD–derived nanodisc ensembles, and compared them with experimental SAXS data from our collaborators. SAXS is well suited to nanodisc systems [24–27]: it reports ensemble-averaged size, shape, and bilayer architecture (e.g., disc diameter, bilayer thickness, and anisotropy) that are difficult to obtain from imaging or high-resolution methods alone. Because interpreting SAXS curves depends on accurate forward modeling, we explicitly included hydration effects when calculating theoretical profiles from simulations, enabling a direct, parameter-free comparison with experiment.

We evaluated the MD models by comparing experimental scattering curves to theoretical profiles computed from the trajectories, using an explicit hydration shell without empirical tuning of shell parameters [23]. By analyzing both the scattering intensity $I(q)$ and the pair-distance distribution $P(r)$, we assess the degree of structural agreement, identify likely sources of discrepancy (e.g., polydispersity, aggregation, or interparticle effects), and extract physical insight into peptide-based nanodisc organization. This integrative framework provides key constraints on plausible sizes and morphologies and establishes a principal basis for refining the nanodisc models.

3.2.1 Computational Details

Based on prior NMR data from related apoA-I mimetic peptide nanodiscs of 18A, 14A, 4F [1, 21, 22] and insights from our 14A peptide study, we built an initial structure of nanodiscs composed of 4F and 4F-P-4F peptides. Following earlier studies, the amphipathic helices were arranged in an antiparallel belt around a discoidal lipid bilayer using our established lipid–peptide assembly workflow (see section: 2.2). All-atom molecular dynamics simulations were then performed using the same protocol as for the 14A nanodiscs (see section: 2.2.3). Simulations were conducted at 30 °C to match the SAXS measurement temperature. Further specification of each nanodisc system mentioned in Table 3.7.

For each system, SAXS profiles were computed snapshot-by-snapshot over the full MD trajectory with GROMACS-SWAXS [23] (Specific trajectory lengths for each system are listed in Table 3.7.) and subsequently averaged to obtain $\langle I_{\text{calc}}(q)\rangle$. Real-space pair-distance distribution functions, $P(r)$ [28], were derived from the SAXS curves using GNOM as a radius of gyration option from Guinier analysis [29] implemented in the ATSAS package [30].

Real-space pair distance distribution function (PDDF) $P(r)$ can be calculated,

$$I(q) = n \cdot I_{\text{particle}}(q) = n \int_0^{D_{\max}} P(r) \frac{\sin(qr)}{qr} dr \tag{3.2}$$

where n is the number of particles in solution, and $D_{\max}$ is the maximum intraparticle dimension. The function $P(r)$ contains the structural information of the particle, encoding the distribution of all interatomic distances within the scattering object.

Guinier analysis:

$$I(q) \approx I(0) \exp\left(-\frac{q^2 R_g^2}{3}\right). \tag{3.3}$$

R_g and I(0) can be determined by performing a linear fit of lnI(q) versus q^2, a representation commonly referred to as the Guinier plot. The range of data points used for this linear fit defines the Guinier region. approximation is valid in the Guinier regime, i.e., for a small $q^2 R_g^2$ value (typically $q^2 R_g^2 \leq 1.3$)

System	Type	No. of Peptides	No. of DMPC	Total no. of atoms	Simulation Time (ns)
A1	14A	24	186	326485	1000
B1	4F	16	122	305913	1000
B2	4F	20	186	327685	1000
B3	4F	24	298	734984	500
B4	4F	28	316	771649	300
B5	4F	32	496	1210589	500
B6	4F	36	570	1307371	300
B7	4F	40	734	1606403	500
B8	4F	44	882	2046473	200
B9	4F	48	1082	2529532	150
B10	4F	52	1274	3022897	150
B11	4F	56	1506	3643263	130
B12	4F	60	1738	4270424	150
B13	4F	64	2006	5044218	200
B14	4F	68	2272	5817911	180
B15	4F	72	2588	6759397	130
C1	4F-P-4F	10	186	500130	1000
C2	4F-P-4F	12	218	543149	100
C3	4F-P-4F	18	734	1748831	100
C4	4F-P-4F	28	1434	3692066	100
C5	4F-P-4F	34	2236	6085716	100

Table 3.7: Simulation system details for MD studies of DMPC bilayer patches stabilized by 14A, 4F, and 4F-P-4F peptides. Reported are the numbers of peptides, DMPC lipids, total atoms, and simulation time. Simulations were conducted at 30°C. For convenience, we label the simulated systems as follows: A series: 14A; B series: 4F; C series: 4F-P-4F. Here, "simulation length" refers to the production run only, without any positional restraints.

3.2.2 Comparing Theoretical SAXS Curves Across Different Peptide Scaffold Nanodiscs of Similar Size

To evaluate how the choice of peptide scaffold influences the global structure of nanodiscs, we compared theoretical SAXS curves computed from MD trajectories of three systems—14A/DMPC (A1), 4F/DMPC (B2), and 4F–P–4F/DMPC (C1)—that were constructed to have comparable overall diameters (Fig 3.2A, 3.10A, B). This comparison serves two purposes. First, it tests whether SAXS is sensitive to scaffold-specific differences when nanodisc size is held approximately constant. Second, it provides an internal check of the simulation and SAXS–calculation pipeline, since these systems differ in peptide identity but are structurally similar at the overall nanodisc level.

Figure 3.12 shows the SAXS profiles calculated from the MD ensembles for the three systems. All three curves exhibit a sharp minimum below $q \approx 1$ nm^{-1}, followed by a broad maximum at higher q, hallmark features of discoidal lipid–protein particles that are also observed experimentally. Despite the differences in peptide sequence and stoichiometry, the positions of these minima and maxima are essentially indistinguishable across A1, B2, and C1. The similarity in the overall scattering patterns indicates that SAXS curves are dominated by the nanodisc's global size and shape rather than by the details of peptide sequence (scattering from the amino acids composing it). This behavior is consistent with the known sensitivity of SAXS to large-scale structural parameters such as disc diameter and bilayer thickness, whereas finer features associated with peptide identity are typically averaged out in the one-dimensional scattering profile.

To quantify these observations, we extracted structural parameters from both the MD trajectories and the SAXS curves, including the radius of gyration (R_g), the average nanodisc diameter determined from mass–density profiles, and the maximum particle dimension ($D_{\max}$) obtained by indirect Fourier transform of the SAXS curves. The results are summarized in Table 3.8. Across all three systems, the derived parameters are nearly identical, with average diameters of ~ 10 nm and $D_{\max}$ values of $\sim$ 10–10.5 nm. Guinier analysis of the calculated SAXS curves yields consistent R_g estimates, further confirming that these systems are structurally similar at the global level despite having different peptide scaffolds.

The corresponding real-space pair–distance distribution functions $P(r)$ (Figure 3.13) provide additional structural insight. The $P(r)$ curves for all three systems have similar overall shapes and reach their maxima and cutoffs at nearly the same distances, indicating that the dominant length scales within the particles are equivalent. Likewise, mass–density distributions (Figure 3.11) show nearly circular discoidal bilayers surrounded by peptide belts, with only subtle variations in the radial distribution of peptide density.

Together, these analyses demonstrate that, for nanodiscs of comparable size, SAXS is largely insensitive to which peptide scaffold is used. As a result, SAXS curves

alone are insufficient to distinguish between nanodiscs formed by different apoA-I mimetic peptides when their global dimensions are matched. This has important methodological implications: relying exclusively on SAXS fitting with simple geometric form factors can lead to ambiguous structural interpretations, as different molecular assemblies may produce indistinguishable SAXS profiles if their overall shape and size are similar. Consequently, integrating SAXS data with either complementary experimental constraints (e.g., NMR, EPR, cryo–EM) or Molecular dynamics simulations, as done here, is essential for building realistic structural models of peptide–lipid nanodiscs.

Note: Here, R_g from MD—computed over the peptide-lipid assembly is a mass-weighted, time-averaged quantity that typically excludes the hydration shell. By contrast, the Guinier R_g is contrast-weighted over the full scatterer (peptide + lipid + hydration shell); therefore, the two values are not expected to coincide.

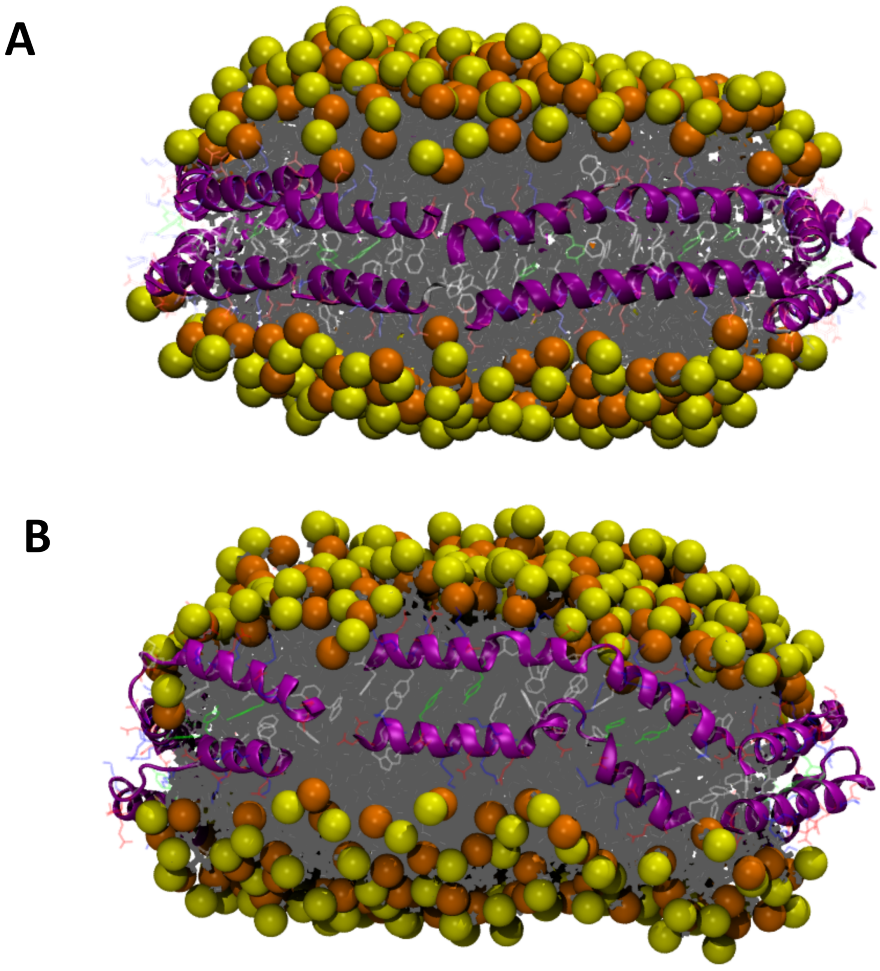

Figure 3.10: Pictorial representation of 4F/DMPC and 4F–P–4F/DMPC nanodiscs. (A) System B2 (4F/DMPC). (B) System C1 (4F–P–4F/DMPC).

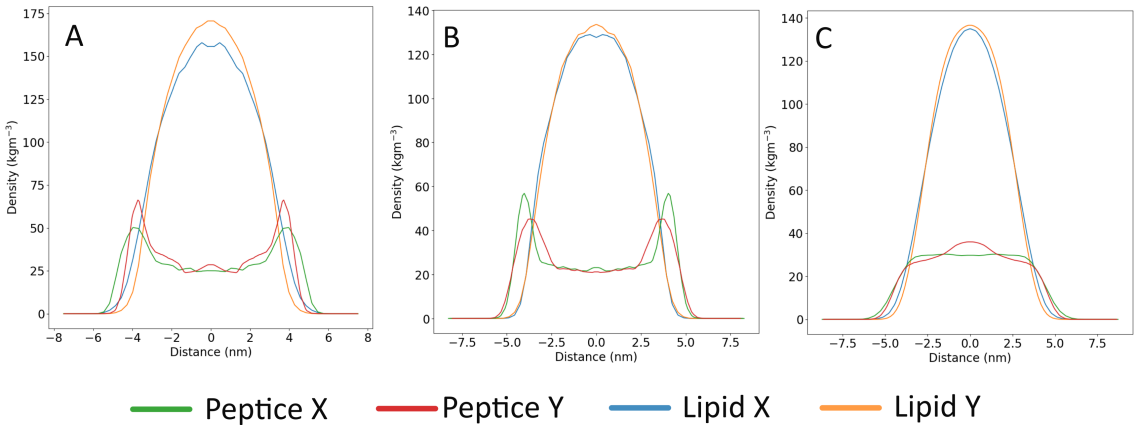

Figure 3.11: Mass density distribution profiles of 14A, 4F and 4F-P-4F nanodiscs.(A): System A1, and (B): System B2, (C): System C1. The plots show lipid and peptide mass density distributions along the x and y axes. "Lipid x" and "Lipid y" denote lipid densities along the respective axes, while "Peptide x" and "Peptide y" show peptide mass densities (see section: 2.3.3). These profiles were used to calculate the average nanodisc diameter for each system.

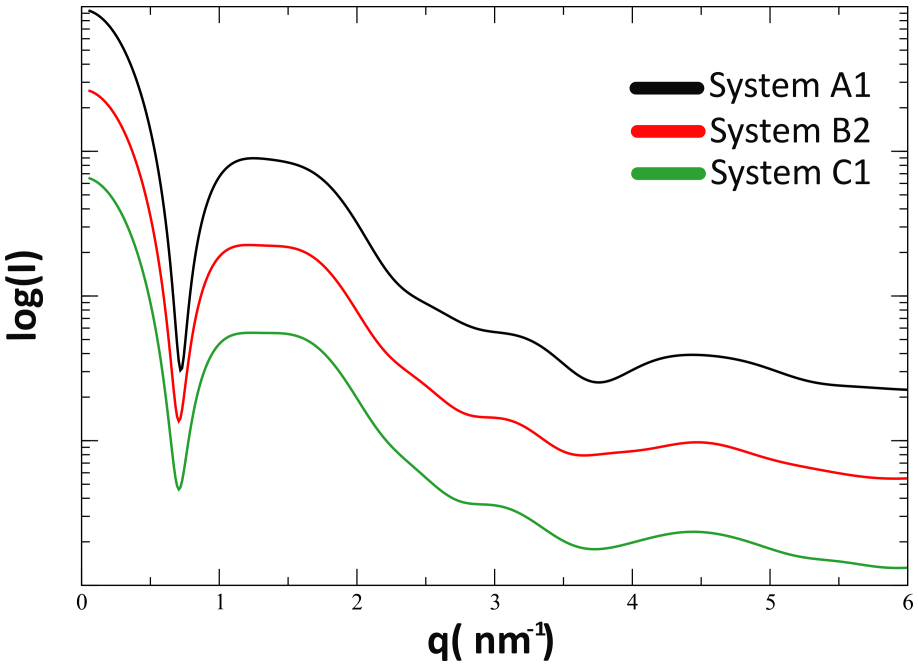

Figure 3.12: Calculated Small-angle scattering curves of system A1, B2, C1. The curves are vertically separated for clarity.

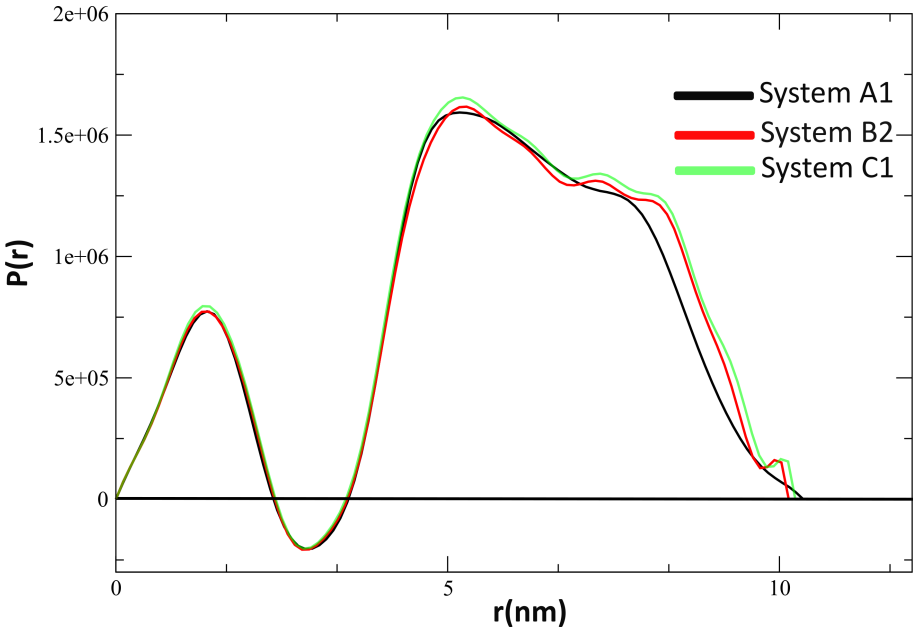

Figure 3.13: Pair-distance distribution functions, P(r), obtained by indirect Fourier transform (IFT) of the corresponding SAXS curves for systems A1 (14/DMPC), B2 (4F/DMPC), and C1 (4F-P-4F/DMPC). The inferred D_{max} for each system are derived from the respective P(r) profiles

System	R_g (MD) [nm]	R_g (Guinier Approx) [nm]	Average Diameter (MD) [nm]	$D_{\max}$ [nm]
A1	3.5	4.6	10.3	10.3
B2	3.4	4.6	10.2	10.1
C1	3.5	4.6	10.5	10.2

Table 3.8: Summary of size metrics for systems A1, B2, and C1. *MD-derived quantities:* R_g from radius-of-gyration analysis and the average nanodisc diameter from mass–density distributions. *SAXS-derived quantities:* Guinier analysis approximated R_g , and $D_{\max}$ from the pair-distance distribution $P(r)$ obtained by indirect Fourier transform (IFT).

3.2.3 Preliminary Data Analysis on Experimental SAXS Curves

Experimental SAXS datasets for 4F/DMPC and 4F–P–4F/DMPC were measured by the group of Ruth Prassl (Medical University of Graz, Austria) at the Austrian SAXS beamline, Elettra Sincrotrone Trieste (Italy). Samples were prepared at a nominal peptide-to-lipid molar ratio of 1:40 to match the conditions used in parallel biological assays conducted by the group of Günther Marsche (Medical University of Graz). The raw scattering profiles were provided by the experimental collaborators (Fig. 3.14A); all subsequent data reduction and analysis were performed by us to complement these measurements with MD simulations to obtain valuable information. Importantly, Size-exclusion chromatography–coupled SAXS (SEC–SAXS) was

not employed prior to measurement; as a result, we could expect sample heterogeneity, aggregation, or interparticle effects may contribute to the scattering signal.

We assessed the quality of the experimental SAXS data for 4F/DMPC and 4F-P-4F/DMPC by Guinier analysis [29], followed by an indirect Fourier transform (IFT) [28]. As nanodiscs were expected in the sample, we used the pair-distance distribution function $P(r)$ from IFT to estimate the maximum particle dimension $D_{\max}$, which in this context approximates the diameter of the largest nanodiscs present.

Both datasets display the characteristic minima and maxima of nanodiscs reported previously; however, anomalous low-q behavior—an intensity upturn as well as a downturn below $q \approx 0.2\,\mathrm{nm}^{-1}$ indicates possible polydispersity, aggregation, and/or interparticle effects (Fig. 3.14B)[31]. To probe this, we performed Guinier fits using the standard approximation, i.e., linear regression of $\ln I(q)$ versus q^2 within the range $qR_g \lesssim 1.3$. Deviations from linearity at the lowest q support the presence of interparticle interactions, size heterogeneity in both samples. In the 4F/DMPC sample, the low-q range intensity is more strongly affected than in the 4F-P-4F/DMPC sample, consistent with enhanced polydispersity and/or interparticle effects.

Prior experimental work on structurally similar apoA-I mimetic peptides—18A [26] and its tandem variant 18A-P-18A [25] in DMPC nanodiscs reported more polydispersity than in MSP-based nanodiscs, with 18A showing the most pronounced heterogeneity. We observe analogous behavior here. In those studies, size-exclusion chromatography was performed prior to SAXS measurements to reduce polydispersity, suggesting SEC could likewise improve data quality for the 4F/DMPC and 4FP4F/DMPC systems.

We then applied IFT to obtain $P(r)$ and $D_{\max}$. The estimated $D_{\max}$ values are $\approx 27\,\mathrm{nm}$ for 4F/DMPC and $\approx 33\,\mathrm{nm}$ for 4FP4F/DMPC. Accordingly, we interpret $D_{\max}$ as the diameter of the largest nanodisc species present in each sample. Taken together, these analyses indicate notable aggregation and polydispersity.

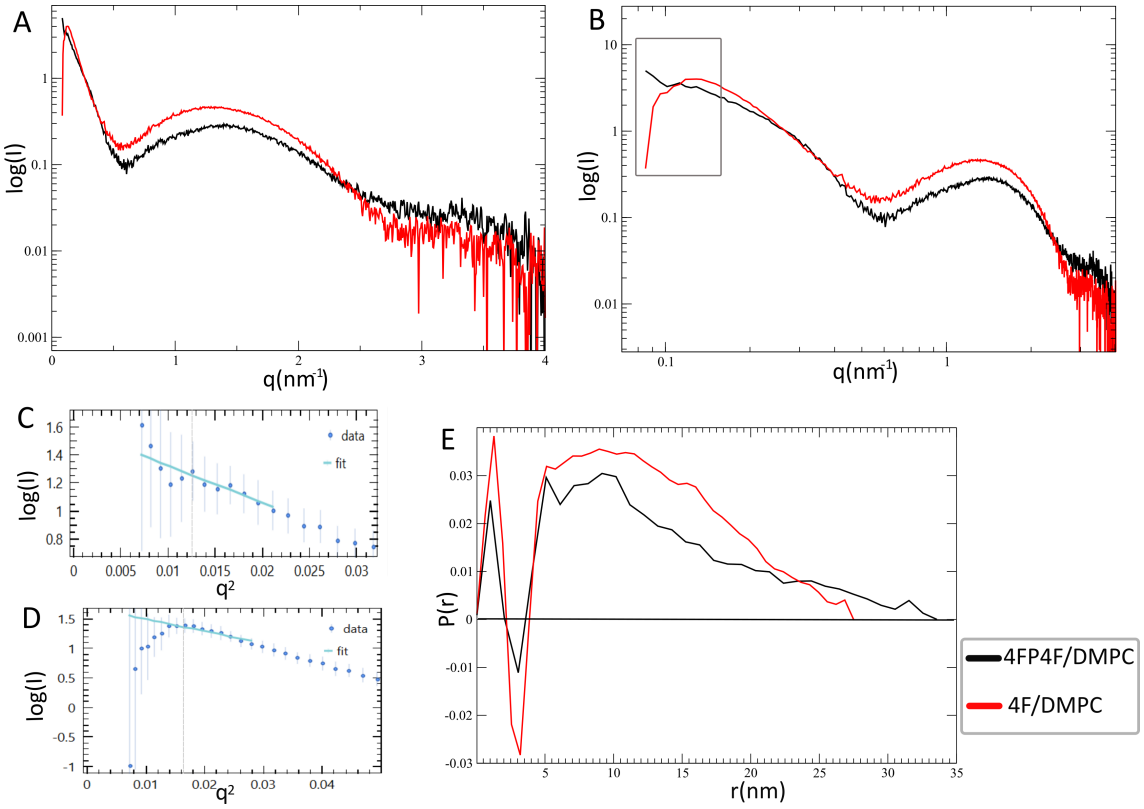

Figure 3.14: Experimental SAXS profiles for 4F/DMPC and 4F-P-4F/DMPC. (A) Intensity plotted as $\log I$ vs. q. (B) Intensity plotted as $\log I$ vs. $\log q$, the gray box highlights the deviation in the SAXS profiles. (C) Guinier analysis for the 4F–P4F/DMPC sample ($\ln I$ vs. q^2). (D) Guinier analysis for the 4F/DMPC sample. (E) Pair-distance distribution functions $P(r)$ obtained by indirect Fourier transform (IFT) of the respective SAXS profiles, used to estimate the maximum particle dimension $D_{\max}$.

3.2.4 Analysis of Polydispersity and Size Effects on SAXS Profiles

Evidence of polydispersity and aggregation in the experimental SAXS data complicates structural interpretation. Experimentally, it's not straightforward to interpret differences in SAXS curves arising from size effects. Hence, in this section, we attempted to rationalize the size effect, and in the following subsection, we attempted to quantify the impact of polydispersity in the experimental SAXS curves.

To rationalize the SAXS curve features, we generated a series of nanodisc models with the peptide-to-lipid ratio systematically varied to tune the nanodisc diameter. The resulting SAXS profiles revealed clear size-dependent trends. As nanodisc diameter increases, the first minimum in the SAXS curve becomes progressively shallower and broader relative to the adjacent maximum, and its position shifts slightly toward lower q values (below $\sim 1\,\mathrm{nm}^{-1}$). For the largest modeled nanodiscs, this minimum exhibits local fluctuations, likely reflecting shape variability or insufficient sampling. These trends were consistently observed for both 4F/DMPC and 4F-P-4F/DMPC systems (Fig. 3.15A, B), highlighting the strong influence of nanodisc size and shape on the low-q scattering features ($q < 1\,\mathrm{nm}^{-1}$).

Global parameters for the 4F/DMPC (B series) and 4F-P-4F/DMPC (C series) systems obtained from both MD trajectories and their corresponding theoretical SAXS curves are summarized in Tables 3.9 and 3.10. For 4F/DMPC, MD model **B11** reproduces the Guinier radius of gyration, $R_g \approx 9.7\,\mathrm{nm}$, in excellent agreement with experiment ($R_g \approx 9.6\,\mathrm{nm}$), but not the maximum particle dimension ($D_{\max} \approx 25.4\,\mathrm{nm}$). In contrast, model **B12** matches the experimental $D_{\max}$ ($D_{\max} \approx 27.3\,\mathrm{nm}$ vs. experimental $\sim 27.5\,\mathrm{nm}$) but not R_g ($R_g \approx 10.3\,\mathrm{nm}$). For 4F–P–4F/DMPC, model **C4** closely matches the experimental R_g ($R_g \approx 10.2\,\mathrm{nm}$) but yields a smaller $D_{\max}$ ($\sim 25.2\,\mathrm{nm}$), whereas model **C5** reproduces the experimental $D_{\max}$ ($\sim 32.5\,\mathrm{nm}$) but not R_g. Taken together, the pairs **B11/B12** and **C4/C5** bracket the experimental observables—one model in each pair captures R_g while the other captures $D_{\max}$, supporting the presence of polydispersity rather than a single, monodisperse size.

The theoretical SAXS curves for **B11/B12** (4F/DMPC) and **C4/C5** (4F–P–4F/DMPC) reproduce the characteristic minimum, maximum, and overall shape of the experimental profiles (Fig. 3.16 A, B). However, they do not match exactly, suggesting that the monodispersed MD models do not fully capture the *in vitro* assemblies.

The resulting discrepancies likely arise from several factors, including the presence of multiple nanodisc sizes, contributions from peptide-lipid aggregates, and insufficient sampling in the simulations. Previous studies on related 18A and 18A-P-18A [25, 26] systems have shown that even after size-exclusion chromatography, a small fraction of aggregates can persist and influence the SAXS signal—particularly near the first minimum—while leaving higher-q regions largely unaffected. In our experiments,

SAXS measurements were performed without SEC, so contributions from aggregates and a broader size distribution are likely to affect the entire scattering profile, exacerbating the mismatch between the experimental and simulated curves. Nevertheless, this analysis clarifies how nanodisc size modulates specific features of the scattering curves.

System	R_g**(MD) [nm]**	R_g**(Guinier Approx) [nm]**	**Average Diameter (MD) [nm]**	$D_{\max}$ **[nm]**
B1	3.0	4.1	9.2	10.0
B2	3.5	4.6	10.2	10.1
B3	4.3	5.4	13.0	13.3
B4	4.4	5.4	13.5	15.1
B5	5.1	6.3	15.0	16.4
B6	5.6	6.6	16.7	18.0
B7	6.1	7.3	17.8	20.0
B8	6.7	7.8	19.7	21.2
B9	7.4	8.5	21.8	23.5
B10	8.0	9.0	23.5	24.1
B11	8.6	9.7	25.3	25.4
B12	9.1	10.3	27.0	27.3
B13	9.8	11.0	29.0	30.5
B14	10.4	11.4	31.0	31.7
B15	11.0	12.1	32.4	32.1
Exp$(4F/DMPC)^*$	N/A	9.6	N/A	27.5

Table 3.9: Summary of size metrics for systems B1 to B15 (4F/DMPC). *MD-derived quantities:* R_g from radius-of-gyration analysis and the average nanodisc diameter from mass–density distributions. *SAXS-derived quantities:* Guinier analysis approximated R_g , and $D_{\max}$ from the pair-distance distribution $P(r)$ obtained by indirect Fourier transform (IFT). The final row lists global parameters derived from the experimental SAXS curve of 4F/DMPC*.

System	R_g**(MD) [nm]**	R_g**(Guinier Approx) [nm]**	**Average Diameter (MD) [nm]**	$D_{\max}$ **[nm]**
C1	3.0	4.6	10.5	10.2
C2	3.9	5.0	12.0	11.5
C3	6.1	7.8	18.1	19.0
C4	8.3	10.2	26.0	26.2
C5	10.5	12.2	31.0	32.5
Exp$(4F-P-4F/DMPC)^*$	N/A	10.4	N/A	33.5

Table 3.10: Summary of size metrics for systems B1 to B15 (4F-P-4F/DMPC). *MD-derived quantities:* R_g from radius-of-gyration analysis and the average nanodisc diameter from mass–density distributions. *SAXS-derived quantities:* Guinier analysis approximated R_g , and $D_{\max}$ from the pair-distance distribution $P(r)$ obtained by indirect Fourier transform (IFT). The final row lists global parameters derived from the experimental SAXS curve of 4F-P-4F/DMPC*.

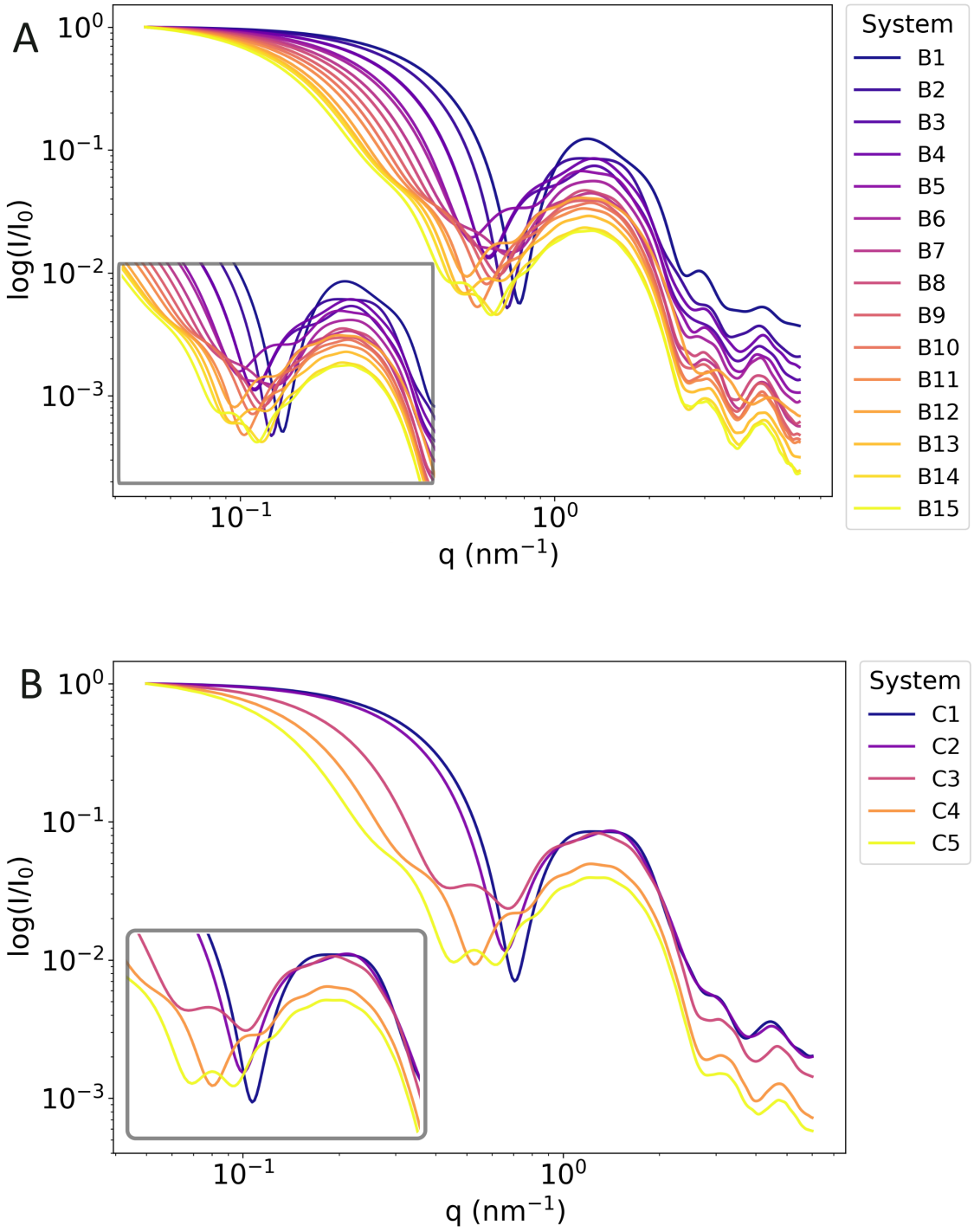

Figure 3.15: Calculated SAXS profiles from MD simulations using GROMACS-SWAXS, plotted as $\log I(q)$ vs. $\log q$. (A) Normalized SAXS curves of the 4F/DMPC systems. (B) Normalized SAXS curves of the 4F-P-4F/DMPC systems. A gradient color scheme is used to highlight differences among the curves.

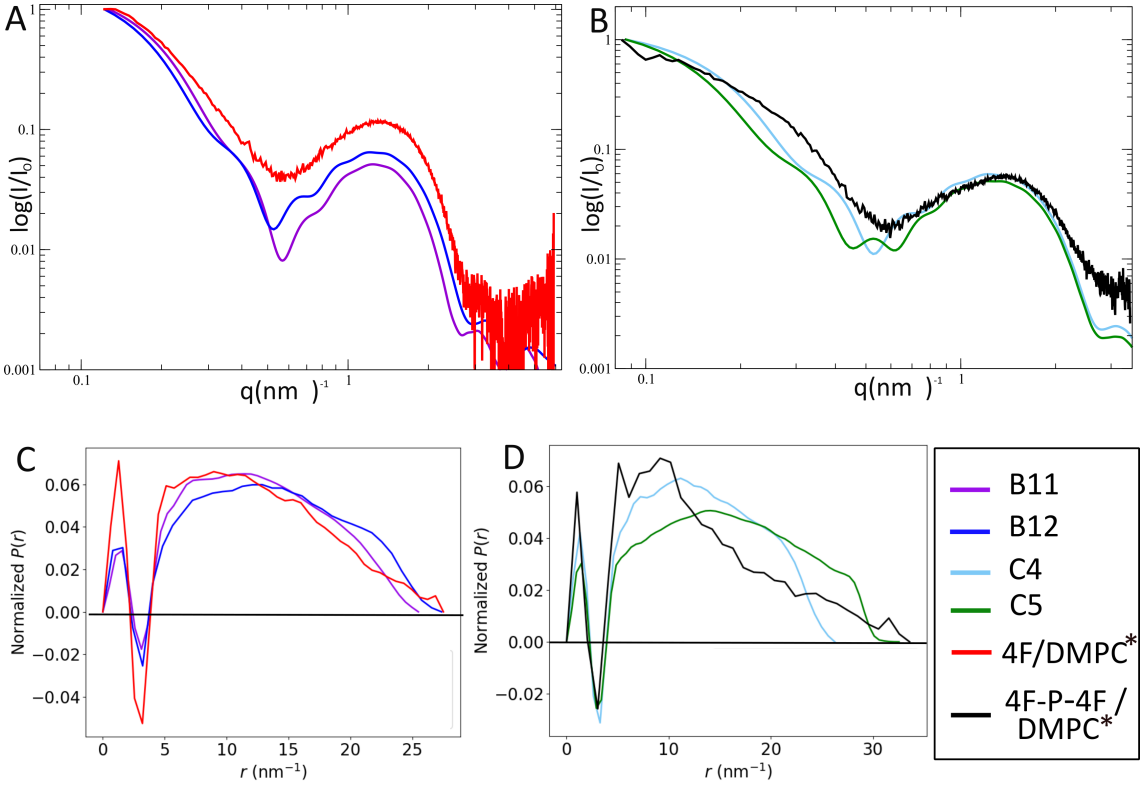

Figure 3.16: Comparison of calculated SAXS curves with experimental data. (A) Calculated SAXS curves for B11 and B12 overlaid with the experimental 4F/DMPC profile. (B) Calculated SAXS curves for C4 and C5 overlaid with the experimental 4F-P-4F/DMPC profile. (C) Pair-distance distribution $P(r)$ for B11, B12, and the experimental 4F/DMPC data. (D) Pair-distance distribution $P(r)$ for C4, C5, and the experimental 4F-P-4F/DMPC data. *Note:* For panels (A) and (B), intensities were normalized as I/I_0; for panels (C) and (D), $P(r)$ curves were area-normalized to enable fair comparison.

3.2.4.1 Assuming Gaussian distribution of sizes to address polydispersity

To quantify the impact of polydispersity on the experimental SAXS curves, we simulated monodisperse 4F/DMPC nanodiscs with a uniformly spaced size range spanning 9–32 nm (B1-B15). We assumed the underlying size distribution to be Gaussian, treating these discrete sizes as a sufficient approximation to constrain the size range (i.e., distribution) that best describes the experiment. For example, taking B11 as the mean (μ) with a spread of ±3, we compute normalized Gaussian weights to all sizes, weight their respective theoretical SAXS profiles, and sum to obtain a single polydisperse curve. Repeating this procedure while treating each size from B1 to B15 as the mean (μ) yields a set of polydisperse theoretical profiles. Fitting these to the experimental curve both evaluates how well the MD-derived models reproduce the data and constrains the size distribution that best describes the experiment. For details of the procedure, see Appendix 5.3.

Scanning across means and standard deviations (SD) shows that size distributions centered on the larger discs (B11–B15) with $\sigma \pm 3$ size bins consistently give reasonable agreement (Appendix Fig. 5.3); broadening beyond about $\sigma \pm 3$ yields similar trends without improvement. Across all cases, the χ^2 values are below 6, indicating that the apparent fit quality is likely overestimated due to large uncertainties in the experimental SAXS curves (Appendix Table 5.1). The χ^2 decreases up to B12 and then rises again; the reasonable fit occurs for $\sigma \pm 3$ bins with the mean at B12 (25.4 nm), giving $\chi^2 \approx 1.2$ (Fig. 3.17). However, the low-q region ($q \lesssim 0.2$) remains systematically misfit in all cases, consistent with aggregation and/or interparticle interactions. Consequently, while this analysis attempts to narrow the plausible size range, it does not uniquely determine a single size distribution (Appendix Fig. 5.3).

Overall, our polydispersity analysis indicates that larger nanodiscs (B11–B15) dominate the experimental SAXS features, and that our MD-simulated models are sufficiently robust to reproduce the SAXS profiles similar to experimental profiles.

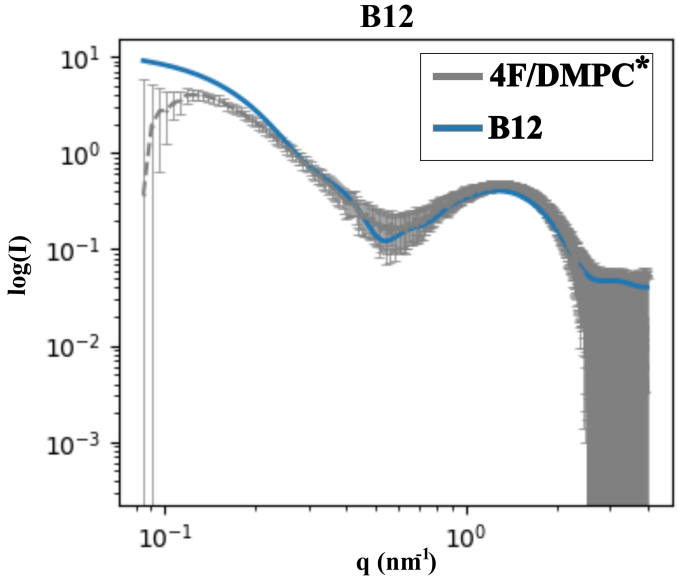

Figure 3.17: **Polydisperse theoretical SAXS profile at B12 (25.4 nm).** The theoretical SAXS profile corresponds to a Gaussian size distribution with mean 25.4 nm (B12) and standard deviation $\sigma = 3$ (size bins). Fitted to the 4F/DMPC* experimental data using a single global scale factor C (Section: 2.3.9.3.) and plotted as a log–log scale as $\log I(q)$ versus $\log q$, with q in nm^{-1}.

3.2.5 Cross-system Comparison of the SAXS Profiles

To further validate our modeling and analysis workflow, we benchmarked small-angle X-ray scattering (SAXS) profiles computed from molecular-dynamics–derived 4F/DMPC nanodisc structures against published size-exclusion chromatography–coupled SAXS data for the closely related apoA-I mimetic system 18A/DMPC [26]. Because the SAXS acquisition was performed immediately after in-line SEC, the reported dataset is predominantly monodisperse, providing an appropriate reference for comparison. Because the two peptides are closely related and both form lipid nanodiscs, and given limitations in our own experimental dataset, this cross-system comparison is informative.

To quantitatively compare the calculated and experimental profiles, we fit the MD-derived theoretical curves to the experimental SAXS data by optimizing a global intensity scale factor C (a constant q-independent background term) to minimize the goodness-of-fit metric χ^2 according to Eq. 2.60, using the experimental uncertainties as weights (Section 2.3.9.3). Applying this fitting protocol, we find that the B1 (4F/DMPC) nanodisc model comprising 16 peptides and 122 DMPC lipids reproduces the experimental profile well, yielding $\chi^2 \approx 20$, comparable to the previously reported monodisperse model [26]. Furthermore, key quantitative parameters extracted from the experimental simple form-factor analysis closely match those computed directly from our MD model of B1 (Table 3.11).

SAXS is primarily sensitive to overall dimensions and low-resolution features; it is not straightforward to distinguish nanodiscs with different peptide scaffolds using SAXS alone, which we have demonstrated in the section: 3.2.2. Hence, our results show that the MD-generated structures capture the overall shape and size consistent with reported experimental data, supporting the robustness of our modeling at the global level. Nevertheless, this cross-system validation builds confidence in the modeling and analysis protocol we employed to further characterize the nanodisc systems.

Parameters	**Experiment**	**MD simulation**
No. of peptides	≈ 17	16
No. of lipids	≈ 122	122
Average bilayer thickness	$\approx 4.2\,\mathrm{nm}$	$3.3\,\mathrm{nm}$
D_{max}	$\approx 10\,\mathrm{nm}$	$\approx 10\,\mathrm{nm}$

Table 3.11: Side-by-side comparison of experimental estimates (18A/DMPC) and MD-derived values (system B1).

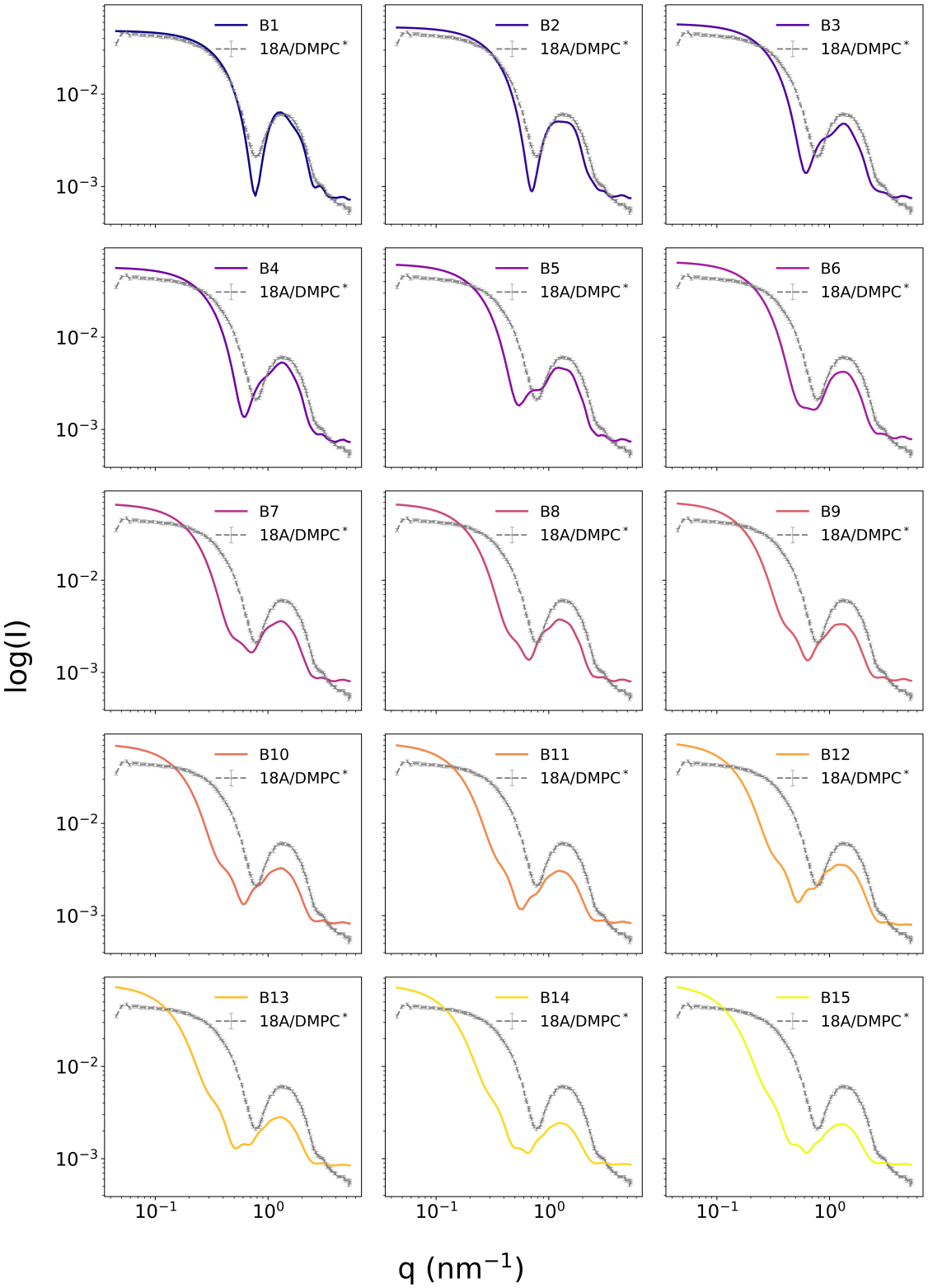

Figure 3.18: Each SAXS curve computed from the 4F/DMPC MD simulations was fitted to the experimental SAXS data of the 18A/DMPC nanodisc and plotted as $\log I(q)$ vs. $\log q$. Experimental SAXS data taken form Midtgaard et al [26]. The fitting procedure is described in Section: 2.3.9.3.

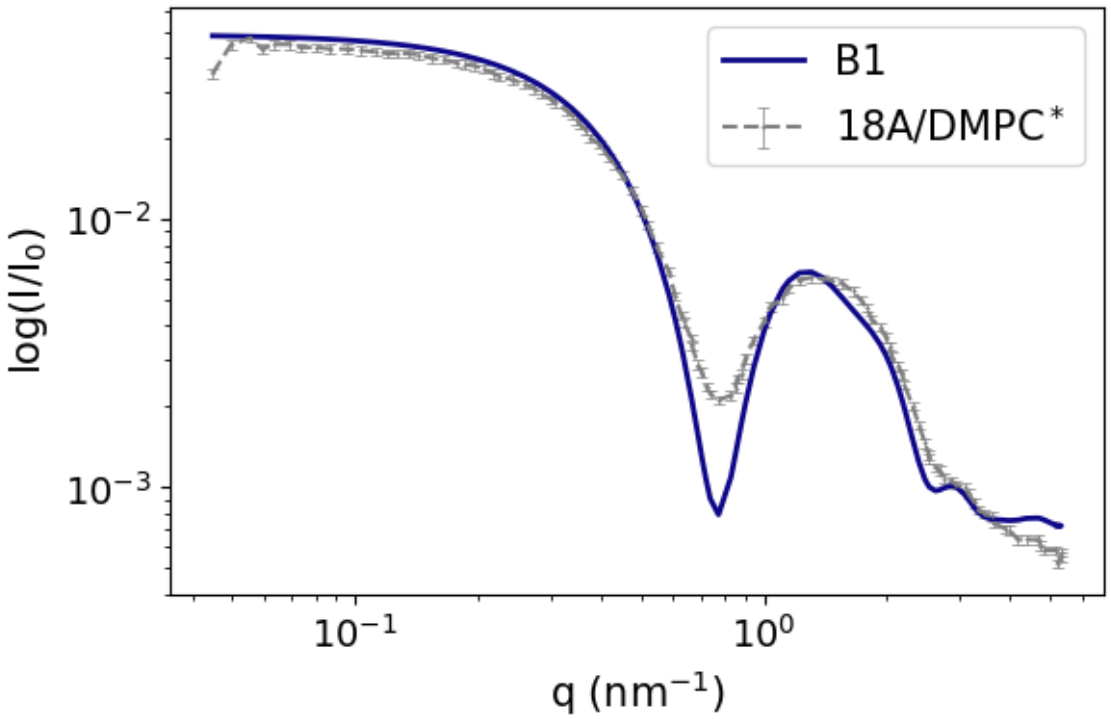

Figure 3.19: Calculated SAXS profile of B1 (4F/DMPC) fitted with the 18A/DMPC* model, plotted as $\log I(q)$ vs. $\log q$ (with q in Å^{-1}). Experimental SAXS data are from Midtgaard et al.[26]. The fitting procedure is described in Section 2.3.9.3.

3.2.6 Discussion

We used MD simulations and SAXS to study the structure of peptide–lipid nanodiscs built with different apoA-I mimetic peptides. By combining these two approaches, we were able to investigate the nanodisc size, shape, overall morphology and how well simulated structures agree with experiments.

Our first goal was to determine whether SAXS can distinguish between nanodiscs formed by different peptides when their overall sizes are similar. By comparing theoretical SAXS curves from MD simulations of 14A, 4F, and 4F–P–4F nanodiscs, we found that the positions of the main scattering minimum and maximum were almost identical across all three systems. These features mainly depend on the disc diameter and bilayer thickness. This shows that SAXS is more sensitive to the global dimensions of the nanodiscs than to specific details of the peptide sequence or arrangement. As a result, using SAXS alone cannot easily distinguish nanodiscs formed by different peptides when their overall size is the same.

Next, we examined the experimental SAXS data for the 4F/DMPC and 4F–P–4F/DMPC samples. The experimental curves showed unusual intensity behavior at low q values, including an upturn and deviations from linearity in the Guinier plots. These patterns suggest the presence of polydispersity and interparticle interactions in the samples. Indirect Fourier transforms of the experimental data also indicated a wide distribution of nanodisc sizes, with $D_{\max}$ around ≈ 27 nm for 4F/DMPC and ≈ 33 nm for 4F–P–4F/DMPC. This means that the solutions likely contain nanodiscs of different sizes, and possibly some aggregates, rather than a single well-defined species. This sample heterogeneity complicates direct comparison between simulation and experiment.

We then explored how nanodisc size affects the SAXS profiles by systematically changing the peptide-to-lipid ratio in simulations. As the nanodisc diameter increased, the first minimum in the SAXS curve became shallower and shifted to lower q values. These size-dependent trends matched the differences we observed between simulated and experimental curves. By comparing experimental R_g and $D_{\max}$ values with those from simulations, we identified the nanodisc sizes that best matched the experimental data. The corresponding SAXS curves reproduced the overall shape of the experimental curves, including the position of minima and maxima. However, the match was not perfect, especially at low q, likely because the experimental samples contain a mixture of different sizes and possibly small aggregates.

Further, we attempted model polydispersity by Gaussian-weighting monodisperse 4F/DMPC nanodiscs spanning 9–32 nm (B1–B15). Scanning mean and width showed that larger discs (B11–B15) best reproduce the characteristic minima, maxima, and overall shape of the experimental SAXS profiles, with the best agreement near B12 (25.4 nm) and $\sigma = 3$ ($\chi^2 \approx 1.2$). Broadening beyond $\sigma = 3$ did not improve fits, and the χ^2 values are below 6 across all cases, indicating that the apparent fit quality is likely overestimated due to large uncertainties in the experimental SAXS curves. A systematic misfit persists at low q ($q \lesssim 0.2$ nm^{-1}), consistent with aggre-

gation and/or interparticle interactions not captured by the models. Overall, the analysis narrows the plausible size range but does not yield a unique distribution, and supports a polydisperse sample biased toward larger nanodiscs (B11–B15).

Finally, we performed a cross-system validation using published SAXS data of 18A/DMPC nanodiscs [26]. Theoretical SAXS curves from system B1 of 4F/DMPC simulations matched the global features of the 18A/DMPC data, as well as earlier-reported quantitative parameters, including the number of peptides and lipids and the bilayer thickness. Our results show that the MD-generated structures capture the overall shape and size consistent with reported experimental data, supporting the robustness of our modeling at the global level. Nevertheless, this preliminary validation builds confidence in the modeling and analysis protocol we employed to further characterize the nanodisc systems.

Overall, these results demonstrate that combining SAXS with MD simulations is a powerful approach for probing the size, shape, and overall morphology of nanodiscs. Because of limitations in our experimental data, we could not match the experimental SAXS curves exactly; a similar mismatch has been observed previously [32, 33]; however, the joint SAXS–MD framework enables direct comparison between models and experiment, supports estimation of nanodisc dimensions, and helps pinpoint sources of discrepancy. Further collaboration between experiment and theory should yield nanodisc models that more closely match the experimental measurements. The models developed here and their future refinements can guide the design of improved scaffold peptides for biomedical applications and the optimization of nanodiscs as platforms for studying membrane proteins.

3.3 4F-P-4F Synthetic HDL Nanodiscs and Biological Assay

In the previous sections, we studied the 14A, 4F, and 4F-P-4F peptide-based nanodiscs using all-atom molecular dynamics simulations and validated the models against ssNMR and SAXS measurements. The close agreement with experiment supports the robustness of our modeling and simulation approach. In collaboration with the biophysical group led by Ruth Prassl (Medical University of Graz, Austria) and the biomedical group led by Günther Marsche (Medical University of Graz), we further examined 4F-P-4F peptide–lipid assemblies, focusing on their structure, dynamics, and potential relevance to inflammatory lung disease. [34–36]. This integrated computational and in vitro/in vivo effort aimed to identify the structural features and key interactions that underlie nanodisc stability and to assess their biological significance (the latter carried out by our collaborators). Portions of this Results section are adapted from our collaborative publication in the Journal of Controlled Release, titled "Peptide-based lipid nanodiscs suppress eosinophil recruitment and chemotaxis." Here, we emphasize structural characterization—drawing on MD simulations and comparisons with circular dichroism (CD) spectra, Transmission electron microscopy (TEM) and Dynamic light Scattering (DLS), where as the details of biological assays will briefly be presented in the following sections; readers are encouraged to refer to the cited article for detailed experimental methods and results [37]. Note: All figures in this part of the results section are adapted from our collaborative paper [37].

3.3.1 Computational Details

Atomistic molecular dynamics models of the apoA-I mimetic 4F-P-4F/DMPC nanodiscs were built (Section 2.2) and simulated using a standardized protocol (Section 2.2.3). In experiments, samples were prepared at a nominal peptide:lipid molar ratio of 1:20 because assays performed by our collaborators showed improved biological efficacy at this ratio [37]. However, the initial bulk ratio does not uniquely determine the stoichiometry of individual nanodiscs: due to polydispersity, each nanodisc particle can deviate from the 1:20 stoichiometry, as reported by others [25, 26, 38]. Accordingly, in our 4F-P-4F/DMPC models, we varied the peptide:lipid ratio to obtain nanodisc diameters within the observed range using TEM and DLS by our collaborators, and this observed range is consistent with prior reports on apolipoprotein A-I mimetic nanodisc assemblies [25, 26, 38]. The same protocol was applied to simulations of the peptides in aqueous solution (Section: 2.2.3). System compositions and simulation parameters are summarized in Table 3.12. All simulations were performed at 30°C.

To facilitate direct comparison between simulations and experiment, far-UV CD spectra were computed from the MD trajectories. For nanodisc systems, peptide

configurations were extracted every 10 ns from the final 100 ns of each production run. For peptides-only simulations, snapshots were taken every 5 ns over the final 100 ns. The resulting coordinate sets (PDB format) were submitted to the PDBMD2CD web server [39], which predicts CD spectra from atomic structures using an empirically derived mapping. From the predicted spectra, the mean residue ellipticity at 222 nm , $[\theta]_{222}$, was extracted, and the fractional α-helicity was computed using Eq. 3.5; helicity values are reported as $100 \times f_H$ and compared directly with CD-derived experimental estimates [40, 41].

$$\Delta\varepsilon(\lambda) \;=\; \frac{[\theta](\lambda)}{3298} \tag{3.4}$$

where $\Delta\varepsilon$ is the molar circular dichroism ($\mathrm{M^{-1}\,cm^{-1}}$), $[\theta]$ is the molar ellipticity ($\mathrm{deg\,cm^2\,dmol^{-1}}$), and 3298 is a unit-conversion constant.

$$f_H \;=\; \frac{[\theta]_{222} - 3000}{-36000 - 3000}, \qquad \alpha\mathrm{Helix}(\%) \;=\; 100\, f_H \tag{3.5}$$

where $[\theta]_{222}$ is the *mean-residue* molar ellipticity at 222 nm ($\mathrm{deg\,cm^2\,dmol^{-1}\,res^{-1}}$); $+3000$ and -36000 are the random-coil baseline and helical reference, respectively.

System	No of Peptides	No of DMPC	peptide:lipid	Total no of atoms	Simulation Time (ns)
A	10	250	1:25	543265	1000
B	18	734	1:40	1748831	300
C	28	1434	1:50	3692066	200
D	1	0	N/A	55745	500

Table 3.12: Simulation system details for MD studies of DMPC bilayer patches stabilized by 4F–P–4F peptides. Reported are the numbers of peptides, DMPC lipids, total atoms, peptide to lipid ratio and production simulation time. Simulations were conducted at 30°C.

3.3.2 Characteriszation of 4F-P-4F Nanodiscs

3.3.2.1 Rationale and nanodisc construction

Previous studies have indicated that peptides that effectively stabilize these discoidal lipid bilayers, mimicking nHDL-like particles, are essential for sHDL functionality [9, 42]. To test this hypothesis on 4F-P-4F based sHDL, we constructed peptide-lipid (4F-P-4F/DMPC) complexes informed by prior solid-state NMR data on structurally related apolipoprotein mimetic peptides (14A, 18A, 4F peptide) [1, 21, 22], given the lack of solid-state NMR data regarding the orientation of 4F-P-4F.

3.3.2.2 Comparison of MD simulation and experiment CD spectra

We analyzed the helicity of the isolated 4F-P-4F peptide and 4F-P-4F/DMPC (sHDL), comparing MD-simulated and experimental CD spectra to determine their secondary structure compositions. The percentage of helix was calculated from the mean residual ellipticity at 222nm using the equation described in section 3.3.1 and compared in Table: 3.13. Both simulated and experimental spectra consistently exhibit canonical α-helical signatures, with pronounced minima at 208 and 222 nm [41] (Fig. 3.20). The MD-derived CD spectra capture these key features, and simulation-derived secondary-structure metrics agree well with experiment. Across all systems, the α-helical content is 63–77%, demonstrating that the peptides are highly helical in both their free and lipidated form.

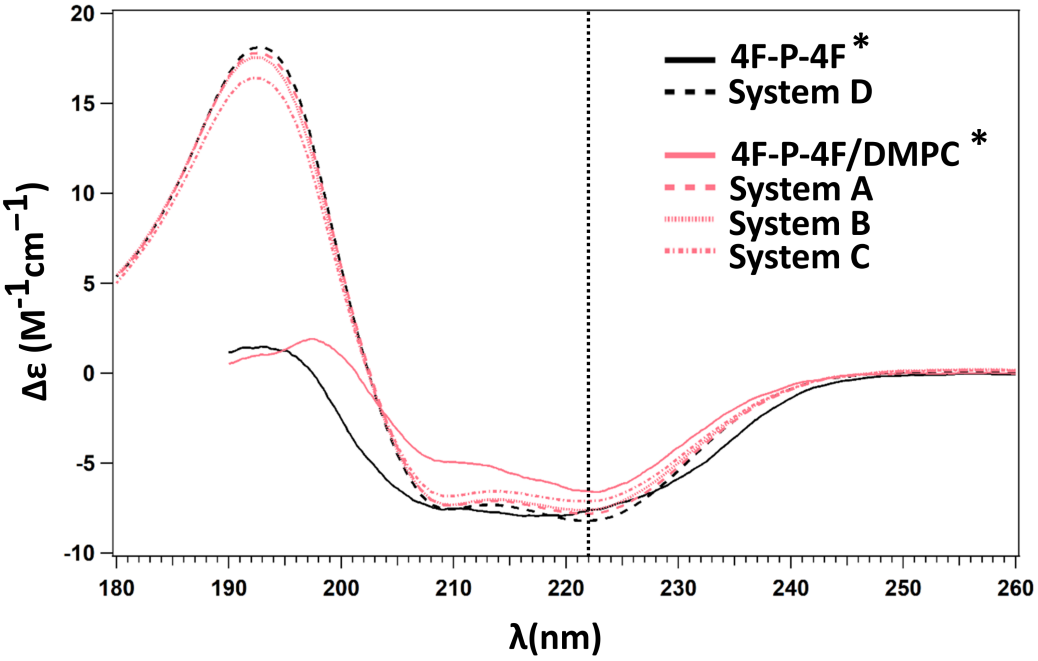

Figure 3.20: Far UV CD spectra comparing the structural characteristics of the sHDL formulation and the non-lipidated 4F-P-4F peptide. Both experimental spectra and MD-derived spectra are shown. The mean-residue molar ellipticity at 222 nm, $[\theta]_{222}$, was obtained by converting the molar circular dichroism spectra $\Delta\varepsilon(\lambda)$ using $[\theta] = 3298\,\Delta\varepsilon$, and the percent α-helicity was computed using Eq. 3.5. 4F-P-4F* and 4F-P-4F/DMPC* are experimental curves, and the remaining systems are from MD-derived spectra.

3.3.2.3 Lipid-peptide Interactions

MD simulations of the sHDL nanodiscs yielded average diameters of 11.7 nm, 18.0 nm, and 25.6 nm, respectively (Fig: 3.21). These models remained stable throughout

Sample	$[\theta]_{222\,\mathrm{nm}}$	Helix (%)
4F-P-4F *	−25174	72
4F-P-4F/DMPC *	−21643	63
System A	−25777	74
System B	−25081	72
System C	−23480	68
System D	−27051	77

Table 3.13: Percent α-helicity from mean-residue molar ellipticity at 222 nm, $[\theta]_{222}$ (units: $\mathrm{deg\,cm^2\,dmol^{-1}\,res^{-1}}$), computed using the baseline-corrected relation in Eq. 3.5. Entries marked with * (4F-P-4F* and 4F-P-4F/DMPC*) are experimental measurements; the remaining systems are from MD-derived spectra.

the simulations, owing to salt-bridge interactions between the peptide's polar amino acids and the DMPC lipid head groups. Specifically, lysine-phosphate interactions outnumbered choline-glutamic acid interactions across all systems. The hydrophobic faces of the 4F-P4F dimers are consistently oriented toward the DMPC hydrophobic tails, with their hydrophilic surfaces exposed to the aqueous phase. Saltbridge interactions with the lipid head groups anchored the peptides in a belt-like arrangement around the membrane normal, stabilizing the discoidal bilayer structure. MD simulations revealed that polar amino acids at the interface between hydrophobic peptide residues and lipid headgroups play a pivotal role in stabilizing the lipid bilayer. These interactions enable peptides to effectively cover the lipid hydrophobic tails, maintaining structural integrity throughout the simulation across nanodiscs of varying sizes. Combined atomistic simulations and high-resolution experimental characterizations demonstrate the structural stability and speculate the robust functional potential of the synthesized 4F-P-4F/DMPC (sHDL) formulations.

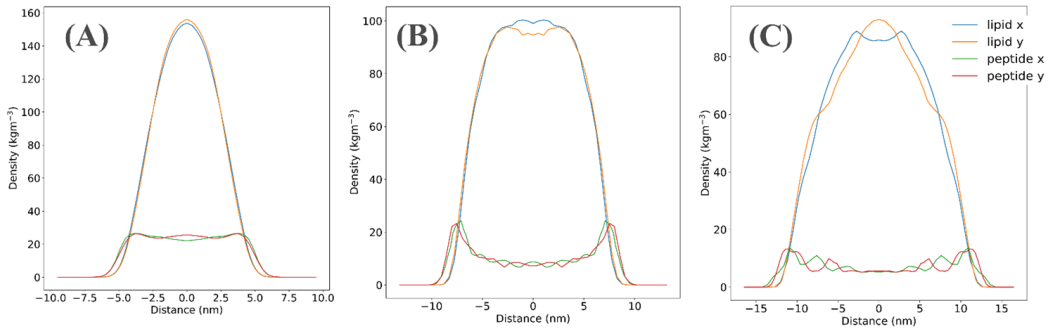

Figure 3.21: Mass density distribution profiles of 4F-P-4F nanodiscs.(A): System A, and (B): System B, (C): System C. The plots show lipid and peptide mass density distributions along the x and y axes. "Lipid x" and "Lipid y" denote lipid densities along the respective axes, while "Peptide x" and "Peptide y" show peptide mass densities (see section: 2.3.3). These profiles were used to calculate the average nanodisc diameter for each system.

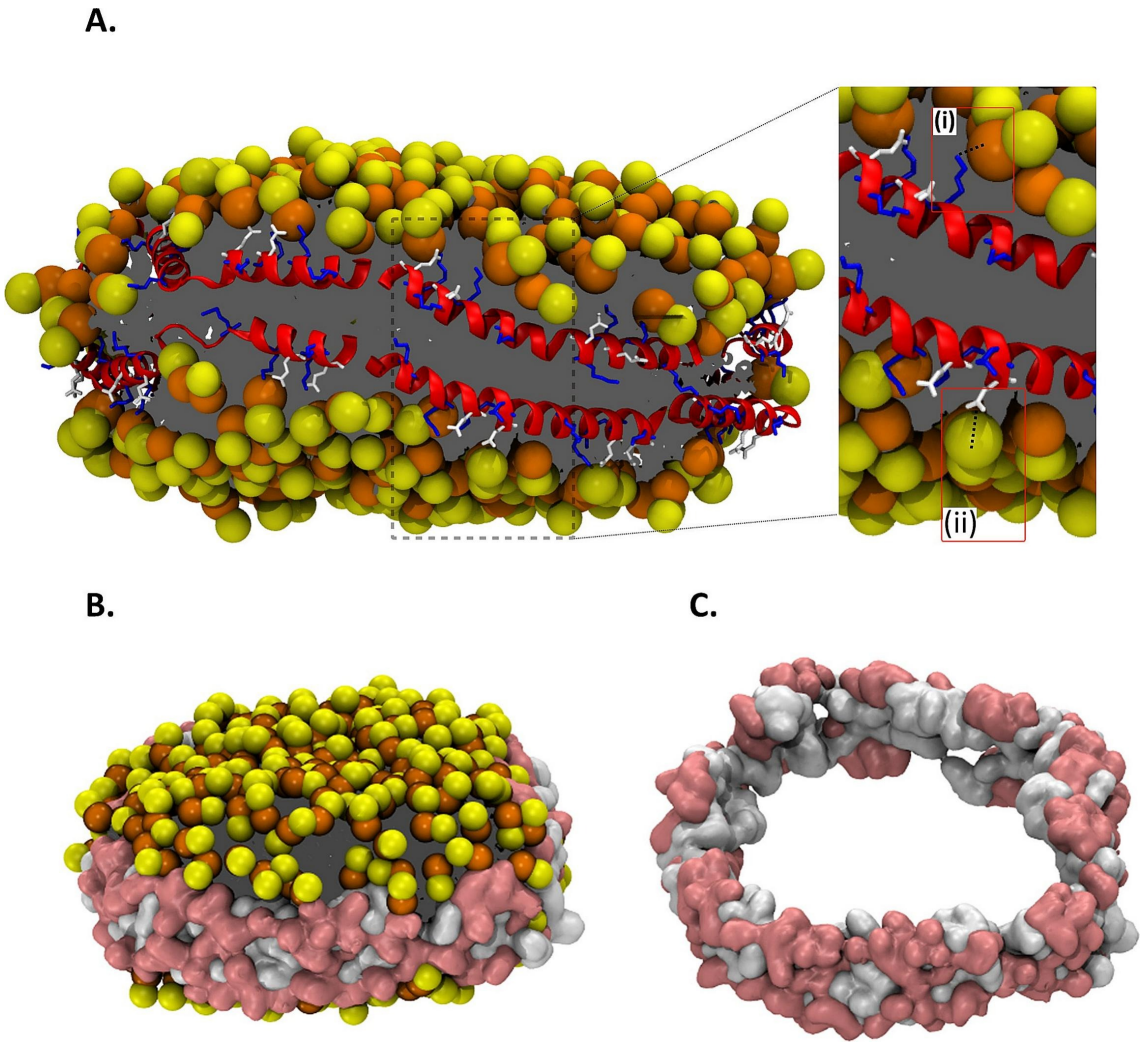

Figure 3.22: Molecular dynamics simulation of sHDL nanodiscs. A. Snapshot of system A (4F-P-4F/DMPC) from the MD trajectory illustrating peptide–lipid salt bridges: (i) a lysine–phosphate interaction between the lysine amine nitrogen (blue) and the lipid phosphate phosphorus (orange); (ii) a glutamate–choline interaction between the glutamate carboxylate (white) and the choline nitrogen of the lipid headgroup (yellow). B–C. Alternative orientations highlighting hydrophobic (white) and hydrophilic (pink) residues of the 4F-P-4F dimers, emphasizing the amphipathic side-chain patterning and their positioning relative to the lipid core and surrounding solvent.

System	no of salt bridges per peptide	
	Lys-Phos	Glu-Choline
A	2.69	0.60
B	2.98	0.75
C	2.85	0.82

Table 3.14: Average number of salt bridges formed between the amino groups of the lysine residues (K4, K9, K13, K15, K23, K28, K32, K34) of the 4F-P-4F peptides and the phosphorus of the phosphate groups in the DMPC lipids, or between the carbon of the carboxyl groups of the glutamate residues (E12, E16, E31, E35) of the 4F-P-4F peptides and the nitrogen of the choline groups in the DMPC molecules. Salt bridges were considered when the distances between the interacting groups were 4.6 Å or 6 Å. The averages were calculated over the last 50 ns of each simulation for the three systems, normalized by the number of 4F-P-4F peptides. The Cutoff distances for counting salt bridges were obtained from radial distribution functions.

3.3.3 sHDL Structural Relation to Cholesterol Efflux

Despite comparable α-helical content in free 4F-P-4F and in its nanodisc form (sHDL), their functional outcomes differ markedly. In human eosinophils, sHDL nanodiscs produce a strong reduction in cellular cholesterol, whereas free 4F-P-4F elicits only minimal efflux (Fig. 3.23). These observations support the hypothesis [9, 42] that amphipathic helices must be presented in a lipidated, discoidal architecture—structurally similar to nHDL—to drive efficient cholesterol removal. In the assembled particle, the peptides interact with phospholipid headgroups and remain structurally organized in belt-like arrangements, which limits peptide–peptide aggregation and facilitates cholesterol efflux; by contrast, the free peptide likely lacks this supramolecular organization and shows minimal activity. Several previous studies report that free amphipathic peptides tend to aggregate and behave unpredictably in biological environments [42, 43]. Consistent with this, our MD simulations indicate that peptides around the nanodisc interact with phospholipid headgroups and remain associated throughout the simulation across all three nanodisc sizes, and TEM images (Fig. 1C in [37]) from our collaborators clearly show nanodisc formation. To clarify how sHDL particles mediate efficient cholesterol efflux, we need to further investigate their interactions with ABCA1, the initial step in reverse cholesterol transport (see section: 1.2.1). To our knowledge, simulations of peptide-based nanodiscs engaging ABCA1 have not yet been reported and represent an important avenue for future work.

3.3.4 Discussion

In this work, we combined MD simulations with biophysical and biomedical experiments to attempt to relate the structure of 4F-P-4F/DMPC nanodiscs to their function. We first modeled nanodiscs with diameters matched to those observed by

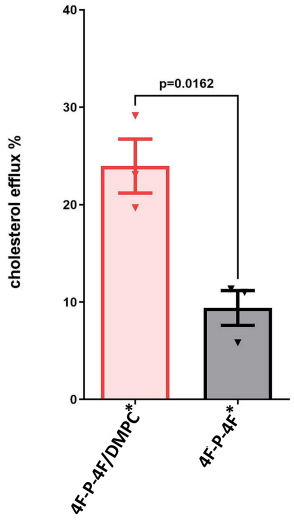

Figure 3.23: ^{3}H-cholesterol efflux from isolated human eosinophils, expressed as the percentage of total ^{3}H-cholesterol released following treatment with sHDL (25 µg/mL) or 4F-P-4F (25 µg/mL). Data are presented as mean ± SEM from three independent experiments; statistical significance was assessed using Student's t-test. Data adapted from our collaborative study [37].

TEM and DLS. CD spectra computed from the MD ensembles agreed with experimental measurements for both the peptide in solution and the lipidated nanodisc state, indicating comparable overall helicity across conditions. MD further revealed key interactions that are difficult to resolve experimentally: peptide–lipid contacts that stabilize the discoidal bilayer. In particular, Lys–phosphate contacts were more frequent than Glu–choline contacts. Notably, peptides remained continuously associated with the nanodisc edge across all modeled sizes, consistent with our earlier simulations presented in the previous results sections 3. Because our build protocol enforces an appropriate peptide: lipid ratio and resolves peptide–lipid steric clashes, it is practical to insert a pre-equilibrated lipid bilayer within the peptide ring—an approach closely aligned with Tieleman's protocol for apoA-I assembly/MDS protocol [14] (see Section: 2.2).

Previous studies suggest that stable discoidal, nHDL–like particles are essential for sHDL functionality [9, 42]. Our data support this view: amphipathic helices must be lipidated and arranged in a discoidal geometry to drive efficient cholesterol efflux. In contrast, lipid-free peptide showed no significant cholesterol efflux from human eosinophils, and as reported by other studies, free amphipathic peptides tend to aggregate and behave unpredictably in biological environment [42, 43].

Complementary biological assays (performed by collaborators, not shown in this thesis). As part of the broader collaboration, colleagues conducted eosinophil chemotaxis. Eosinophils' chemotaxis toward eotaxin-1 and prostaglandin D_2 significantly amplifies the inflammatory response [35, 36] (a signal elevated in chronic airway inflammation such as asthma); their accumulation at the airway epithelium promotes

tissue damage, mucus hypersecretion, and airway hyperreactivity. We found that 4F-P-4F sHDL potently inhibits eotaxin-driven eosinophil migration in vitro. Importantly, pharmacological blockade of HDL receptors ABCA1 and SR-BI abolished this inhibitory effect, indicating that sHDL acts through these receptors. A plausible mechanism is that sHDL engages ABCA1/SR-BI to modulate membrane cholesterol distribution and downstream signaling pathways required for chemotaxis, thereby limiting eosinophil migration. These findings motivate exploration of sHDL-based interventions for pulmonary inflammatory diseases.

To clarify how sHDL particles mediate efficient cholesterol efflux at the molecular level, future work should explicitly model peptide-based nanodiscs interacting with ABCA1—the initiating step of reverse cholesterol transport (see Section: 1.2.1). To our knowledge, atomistic or coarse-grained simulations of 4F-P-4F nanodiscs bound to ABCA1 have not yet been reported and represent an important next step.

Overall, our results connect nanodisc structure stabilized by specific peptide–lipid interactions and preserved peptide integrity to functional outcomes in cholesterol efflux in human eosinophil. This structure–function linkage supports and extends the prevailing hypothesis that nHDL–like discoidal architecture is a prerequisite for sHDL activity.

References

[1] Evgeniy S Salnikov, GM Anantharamaiah, and Burkhard Bechinger. Supramolecular organization of apolipoprotein-ai-derived peptides within disc-like arrangements. *Biophysical journal*, 115(3):467–477, 2018.

[2] Burkhard Bechinger and Evgeniy S Salnikov. The membrane interactions of antimicrobial peptides revealed by solid-state nmr spectroscopy. *Chemistry and physics of lipids*, 165(3):282–301, 2012.

[3] Trivikram R Molugu, Soohyun Lee, and Michael F Brown. Concepts and methods of solid-state nmr spectroscopy applied to biomembranes. *Chemical reviews*, 117(19):12087–12132, 2017.

[4] Burkhard Bechinger, Christopher Aisenbrey, and Philippe Bertani. The alignment, structure and dynamics of membrane-associated polypeptides by solid-state nmr spectroscopy. *Biochimica et Biophysica Acta (BBA)-Biomembranes*, 1666(1-2):190–204, 2004.

[5] Sébastien Côté, Vincent Binette, Evgeniy S Salnikov, Burkhard Bechinger, and Normand Mousseau. Probing the huntingtin 1-17 membrane anchor on a phospholipid bilayer by using all-atom simulations. *Biophysical Journal*, 108(5): 1187–1198, 2015.

[6] Santi Esteban-Martín and Jesús Salgado. The dynamic orientation of membrane-bound peptides: bridging simulations and experiments. *Biophysical journal*, 93(12):4278–4288, 2007.

[7] Lei Shi, Alessandro Cembran, Jiali Gao, and Gianluigi Veglia. Tilt and azimuthal angles of a transmembrane peptide: a comparison between molecular dynamics calculations and solid-state nmr data of sarcolipin in lipid membranes. *Biophysical journal*, 96(9):3648–3662, 2009.

[8] Christie G Brouillette, James L Jones, Thien C Ng, Henri Kercret, B Hong Chung, and Jere P Segrest. Structural studies of apolipoprotein ai/phosphatidylcholine recombinants by high-field proton nmr, nondenaturing gradient gel electrophoresis, and electron microscopy. *Biochemistry*, 23(2):359–367, 1984.

[9] Rafique M Islam, Mohsen Pourmousa, Denis Sviridov, Scott M Gordon, Edward B Neufeld, Lita A Freeman, B Scott Perrin Jr, Richard W Pastor, and Alan T Remaley. Structural properties of apolipoprotein ai mimetic peptides that promote abca1-dependent cholesterol efflux. *Scientific Reports*, 8(1):2956, 2018.

[10] Christopher Sheldahl and Stephen C Harvey. Molecular dynamics on a model for nascent high-density lipoprotein: role of salt bridges. *Biophysical journal*, 76(3):1190–1198, 1999.

[11] Karsten Mörs, Christian Roos, Frank Scholz, Josef Wachtveitl, Volker Dötsch, Frank Bernhard, and Clemens Glaubitz. Modified lipid and protein dynamics in nanodiscs. *Biochimica et Biophysica Acta (BBA)-Biomembranes*, 1828(4): 1222–1229, 2013.

[12] Denis Martinez, Marion Decossas, Julia Kowal, Lukas Frey, Henning Stahlberg, Erick J Dufourc, Roland Riek, Birgit Habenstein, Stefan Bibow, and Antoine Loquet. Lipid internal dynamics probed in nanodiscs. *ChemPhysChem*, 18(19): 2651–2657, 2017.

[13] Ananya Debnath and Lars V Schafer. Structure and dynamics of phospholipid nanodiscs from all-atom and coarse-grained simulations. *The Journal of Physical Chemistry B*, 119(23):6991–7002, 2015.

[14] Iwona Siuda and D Peter Tieleman. Molecular models of nanodiscs. *Journal of chemical theory and computation*, 11(10):4923–4932, 2015.

[15] Sang Ho Park, Sabrina Berkamp, Gabriel A Cook, Michelle K Chan, Hector Viadiu, and Stanley J Opella. Nanodiscs versus macrodiscs for nmr of membrane proteins. *Biochemistry*, 50(42):8983–8985, 2011.

[16] Piotr Stepien, Bozena Augustyn, Chetan Poojari, Wojciech Galan, Agnieszka Polit, Ilpo Vattulainen, Anna Wisnieska-Becker, and Tomasz Rog. Complexity of seemingly simple lipid nanodiscs. *Biochimica et Biophysica Acta (BBA)-Biomembranes*, 1862(11):183420, 2020.

[17] Tone Bengtsen, Viktor L Holm, Lisbeth Ravnkilde Kjølbye, Søren R Midtgaard, Nicolai Tidemand Johansen, Giulio Tesei, Sandro Bottaro, Birgit Schiøtt, Lise Arleth, and Kresten Lindorff-Larsen. Structure and dynamics of a nanodisc by integrating nmr, saxs and sans experiments with molecular dynamics simulations. *Elife*, 9:e56518, 2020.

[18] Masakazu Miyazaki, Yoko Tajima, Tetsurou Handa, and Minoru Nakano. Static and dynamic characterization of nanodiscs with apolipoprotein ai and its model peptide. *The Journal of Physical Chemistry B*, 114(38):12376–12382, 2010.

[19] Chiharu Anada, Keisuke Ikeda, Ayako Egawa, Toshimichi Fujiwara, Hiroyuki Nakao, and Minoru Nakano. Temperature-and composition-dependent conformational transitions of amphipathic peptide–phospholipid nanodiscs. *Journal of Colloid and Interface Science*, 588:522–530, 2021.

[20] Minoru Nakano, Masakazu Fukuda, Takayuki Kudo, Masakazu Miyazaki, Yusuke Wada, Naoya Matsuzaki, Hitoshi Endo, and Tetsurou Handa. Static and dynamic properties of phospholipid bilayer nanodiscs. *Journal of the American Chemical Society*, 131(23):8308–8312, 2009.

[21] Vinod K Mishra, GM Anantharamaiah, Jere P Segrest, Mayakonda N Palgunachari, Manjula Chaddha, SW Simon Sham, and N Rama Krishna. Association of a model class a (apolipoprotein) amphipathic α helical peptide with lipid: High resolution nmr studies of peptide· lipid discoidal complexes. *Journal of Biological Chemistry*, 281(10):6511–6519, 2006.

[22] Vinod K Mishra, Mayakonda N Palgunachari, N Rama Krishna, John Glushka, Jere P Segrest, and GM Anantharamaiah. Effect of leucine to phenylalanine substitution on the nonpolar face of a class a amphipathic helical peptide on its interaction with lipid: high resolution solution nmr studies of 4f-dimyristoylphosphatidylcholine discoidal complex. *Journal of Biological Chemistry*, 283(49):34393–34402, 2008.

[23] Christopher J Knight and Jochen S Hub. Waxsis: a web server for the calculation of saxs/waxs curves based on explicit-solvent molecular dynamics. *Nucleic acids research*, 43(W1):W225–W230, 2015.

[24] Nicholas Skar-Gislinge and Lise Arleth. Small-angle scattering from phospholipid nanodiscs: derivation and refinement of a molecular constrained analytical model form factor. *Physical Chemistry Chemical Physics*, 13(8):3161–3170, 2011.

[25] Andreas N Larsen, Kasper K Sørensen, Nicolai T Johansen, Anne Martel, Jacob JK Kirkensgaard, Knud J Jensen, Lise Arleth, and Søren Roi Midtgaard. Dimeric peptides with three different linkers self-assemble with phospholipids to form peptide nanodiscs that stabilize membrane proteins. *Soft Matter*, 12 (27):5937–5949, 2016.

[26] Søren Roi Midtgaard, Martin Cramer Pedersen, Jacob Judas Kain Kirkensgaard, Kasper Kildegaard Sørensen, Kell Mortensen, Knud J Jensen, and Lise Arleth. Self-assembling peptides form nanodiscs that stabilize membrane proteins. *Soft matter*, 10(5):738–752, 2014.

[27] Vito Graziano, Lisa Miller, and Lin Yang. Interpretation of solution scattering data from lipid nanodiscs. *Applied Crystallography*, 51(1):157–166, 2018.

[28] OTTO Glatter. A new method for the evaluation of small-angle scattering data. *Applied Crystallography*, 10(5):415–421, 1977.

[29] André Guinier. La diffraction des rayons x aux tres petits angles: applications a l'etude de phenomenes ultramicroscopiques. In *Annales de physique*, number 11. Sér. 12, pages 161–237. EDP Sciences, 1939.

[30] Maxim V Petoukhov, Peter V Konarev, Alexey G Kikhney, and Dmitri I Svergun. Atsas 2.1–towards automated and web-supported small-angle scattering data analysis. *Applied crystallography*, 40(s1):s223–s228, 2007.

[31] Christopher D Putnam, Michal Hammel, Greg L Hura, and John A Tainer. X-ray solution scattering (saxs) combined with crystallography and computation: defining accurate macromolecular structures, conformations and assemblies in solution. *Quarterly reviews of biophysics*, 40(3):191–285, 2007.

[32] Amy Y Shih, Ilia G Denisov, James C Phillips, Stephen G Sligar, and Klaus Schulten. Molecular dynamics simulations of discoidal bilayers assembled from truncated human lipoproteins. *Biophysical journal*, 88(1):548–556, 2005.

[33] Amy Y Shih, Anton Arkhipov, Lydia Freddolino, Stephen G Sligar, and Klaus Schulten. Assembly of lipids and proteins into lipoprotein particles, 2007.

[34] Malgorzata Wygrecka, Ioannis Alexopoulos, Daniel P Potaczek, and Liliana Schaefer. Diverse functions of apolipoprotein ai in lung fibrosis. *American Journal of Physiology-Cell Physiology*, 324(2):C438–C446, 2023.

[35] Petra Schratl, Eva M Sturm, Julia F Royer, Gunter J Sturm, Irmgard T Lippe, Bernhard A Peskar, and Akos Heinemann. Hierarchy of eosinophil chemoattractants: role of p38 mitogen-activated protein kinase. *European journal of immunology*, 36(9):2401–2409, 2006.

[36] Xianglan Yao, Michael P Vitek, Alan T Remaley, and Stewart J Levine. Apolipoprotein mimetic peptides: a new approach for the treatment of asthma. *Frontiers in pharmacology*, 3:37, 2012.

[37] Alankrita Rani, Denys Balandin, Rohith Ravi, Julia Teppan, Ivan Vidakovic, Melanie Kienzl, Thomas Bärnthaler, Michael Holzer, Lamija Zijadic, Akos Heinemann, et al. Peptide-based lipid nanodiscs suppress eosinophil recruitment and chemotaxis. *Journal of Controlled Release*, page 114060, 2025.

[38] Yannan Zhao, Tomohiro Imura, Luke J Leman, Linda K Curtiss, Bruce E Maryanoff, and M Reza Ghadiri. Mimicry of high-density lipoprotein: functional peptide–lipid nanoparticles based on multivalent peptide constructs. *Journal of the American Chemical Society*, 135(36):13414–13424, 2013.

[39] Elliot D Drew and Robert W Janes. Pdbmd2cd: providing predicted protein circular dichroism spectra from multiple molecular dynamics-generated protein structures. *Nucleic acids research*, 48(W1):W17–W24, 2020.

[40] Yee-Hsiung Chen, Jen Tsi Yang, and Hugo M Martinez. Determination of the secondary structures of proteins by circular dichroism and optical rotatory dispersion. *Biochemistry*, 11(22):4120–4131, 1972.

[41] Joel D Morrisett, Joshua SK David, Henry J Pownall, and Antonio M Gotto Jr. Interaction of an apolipoprotein (apolp-alanine) with phosphatidylcholine. *Biochemistry*, 12(7):1290–1299, 1973.

[42] Jie Tang, Dan Li, Lindsey Drake, Wenmin Yuan, Sara Deschaine, Emily E Morin, Rose Ackermann, Karl Olsen, David E Smith, and Anna Schwendeman. Influence of route of administration and lipidation of apolipoprotein ai peptide on pharmacokinetics and cholesterol mobilization. *Journal of lipid research*, 58 (1):124–136, 2017.

[43] Wilissa D'Souza, John A Stonik, Andrew Murphy, Steven J Demosky, Amar A Sethi, Xiao L Moore, Jaye Chin-Dusting, Alan T Remaley, and Dmitri Sviridov. Structure/function relationships of apolipoprotein ai mimetic peptides: implications for antiatherogenic activities of high-density lipoprotein. *Circulation research*, 107(2):217–227, 2010.

4 Conclusion and Perspectives

4.1 Conclusion

Apolipoprotein A-I (apoA-I) mimetic peptides that assemble with phospholipids into lipid-poor, HDL-like nanodiscs have emerged as versatile bioinspired nanoparticle platforms for pharmacological intervention in cardiovascular [1] and inflammatory diseases [2, 3]. In addition, peptide-based nanodiscs provide a versatile platform for the structural and functional characterization of membrane proteins [4]. Despite extensive research, fundamental aspects of their physicochemical behavior, molecular organization, size, structure, dynamics, and, critically, how these parameters modulate biological activity remain inadequately explored.

In this thesis, we set out to elucidate the structure and dynamics of peptide–lipid nanodiscs and to identify the key interactions that stabilize these assemblies using all-atom molecular dynamics simulations and validating our models against experimental observables. We concentrated on clinically relevant derivatives of the 18A class of apoA-I–mimetic peptides, specifically 14A, 4F, and 4F-P-4F, which have attracted sustained biomedical interest. A prerequisite for any mechanistic analysis is a reliable structural model. Whereas MSP–based nanodiscs are routinely constructed (e.g., via CHARMM-GUI [5]), equivalent, generally accepted starting models for peptide-based nanodiscs are not straightforward to obtain. Guided by ssNMR work of 14A [6], 18A [7], and other related apoA-1 mimetic peptides [8], we assembled peptides into antiparallel dimers arranged around a discoidal DMPC bilayer such that charged residues face outward toward the aqueous phase.

We first modeled and validated a 14A/DMPC nanodisc model, leveraging ssNMR measurements [6] from our collaborators to probe local peptide orientation and peptide–lipid contacts while simultaneously validating our nanodisc-building workflow. To assess model fidelity, we back-calculated Solid-state NMR observables, namely ^{15}N chemical shifts and ^{2}H quadrupolar splittings, from MD trajectories and compared them to experimental measurements. The calculated NMR parameters show good agreement with experiment, supporting the accuracy of the structural ensemble used for subsequent analyses. Having established agreement with experiment, we examined the peptide dimer architecture and its stabilizing interactions, addressing earlier speculations about supramolecular organization. We find that aromatic π–π

stacking between tyrosine residues (Y7) in antiparallel helices provides persistent stabilization of the dimer interface. Phenylalanine residues (F14) at the boundaries between neighboring dimer blocks also form π–π contacts, albeit with lower persistence than the Y7 interactions. Specific peptide–lipid contacts further stabilize the belt: polar residues such as lysine (K9) and glutamic acid (E12) frequently interact electrostatically with DMPC headgroups, while aromatic residues—particularly tyrosine (Y2) and phenylalanine (F6) anchor the peptide to the hydrophobic acyl chains of lipids and cover them from direct exposure to the aqueous environment. Comparison of lipid properties in 14A/DMPC nanodiscs to a reference DMPC bilayer slab reveals pronounced rim-to-core heterogeneity. Lipids proximal to the peptide belt exhibit reduced acyl-chain order and a thinner local bilayer than those at the nanodisc center. Increasing temperature accentuates thinning and disorder across the disc, with more pronounced effects at the rim, and these trends are consistent across the nanodisc sizes we examined.

Collectively, our MD simulations support a dimeric, antiparallel, belt-like arrangement of 14A peptides around a discoidal DMPC bilayer, stabilized by a synergy of aromatic π–π stacking and complementary electrostatic and hydrophobic peptide–lipid interactions. These atomistic insights provide direct evidence for previously hypothesized interaction motifs and clarify how amphipathic helices organize to define the rim architecture of peptide-based nanodiscs, setting the stage for 4F and 4F-P-4F based nanodisc systems.

Guided by our detailed analysis of 14A-based nanodiscs and prior NMR data on 14A, 18A and 4F ([6–8]), we constructed structural models for 4F and 4F–P–4F nanodiscs featuring antiparallel peptide arrangement around the discoidal lipid bilayer. Because solid-state NMR measurements reporting the local orientation of these peptides (e.g., helix tilt and azimuth relative to the bilayer normal) were not available at the time of this work, we evaluated the MD models at a global morphological level. Specifically, we computed ensemble-averaged SAXS profiles from explicit-solvent, MD ensembles and compared them with experimental SAXS datasets from our collaborators to assess size, shape, and overall structural organization.

Comparing I(q) profiles from simulations of 14A, 4F, and 4F–P–4F nanodiscs showed that the positions of the first principal minimum and subsequent maximum were nearly identical across all three systems. These features are predominantly governed by the disc diameter and bilayer thickness, indicating that SAXS is more sensitive to the global form factor than to peptide-sequence details. Consequently, SAXS alone has limited power to distinguish nanodiscs formed by different peptides if their overall sizes are similar. Experimental SAXS from our collaborators for 4F/DMPC and 4F–P–4F/DMPC showed a low-q upturn and non-linear Guinier regions, indicating polydispersity and interparticle interactions. Indirect Fourier transforms yielded broad $P(r)$ with $D_{\max} \approx 27\,\text{nm}$ (4F) and $\approx 33\,\text{nm}$ (4F–P–4F), consistent with a wide size distribution and some aggregates. This heterogeneity complicates one-to-one comparisons between the experimental data and MD ensembles of single-size nanodiscs.

To isolate size effects in the SAXS profiles, we varied nanodisc diameter by adjusting the peptide: lipid ratio. Larger discs yielded a shallower first minimum that shifted to lower q, mirroring experiment–simulation differences. Constraining models with experimental R_g and $D_{\max}$ identified MD simulated sizes that best reproduced the experimental features (minima/maxima positions). Further, we attempted model polydispersity by Gaussian-weighting monodisperse 4F/DMPC nanodiscs spanning 9–32 nm (B1–B15). Scanning mean and width showed that larger discs (B11–B15) best reproduce the characteristic minima, maxima, and overall shape of the experimental SAXS profiles, with the best agreement near B12 (25.4 nm) and $\sigma = 3$ ($\chi^2 \approx 1.2$). Broadening beyond $\sigma = 3$ did not improve fits, and the χ^2 values are below 6 across all cases, indicating that the apparent fit quality is likely overestimated due to large uncertainties in the experimental SAXS curves. A systematic misfit persists at low q ($q \lesssim 0.2$ nm^{-1}), consistent with aggregation and/or interparticle interactions not captured by the models. Overall, the analysis narrows the plausible size range but does not yield a unique distribution, and supports a polydisperse sample biased toward larger nanodiscs (B11–B15). Finally, we performed a cross-system validation using previously reported SAXS data for 18A/DMPC nanodiscs [9]. Theoretical curves from the 4F/DMPC simulations of system B1 with smaller diameter of 10 nm reproduced the global features of the 18A/DMPC dataset and yielded quantitative parameters—peptide/lipid stoichiometry and bilayer thickness—within reported ranges. Thus, MD-generated structures recapitulate the overall size and shape observed experimentally, supporting the robustness of our modeling at the global level. While preliminary, this validation increases confidence in the modeling and analysis workflow used to characterize the nanodisc systems. Integrating SAXS with MD provides a powerful framework for constraining nanodisc size, shape, and overall morphology. Given limitations of the present experimental data (polydispersity and interparticle effects), exact reproduction of the SAXS curves was not achievable. Nevertheless, the joint SAXS–MD approach enables direct model–experiment comparisons, informs nanodisc dimension estimates, and pinpoints likely sources of disagreement.

In the final part of the Results, we report work performed with biophysical experimentalists and biomedical collaborators to link nanodisc structure to function. In parallel with our simulations, collaborators characterized 4F-P-4F/DMPC nanodiscs and conducted in vitro assays and in vivo mouse studies relevant to inflammatory lung disease. We modeled 4F-P-4F/DMPC discs with average diameters matched to TEM/DLS, and computed CD spectra from MD ensembles that agreed with measurements for both peptide-in-solution and lipidated states, indicating comparable helicity across conditions. MD resolved molecular features difficult to access experimentally, revealing stabilizing peptide–lipid contacts with Lys–phosphate interactions more frequent than Glu–choline contacts.

Prior work indicates that stable [10, 11], discoidal nHDL–like particles are required for sHDL activity, and our results concur: amphipathic helices must be lipidated and arranged in a discoidal geometry to support efficient cholesterol efflux. Lipid-free peptide showed no measurable efflux from human eosinophils and, consistent with previous studies, free amphipathic peptides tend to aggregate and behave un-

predictably in biological media [11, 12]. Biological assays further link structure to function: 4F-P-4F sHDL inhibits eotaxin-driven eosinophil chemotaxis in vitro, while blockade of ABCA1 and SR-BI abolishes this effect, implicating HDL receptor pathways. A plausible mechanism is sHDL-mediated modulation of membrane cholesterol via ABCA1/SR-BI, altering downstream signaling required for chemotaxis. These findings motivate continued evaluation of sHDL formulations as candidates for treating pulmonary inflammatory disease. This structure–function linkage supports and extends the prevailing hypothesis that nHDL–like discoidal geometry is a prerequisite for sHDL activity and function.

We note several methodological constraints that frame this work. For the 4F and 4F-P-4F nanodiscs, we adopted an antiparallel peptide architecture based on prior reports of 18A, 14A, and 4F ([6–8]) because contemporaneous ssNMR measurements of local peptide orientation were not available. In the SAXS analysis, sample polydispersity and minor aggregation impeded the exact reproduction of experimental curves.

Nevertheless, our results support a dimeric, belt-like assembly of 14A peptides around a discoidal lipid bilayer, and we characterized the key peptide–peptide and peptide–lipid interactions that stabilize the rim. We then extended the study to 4F and 4F-P-4F nanodiscs, providing a quantitative global description of disc size and shape; however, molecular-level features, such as peptide orientation, remain to be validated against experimental measurements. To our knowledge, this work provides a controllable molecular modeling framework for peptide-based nanodiscs, with size and composition explicitly defined, along with reproducible procedures for model construction and validation. Further collaboration between experiment and simulation should yield models that more closely match experimental measurements and support ongoing refinement, enabling a detailed study of their biological relevance. Despite these constraints, this thesis establishes a robust foundation and reproducible workflow for future studies of apoA-I mimetic peptide-lipid nanodiscs (including 18A and related sequences), enabling the rational design of improved scaffolds for biomedical applications and cardiovascular therapeutics and providing an optimized platform for membrane-protein characterization.

4.2 Perspectives

While apoA-I mimetic peptide-lipid assemblies constitute a broad research area, in this thesis, we focus on three clinically relevant sequences: 14A, 4F, and 4F-P-4F. Simulation studies of peptide-based nanodiscs are still relatively scarce despite their wide applicability. In collaboration with experimentalists, we developed and validated a reproducible protocol spanning nanodisc construction, MD simulation, and analysis, and we established a physicochemical framework for interpreting 14A, 4F, and 4F-P-4F peptide-lipid assemblies. Building on these results, we outline concrete directions for future work:

- **NMR-guided peptide orientation for 4F and 4F-P-4F.** Recent ssNMR data from our collaborators suggest an antiparallel arrangement of 4F and 4F-P-4F around DMPC, further supporting our hypothesis. To resolve local orientations of the peptides, we could compute ^{15}N chemical shifts and ^{2}H quadrupolar splittings from MD simulations and compare them directly with ssNMR measurements to obtain an atomistic picture of peptide orientation around the discoidal lipid bilayer. (These experimental data are not reported in this thesis.)

- **Cross-system comparison and design implications.** Once the 4F and 4F–P–4F nanodisc models are validated and refined, we will compare the 14A, 4F, and 4F–P–4F peptide–lipid nanodiscs to rationalize their behaviors and to inform the future design of bio-active apoA-I–mimetic peptides.

- **Link to cholesterol efflux via ABCA1.** To clarify how sHDL particles mediate efficient cholesterol efflux, we can investigate their interactions with ABCA1, the initial step in reverse cholesterol transport. To our knowledge, simulations of peptide-based nanodiscs engaging ABCA1 have not yet been reported.

- **ApoA-I mimetic peptides based nanodiscs interactions with oxidized Lipids.** Peptide mimetics bind oxidized phospholipids (oxPLs) and oxidized fatty acids (oxFAs) with affinities *orders of magnitude* higher than the parent apolipoprotein A–I [13, 14]. Owing to their anti-inflammatory and antioxidant activities, they are being explored as therapeutics for multiple diseases [15]. Our results indicate that current computational resources are sufficient to address the central questions of this project, but several methodological gaps remain. While atomistic force fields (e.g., CHARMM) adequately describe amphipathic α-helical mimetics and standard lipids, **compatible parameters for oxidized lipids (oxPLs)** are lacking. Following **protocols established by our group** in prior work [16], we will perform high-level quantum-chemical calculations to derive atomic partial charges and bonded terms (including key torsions) for the peroxidized/oxidized moieties, thereby generating a consistent oxPL force field. We will then construct peptide-based nanodiscs containing DMPC and selected oxPLs to investigate: (i) how oxidized lipids diffuse within nanodiscs, (ii) how they interact with apoA–I–derived peptides, and (iii) how they modulate the nanodisc lipid properties.

- **Extend peptide-based nanodisc all-atom model to coarse-grained (CG) model.** Processes on microsecond timescales and in very large systems remain beyond the reach of routine atomistic simulations. To overcome these limitations, we can extend our all-atom model of peptide-based nanodiscs to a coarse-grained representation. This enables us to address open questions such as whether lipid exchange between apoA-I–mimetic peptide nanodiscs is mediated by diffusion of lipids through the aqueous phase or by collision-mediated [17, 18].

References

[1] Karin Kornmueller, Ivan Vidakovic, and Ruth Prassl. Artificial high density lipoprotein nanoparticles in cardiovascular research. *Molecules*, 24(15):2829, 2019.

[2] Xianglan Yao, Michael P Vitek, Alan T Remaley, and Stewart J Levine. Apolipoprotein mimetic peptides: a new approach for the treatment of asthma. *Frontiers in pharmacology*, 3:37, 2012.

[3] Oleg F Sharifov, Xin Xu, Amit Gaggar, William E Grizzle, Vinod K Mishra, Jaideep Honavar, Silvio H Litovsky, Mayakonda N Palgunachari, C Roger White, GM Anantharamaiah, et al. Anti-inflammatory mechanisms of apolipoprotein ai mimetic peptide in acute respiratory distress syndrome secondary to sepsis. *PLoS One*, 8(5):e64486, 2013.

[4] TK Ritchie, YV Grinkova, TH Bayburt, IG Denisov, JK Zolnerciks, WM Atkins, and SG Sligar. Reconstitution of membrane proteins in phospholipid bilayer nanodiscs. *Methods in enzymology*, 464:211–231, 2009.

[5] Yifei Qi, Jumin Lee, Jeffery B Klauda, and Wonpil Im. Charmm-gui nanodisc builder for modeling and simulation of various nanodisc systems. *Journal of computational chemistry*, 40(7):893–899, 2019.

[6] Evgeniy S Salnikov, GM Anantharamaiah, and Burkhard Bechinger. Supramolecular organization of apolipoprotein-ai-derived peptides within disc-like arrangements. *Biophysical journal*, 115(3):467–477, 2018.

[7] Vinod K Mishra, GM Anantharamaiah, Jere P Segrest, Mayakonda N Palgunachari, Manjula Chaddha, SW Simon Sham, and N Rama Krishna. Association of a model class a (apolipoprotein) amphipathic α helical peptide with lipid: High resolution nmr studies of peptide· lipid discoidal complexes. *Journal of Biological Chemistry*, 281(10):6511–6519, 2006.

[8] Vinod K Mishra, Mayakonda N Palgunachari, N Rama Krishna, John Glushka, Jere P Segrest, and GM Anantharamaiah. Effect of leucine to phenylalanine substitution on the nonpolar face of a class a amphipathic helical peptide on its interaction with lipid: high resolution solution nmr studies of 4f-dimyristoylphosphatidylcholine discoidal complex. *Journal of Biological Chemistry*, 283(49):34393–34402, 2008.

[9] Søren Roi Midtgaard, Martin Cramer Pedersen, Jacob Judas Kain Kirkensgaard, Kasper Kildegaard Sørensen, Kell Mortensen, Knud J Jensen, and Lise Arleth. Self-assembling peptides form nanodiscs that stabilize membrane proteins. *Soft matter*, 10(5):738–752, 2014.

[10] Rafique M Islam, Mohsen Pourmousa, Denis Sviridov, Scott M Gordon, Edward B Neufeld, Lita A Freeman, B Scott Perrin Jr, Richard W Pastor, and Alan T Remaley. Structural properties of apolipoprotein ai mimetic peptides that promote abca1-dependent cholesterol efflux. *Scientific Reports*, 8(1):2956, 2018.

[11] Jie Tang, Dan Li, Lindsey Drake, Wenmin Yuan, Sara Deschaine, Emily E Morin, Rose Ackermann, Karl Olsen, David E Smith, and Anna Schwendeman. Influence of route of administration and lipidation of apolipoprotein ai peptide on pharmacokinetics and cholesterol mobilization. *Journal of lipid research*, 58 (1):124–136, 2017.

[12] Wilissa D'Souza, John A Stonik, Andrew Murphy, Steven J Demosky, Amar A Sethi, Xiao L Moore, Jaye Chin-Dusting, Alan T Remaley, and Dmitri Sviridov. Structure/function relationships of apolipoprotein ai mimetic peptides: implications for antiatherogenic activities of high-density lipoprotein. *Circulation research*, 107(2):217–227, 2010.

[13] Raquel F Epand, Vinod K Mishra, Mayakonda N Palgunachari, GM Anantharamaiah, and Richard M Epand. Anti-inflammatory peptides grab on to the whiskers of atherogenic oxidized lipids. *Biochimica et Biophysica Acta (BBA)-Biomembranes*, 1788(9):1967–1975, 2009.

[14] G Kees Hovingh, Andrea E Bochem, and John JP Kastelein. Apolipoprotein ai mimetic peptides. *Current opinion in lipidology*, 21(6):481–486, 2010.

[15] Srinivasa T Reddy, Mohamad Navab, Gattadahalli M Anantharamaiah, and Alan M Fogelman. Apolipoprotein ai mimetics. *Current opinion in lipidology*, 25(4):304–308, 2014.

[16] Julian Garrec, Antonio Monari, Xavier Assfeld, Lluis M Mir, and Mounir Tarek. Lipid peroxidation in membranes: the peroxyl radical does not "float". *The Journal of Physical Chemistry Letters*, 5(10):1653–1658, 2014.

[17] Masakazu Miyazaki, Yoko Tajima, Tetsurou Handa, and Minoru Nakano. Static and dynamic characterization of nanodiscs with apolipoprotein ai and its model peptide. *The Journal of Physical Chemistry B*, 114(38):12376–12382, 2010.

[18] Chiharu Anada, Keisuke Ikeda, Ayako Egawa, Toshimichi Fujiwara, Hiroyuki Nakao, and Minoru Nakano. Temperature-and composition-dependent conformational transitions of amphipathic peptide–phospholipid nanodiscs. *Journal of Colloid and Interface Science*, 588:522–530, 2021.

5 Appendix

5.1 Optimization of 14A Dimeric Antiparallel Arrangement

We began from the dimer configuration of the 14A peptide suggested by our collaborators (Fig. 4 in [1] and Fig. 5.1A). Nanodiscs were assembled with the same composition as System A (24 peptides and 186 DMPC lipids in Table:3.1) and subjected to MD simulations. After equilibration, positional restraints were released sequentially. Upon release, steric clashes between aromatic side chains caused the 14A dimer to collapse; repeated short 100 ns replicas did not yield a stable dimer in this configuration (Fig. 5.1B).

ssNMR measurements indicate that the peptides adopt an antiparallel, head-to-tail arrangement oriented approximately perpendicular to the bilayer normal [1]. Guided by this, we generated initial docked dimeric poses using ClusPro [2] and performed explicit-solvent MD simulation on the dimers in water for 200ns (Fig. 5.1C(i)) to relax the structure. In the simulation, a Tyr–Tyr contact between Y7 residues formed and stabilized the dimer in water for ∼200 ns (Fig. 5.1C(ii)).

We selected this antiparallel dimeric configuration that satisfied our structural criteria as the building block for revised nanodiscs (Fig. 5.1D) and constructed the systems according to our protocol (Section 2.2). We ran five short replicas (100 ns each) at 30 °C to assess stability of the dimer within nanodiscs, followed by three independent 1 μs replicas at 30 °C and three independent 1 μs replicas at 37 °C (Fig. 5.1E) to enable comparison of simulation-derived NMR observables with the experimental measurements.

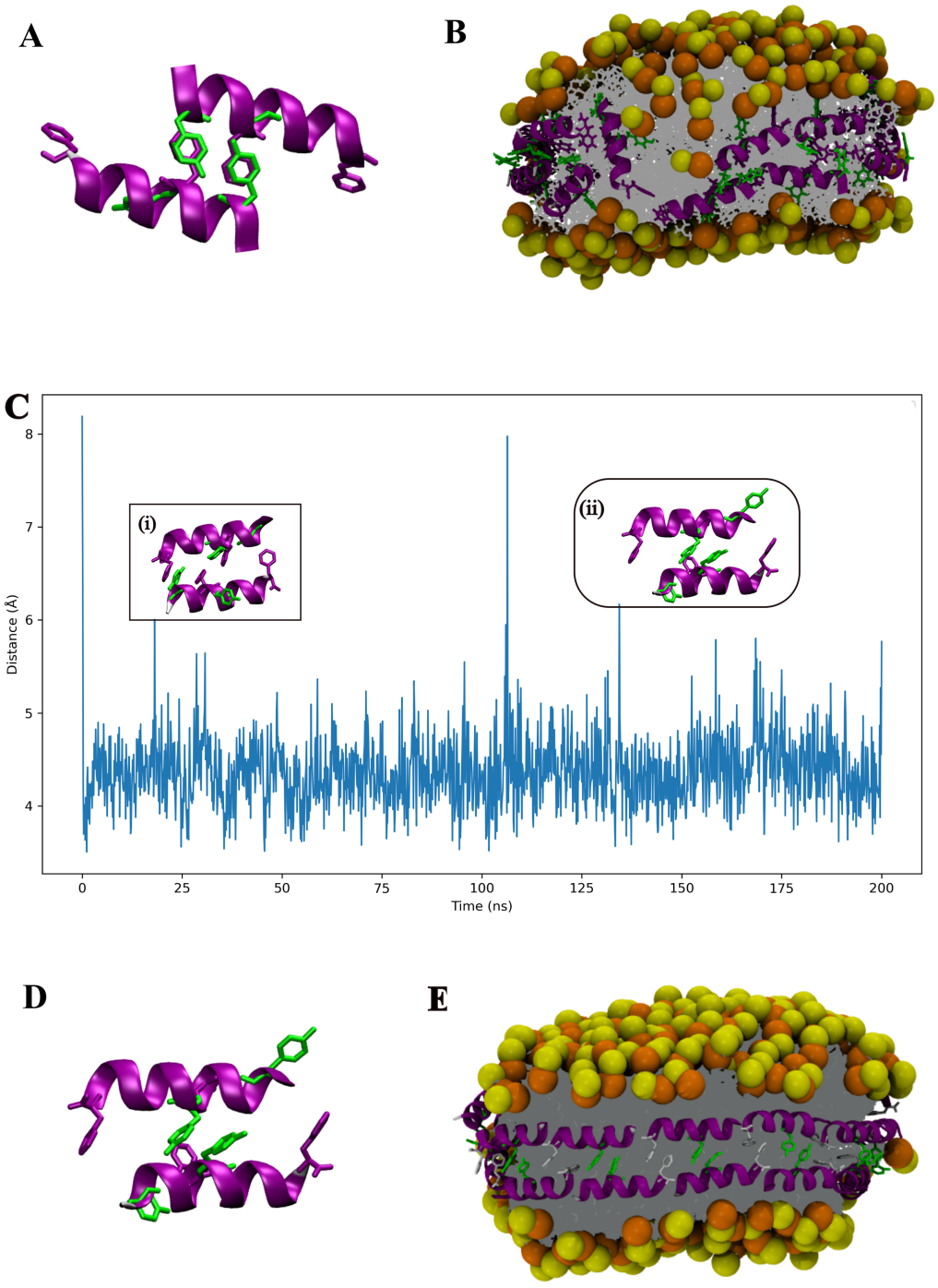

Figure 5.1: **(A)** Schematic of the collaborator-proposed 14A dimer configuration. **(B)** Representative snapshot showing collapse of the dimer at the nanodisc rim after restraint release. **(C)** Time series of the distance between the centers of mass of the Tyr7 aromatic rings over 500 ns. **(D)** Antiparallel, head-to-tail dimer configuration that satisfies our structural criteria. **(E)** Pictorial representation of a stable 14A-peptide nanodisc after a 1 μs simulation at 37 °C.

5.2 Orientation of the Side Chain

For each aromatic residue, the plane of the aromatic ring is defined using the positions of three atoms: $\vec{r}_{\mathrm{CG}}$, $\vec{r}_{\mathrm{CD1}}$, and $\vec{r}_{\mathrm{CE2}}$. Two vectors lying in the plane of the ring are defined as

$$\vec{v}_1 = \vec{r}_{\mathrm{CD1}} - \vec{r}_{\mathrm{CG}}, \quad \vec{v}_2 = \vec{r}_{\mathrm{CE2}} - \vec{r}_{\mathrm{CG}}.$$

The normal vector $\vec{n}$ to the ring plane is computed by taking the cross product of these vectors:

$$\vec{n} = \vec{v}_1 \times \vec{v}_2.$$

This normal vector is then normalized to obtain the unit normal vector:

$$\hat{n} = \frac{\vec{n}}{\|\vec{n}\|}.$$

Assuming the membrane normal is aligned with the z-axis (represented by the unit vector $\vec{k} = (0, 0, 1)$), the angle θ between the aromatic ring normal and the membrane normal is calculated using the dot product:

$$\cos\theta = \hat{n} \cdot \vec{k} \quad \Longrightarrow \quad \theta = \arccos\left(\hat{n} \cdot \vec{k}\right).$$

This angle θ quantifies the tilt of the aromatic ring relative to the membrane normal.

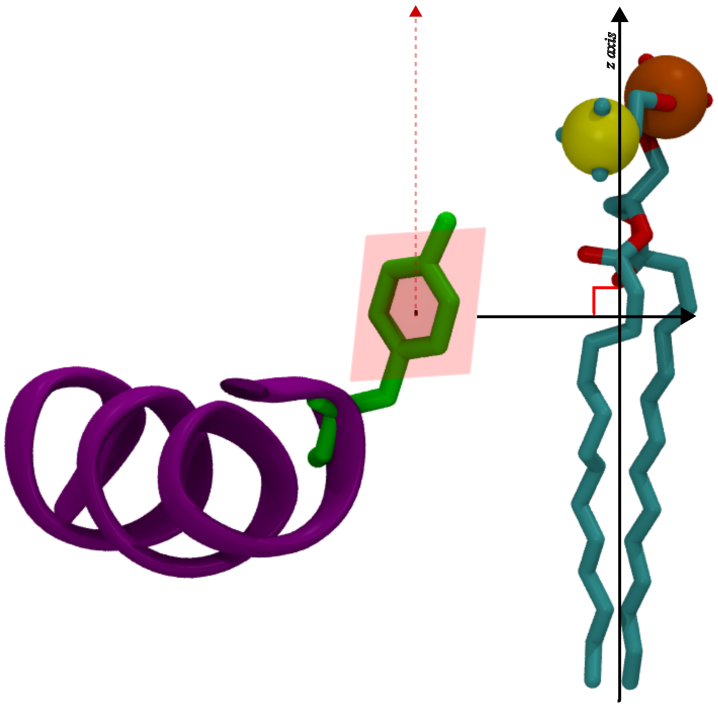

Figure 5.2: Pictorial representation of the method used to calculate the orientation of 14A peptide sidechain aromatic rings relative to the membrane axes. The aromatic ring plane is aligned parallel to the z-axis, with its normal oriented perpendicular to the membrane plane. The calculation was performed by measuring the angle between the aromatic ring normal and the membrane normal.

5.3 Gaussian Distribution of Sizes of Nanodiscs to Introduce the Polydispersity

To account for polydispersity in the experimental SAXS data, we assume that particle sizes follow a Gaussian (normal) distribution. For each mean μ (size) and standard deviation σ, we compute normalized Gaussian weights for each size contribution from the distribution and multiply these weights with the respective SAXS curves and sum them to obtain a single polydisperse theoretical profile. Comparing these profiles with the experiment identifies the (μ, σ) pair, and thus the size distribution from the simulated models, that best matches the data.

Polydispersity model and fit to experiment

We model size polydispersity with a Gaussian (normal) distribution of mean μ and standard deviation σ:

$$P(s \mid \mu, \sigma) \;=\; \mathcal{N}\big(s \mid \mu, \sigma^2\big) \;=\; \frac{1}{\sqrt{2\pi}\,\sigma}\,\exp\!\left[-\frac{(s-\mu)^2}{2\sigma^2}\right]. \tag{5.1}$$

Simulations are available at a discrete set of sizes $\{s_i\}$ (e.g., $s_i \in (B1, B2, B3, .., B15)$ for each MD model Table: 3.9). We therefore discretize (5.1) into normalized weights

$$w_i(\mu,\sigma) \;=\; \frac{\mathcal{N}(s_i \mid \mu, \sigma^2)}{\sum_k \mathcal{N}(s_k \mid \mu, \sigma^2)} \;=\; \frac{\exp\big[-(s_i-\mu)^2/(2\sigma^2)\big]}{\sum_k \exp\big[-(s_k-\mu)^2/(2\sigma^2)\big]}, \qquad \sum_i w_i = 1,\;\; w_i > 0 \tag{5.2}$$

Each polydisperse theoretical SAXS profile is the Gaussian-weighted average $I(q; s_i)$:

$$I_{\text{theor}}(q;\mu,\sigma) \;=\; \sum_i w_i(\mu,\sigma)\, I(q; s_i). \tag{5.3}$$

To fit I_{theor} to the experimental curve $I_{\text{exp}}(q)$ using a *single* global scale factor c,

where c is obtained by weighted least squares:

$$c \;=\; \frac{\displaystyle\sum_j \frac{I_{\text{exp}}(q_j)\, I_{\text{theor}}(q_j)}{\sigma(q_j)^2}}{\displaystyle\sum_j \frac{I_{\text{theor}}(q_j)^2}{\sigma(q_j)^2}}. \tag{5.4}$$

The goodness of fit for a given (μ, σ) is quantified by the chi-squared

$$\chi^2 \;=\; \frac{1}{N-1}\sum_{j=1}^{N}\left[\frac{I_{\text{exp}}(q_j) - c\, I_{\text{theor}}(q_j)}{\sigma(q_j)}\right]^2, \tag{5.5}$$

with N the number of data points and $\sigma(q_j)$ is uncerinities from the experimental data set.

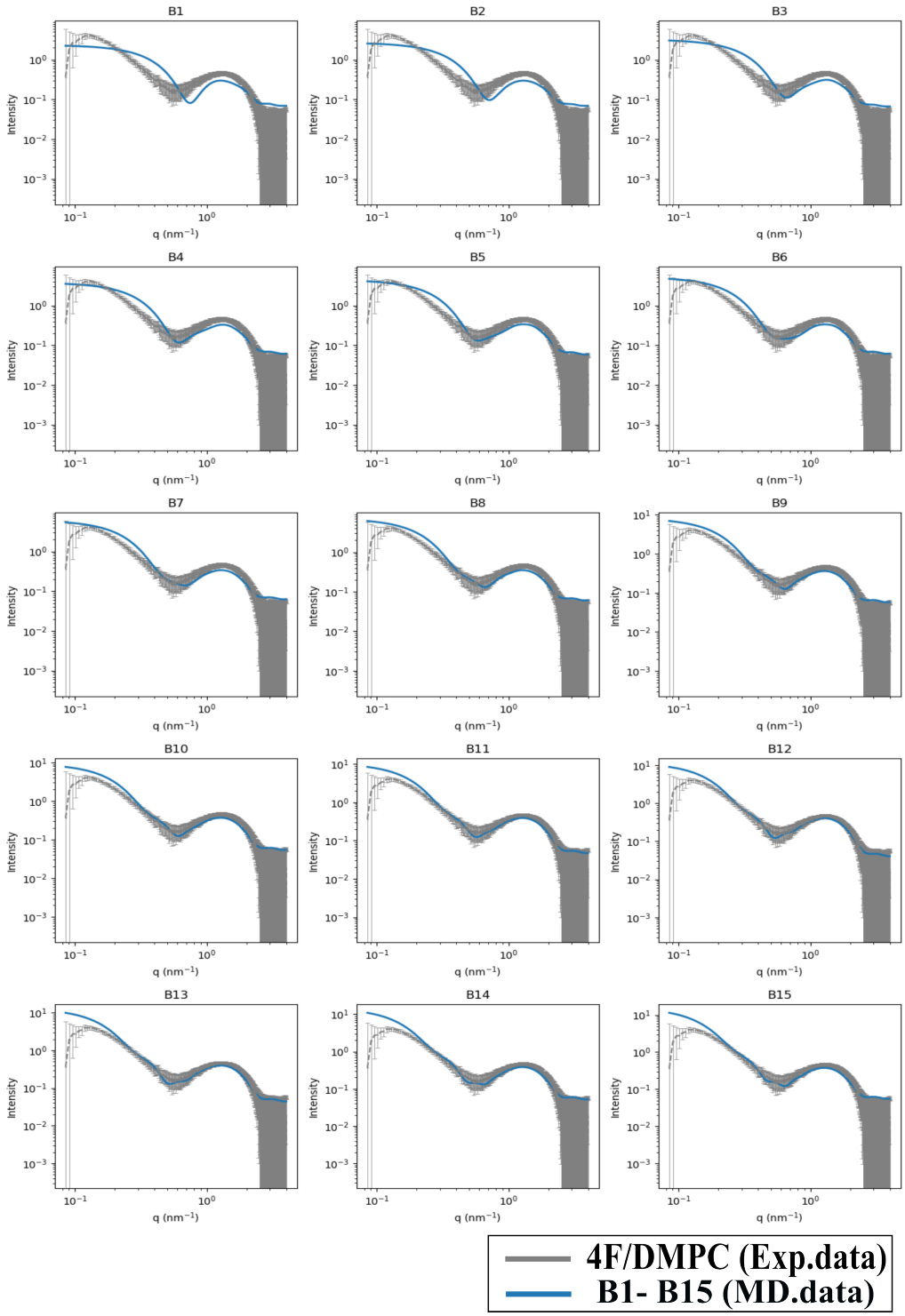

Figure 5.3: **Polydisperse theoretical SAXS profiles for 4F/DPMC.** Each panel (B1–B15) corresponds to a Gaussian size distribution with the mean centered on the indicated system and standard deviation $\sigma = 3$. The resulting polydisperse profiles are fit to the experimental data using a single global scale factor C and plotted on a log–log scale as $\log I(q)$ versus $\log q$, with q in nm^{-1}.

Gaussian mean	χ^2 **value**
B1	5.6
B2	5.1
B3	4.4
B4	3.6
B5	3.2
B6	3.1
B7	3.0
B8	2.6
B9	2.3
B10	2.0
B11	1.5
B12	1.2
B13	1.4
B14	1.9
B15	2.1

Table 5.1: The χ^2 values for Gaussian-mean centered B1–B15 with standard deviation of $\sigma = 3$.

References

[1] Evgeniy S Salnikov, GM Anantharamaiah, and Burkhard Bechinger. Supramolecular organization of apolipoprotein-ai-derived peptides within disc-like arrangements. *Biophysical journal*, 115(3):467–477, 2018.

[2] Dima Kozakov, David R Hall, Bing Xia, Kathryn A Porter, Dzmitry Padhorny, Christine Yueh, Dmitri Beglov, and Sandor Vajda. The cluspro web server for protein–protein docking. *Nature protocols*, 12(2):255–278, 2017.